Lateral-Mode Vibration of Microcantilever-Based Sensors in Viscous Fluids Using Timoshenko Beam Theory

Joshua Schultz
Marquette University

LATERAL-MODE VIBRATION OF MICROCANTILEVER-BASED SENSORS IN VISCOUS FLUIDS USING TIMOSHENKO BEAM THEORY

by

Joshua A. Schultz, B.S.A.E., M.S.S.E.

A Dissertation submitted to the Faculty of the Graduate School,
Marquette University,
in Partial Fulfillment of the Requirements for
the Degree of Doctor of Philosophy in Civil Engineering.

Milwaukee, Wisconsin

December 2012

ABSTRACT

LATERAL-MODE VIBRATION OF MICROCANTILEVER-BASED SENSORS IN VISCOUS FLUIDS USING TIMOSHENKO BEAM THEORY

Joshua A. Schultz, B.S.A.E., M.S.S.E.

Marquette University, 2012

Dynamic-mode microcantilever-based devices are well suited to biological and chemical sensing applications. However, these applications often necessitate liquid-phase sensing, introducing significant fluid-induced dissipative forces and reducing device quality factors (Q). Recent experimental and analytical research has shown that higher in-fluid Q is achieved by exciting microcantilevers in the lateral flexural mode. However, the experimental results show that, for microcantilevers having larger width-to-length (b/L) ratios, the behaviors predicted by current analytical models differ from measurements.

To more accurately model microcantilever resonant behavior in viscous fluids and to improve understanding of lateral-mode sensor performance, a new analytical model is developed, incorporating both viscous fluid effects and "Timoshenko beam" effects (shear deformation and rotatory inertia). Analytical solutions for the frequency response are obtained and verified by reduction to known special cases. Beam response is examined for two harmonic load types that simulate current actuation methods: tip force and support rotation. Results are expressed in terms of total beam displacement and beam displacement due solely to bending deformation, which correspond to current detection methods commonly used with these devices (laser and piezoresistive detection, respectively). Resonant frequencies (f_{res}) and Q are determined from the theoretical beam response. The influences of the shear, rotatory inertia, and fluid parameters, as well as the load/detection scheme, on the resonant characteristics are investigated in detail. Results show that the new model reproduces the experimental trends in f_{res} and Q for lateral-mode microcantilevers at higher b/L ratios (i.e., for the high-Q devices for which Euler-Bernoulli models prove inadequate). Over the practical ranges of system parameters considered, the results indicate that Timoshenko beam effects can account for a reduction in f_{res} and Q of up to 23%, but are negligible (no more than 2% reduction) for length-to-width ratios of 7 and higher. Also derived is a simple analytical expression relating Q to system parameters while incorporating Timoshenko and fluid effects. Finally, to evaluate the influence of lateral-mode chemical sensor design parameters on performance, the results for f_{res} and Q are related to the mass/chemical sensitivities and to the limit of detection (LOD), and illustrative calculations of sensitivity and LOD are presented.

ACKNOWLEDGMENTS

Joshua A. Schultz B.S.A.E., M.S.S.E.

Completion of this dissertation is a result of the time, effort and energy of many generous individuals who have taught, mentored and supported me. Consequently, I'd like to specifically thank a handful of people who were instrumental in this dissertation.

I would like to extend my thanks to my advisor, Dr. Stephen Heinrich, for his instruction and guidance. He has maintained an excellent balance between direction and freedom which has encouraged me to grow and improve both as an engineer as well as a researcher. Exposure to his rigorous attention to detail and relentless pursuit of excellence has left an indelible mark on my intellectual posture and habits.

I would like to thank my dissertation committee, consisting of: Dr. Christopher Foley, Dr. Isabelle Dufour, Dr. Fabien Josse and Dr. Nicholas Nigro. It has been a privilege to work with and learn from this excellent group of researchers and teachers. Exposure to their insight and ideas over the course of my graduate studies has greatly impacted the quality of my engineering expertise and development of my research style. I would also like to thank my friend and mentor Dr. Chris Stutzki, for the countless coffee talks during which he offered sagacious perspective on my academic and professional development. I am indebted to him for measuring out (via countless coffee spoons) his encouragement of my progress and high expectations of my success.

I would like to thank my parents, Todd and Julie Schultz, for their sacrifice, love and support. I am blessed to have them as parents.

I must thank my loving wife, Katelyn, for *everything* that she is and does. I relied on her for patient support and encouragement every day of this academic journey—she truly is my "fixed foot." Her enthusiasm and energy for every new day has often served to buoy my spirits during this shared graduate school experience.

Chesterton once said "gratitude is happiness doubled by wonder," and it is in humble agreement that I conclude these acknowledgements with: *ad majorem Dei gloriam*.

TABLE OF CONTENTS

LIST OF FIGURES

LIST OF TABLES

NOMENCLATURE

Symbols

A = cross-sectional area of cantilever beam;

b = width of rectangular beam (dimension along y-axis);

C_i, C_i' = coefficients on the $\overline{V}(\xi)$ and $\Phi(\xi)$ equations, respectively;

$C_i^*, C_i^{*\prime}$ = scaled coefficients on $\overline{V}(\xi)$ and $\Phi(\xi)$ equations, respectively = $\frac{C_i}{\overline{F}_0}, \frac{C_i'}{\overline{F}_0}$;

$C()$ = cosh();

$C1 \equiv \sqrt{\frac{E}{12\rho}}$ = best-fit parameter, related to the initial slope of in-air frequency vs. b/L^2 data;

$C2 \equiv \sqrt{\frac{E}{kG}}$ = best-fit parameter, related to nonlinearity of in-air frequency vs. b/L^2 data at high b/L^2 values;

$c()$ = cos();

$\overline{c}_f$ = effective fluid damping coefficient per unit length;

$\overline{\overline{c}}_f$ = distributed effective fluid damping coefficient per unit area;

D_B = Normalized amplitude of bending displacement at cantilever tip;

D_{B-D} = Normalized amplitude of bending-deformation displacement at cantilever tip;

D_S = Normalized amplitude of shear displacement at cantilever tip;

D_T = Normalized amplitude of total displacement at cantilever tip;

E = Young's modulus of beam material (along longitudinal direction x of beam);

EB = notation for Euler-Bernoulli beam theory;

$F(t) = F_0 e^{i\omega t}$ = applied harmonic tip force;

F_0 = amplitude of imposed harmonic tip force;

$\bar{F}_0 \equiv \frac{F_0 L^2}{EI}$ = non-dimensional applied tip force amplitude;

f_I = beam inertial force per unit length;

f_{res} = resonant frequency [Hz];

G = shear modulus of beam material (corresponding to *x*-*y* directions);

g = acceleration due to gravity;

h = thickness of rectangular beam cross section (dimension along *z*-axis);

I = second moment of area of beam cross section ("moment of inertia") with respect to neutral axis;

i = imaginary number, $\sqrt{-1}$;

K = partition coefficient of specific coating/analyte pair in a given surrounding medium = ratio of the steady-state analyte concentration in the sensing layer to the analyte concentration in surroundings;

k = shear correction factor in Timoshenko beam theory;

L = length of beam (dimension along *x*-axis);

LOD = limit of detection;

M = bending moment;

$\bar{m}_b \equiv \rho_b A$ = mass per unit length of beam;

$\bar{m}_f$ = effective fluid mass per unit length;

$\bar{\bar{m}}_f$ = distributed effective fluid mass coefficient per unit area;

$n_i(\lambda)$ = frequency-dependent roots of characteristic equation for assumed solution of a Timoshenko Beam, i=1, 2, 3, 4;

$q(x,t) \equiv Q(x)e^{i\omega t}$ = applied harmonic distributed load;

$\bar{q}(\xi,\tau) \equiv \bar{Q}(\xi)e^{i\tau}$ = non-dimensional applied harmonic distributed load;

$Q(x)$ = magnitude of distributed force loading in dimensional form

$\bar{Q}(\xi) \equiv \frac{Q(x)L^3}{EI}$ = magnitude of distributed force loading in non-dimensional form

Q = quality factor of beam at resonance (associated with viscous losses in surrounding fluid);

$r^2 \equiv \frac{I}{AL^2}$ = rotational inertia parameter $= \frac{1}{12}\left(\frac{b}{L}\right)^2$ for rectangular cross section;

$S()$ = sinh();

S_c = chemical sensitivity;

S_m = mass sensitivity;

$s()$ = sin();

$s^2 \equiv \frac{EI}{kAGL^2}$ = shear deformation parameter, $= \frac{1}{12}\left(\frac{b}{L}\right)^2\left(\frac{E}{kG}\right)$ for rectangular cross section;

TB = notation for Timoshenko beam theory;

t = time coordinate;

$v(x,t)$ = total deflection of beam at position x at time t;

$\bar{v}(\xi,\tau)$ = dimensionless total beam deflection at position ξ at time τ;

$v_B(x,t)$ = deflection of beam due to bending (including any rigid displacement) at position x at time t;

$\bar{v}_B(\xi,\tau)$ = dimensionless beam deflection due to bending (including any rigid displacement) at position ξ at time τ;

$v_{B-D}(x,t)$ = deflection of beam due to bending deformation *only* (not including rigid displacement) at position x at time t;

$\overline{v}_{B-D}(\xi,\tau)$ = dimensionless beam deflection due to bending deformation *only* (not including rigid displacement) at position ξ at time τ;

$v_S(x,t)$ = deflection of beam due to shear at position *x* at time *t*;

$\overline{v}_S(\xi,\tau)$ = dimensionless beam deflection due to shear at position ξ and at time τ;

$v_R(x,t)$ = deflection of beam due to including rigid displacement at position *x* at time *t*;

$\overline{v}_R(\xi,\tau)$ = dimensionless beam deflection due to rigid displacement at position ξ and at time τ;

$\overline{V}(\xi) \equiv$ = amplitude of $\overline{v}(\xi,\tau)$;

$V_{EB,static}(1)$ = static tip displacement of Euler-Bernoulli cantilever;

$\overline{V}_B(\xi)$ = amplitude of $\overline{v}_B(\xi,\tau)$;

W = transverse shear force in beam;

x = spatial coordinate along the longitudinal direction of the beam;

y = spatial coordinate along the width (*b*) direction of the beam;

z = spatial coordinate along the thickness of the beam (parallel to dimension *h*);

$\overline{\beta}$ = phase angle associated with bending deformation at tip with respect to imposed support rotation;

$\delta \equiv \dfrac{\overline{c}_f}{\sqrt{EI\overline{m}_b / L^4}}$ = (frequency-dependent) relative fluid damping coefficient for the case of general fluid resistance (analogous to a damping ratio);

$\zeta \equiv \dfrac{L}{hb^{1/2}}\left(\dfrac{48{\rho_f}^2\eta^2}{E{\rho_b}^3}\right)^{1/4}$ = fluid-resistance parameter for Stokes's resistance on a rectangular section;

η = dynamic viscosity of fluid;

$\theta(t) = \theta_0 e^{i\omega t}$ = time-dependent, imposed harmonic support rotation;

θ_0 = amplitude of imposed harmonic support rotation;

$\lambda^4 \equiv \dfrac{\omega^2 \bar{m}_b L^4}{EI}$ = dimensionless frequency parameter = $\omega^2 \left(\dfrac{12\rho_b L^4}{Eb^2} \right)$ for a rectangular cross section;

$\dfrac{\lambda_{TB}}{\lambda_{EB}} \equiv$ = ratio of dimensionless natural frequency parameter for a Timoshenko cantilever beam to that of an Euler-Bernoulli cantilever beam in vacuum;

$\mu \equiv \dfrac{\bar{m}_f}{\bar{m}_b}$ = dimensionless (frequency-dependent) effective fluid mass (scaled by beam mass);

υ = Poisson's ratio

$\xi \equiv$ x/L = dimensionless spatial coordinate along the longitudinal direction of beam;

ρ_b = mass density of beam material;

ρ_f = fluid mass density;

σ = normal stress due to bending;

$\tau(t)$ = shear stress exerted by viscous fluid on a plate;

$\tau \equiv \omega t$ = dimensionless time coordinate;

$\Phi(\xi)$ = amplitude of $\varphi(\xi, \tau)$;

$\varphi(x,t)$ = rotation of beam cross section (slope of bending deflection) at position *x* at time *t*;

$\varphi(\xi, \tau)$ = rotation of beam cross section (slope of bending deflection) at position ξ at time τ;

$\psi(x,t)$ = shear strain at position x at time t = derivative of displacement due to shear, $\partial v_S(x,t)/\partial x$;

ω = circular frequency of the load or the natural frequency of the Timoshenko beam in the case of free vibration;

ω_0 = the natural frequency of the Euler-Bernoulli beam in the case of free vibration;

CHAPTER 1: INTRODUCTION

1.1 Background of Microcantilever Sensors

In 1959, Dr. Richard Feynman called on scientists, engineers and physicists to investigate the micro- and nano-scale environment in his watershed lecture, "There's Plenty of Room at the Bottom" [Feynman, 1959]. During the years between 1959 and the early 1990s, there was considerable focus on design and fabrication of small actuators, motors, valves and pumps. Despite all the research, it was not until the advent of microelectronic fabrication technology that the rapid development of atomic force microscopy (AFM) and the field of micro-electro-mechanical systems (MEMS) — including microcantilever-based sensors — was realized [Trimmer, 1997]. AFM maps a surface by using the changes in the frequency as the cantilever interacts with an object. In 1994 the microcantilever tip on the AFM was observed to be sensitive to surrounding effects of humidity, temperature and chemical adsorption [Thundat et al., 1994]. Primarily as an outgrowth of AFM, novel sensing applications have been realized for microcantilever-based sensors, including chemical, physical, biological, biomedical and biochemical sensing arenas [Barnes et al., 1994; Thundat et al., 1994]. Figure 1-1 is an example of a conventional (i.e., transverse-mode) microcantilever-based chemical sensor showing the electrical circuitry on the microcantilever for actuation and detection [Vancura et al., 2008]. Conventional microcantilever-based sensors are operated in the transverse bending mode.

Currently, the field of micro-electro-mechanical systems is a rapidly expanding area of research, especially in chemical and biological sensing arenas. Due to their relatively large surface area-to-volume ratio, microcantilever-based sensors offer several benefits, including the following [Finot et al., 2008]:

- high sensitivity, sensing rates and parallel sensing ability,
- label-free quantification (no control substance required),

- portable and stable sensing platform,
- low production costs associated with simplicity of construction and economies of scale due to batch sizes,
- multiple modes of operation [Boisen et al., 2011].

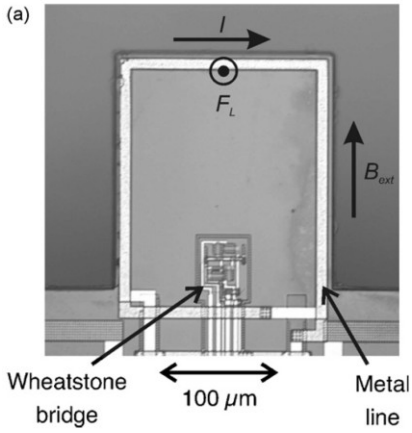

Figure 1-1: Image of Conventional Microcantilever-based Chemical Sensor with Wheatstone Bridge and Metal Loop for Transverse Actuation [Vancura et al., 2008]

These features have elicited interest for a wide variety of practical and commercial uses that include point-of-care medical diagnostics (e.g., blood glucose monitoring), in-situ environmental monitoring of liquids and gases, and detection of hazardous or explosive materials for industrial, military and security needs. Specifically, microcantilever-based sensors have tremendous potential in the areas of bio- and chemical sensing [Li and Lee, 2011]. As a result of their promise in diverse applications, MEMS sensors research in the form of microcantilever-based sensor theory, fabrication and implementation continues to progress for a variety of sensing modes and geometric forms [Zhu, 2011].

In general, a microcantilever-based chemical sensor is a MEMS device that employs changes in either deflection (for static mode of operation) or resonant frequency (for dynamic mode of operation) to assess the presence and/or quantity of a given chemical analyte in the local environment. Mass detection (at ever increasingly low levels) is typically achieved by the use of a

chemically sensitive material (e.g., a deposited coating) that is located on the cantilever sensing platform. The chemically sensitive layer absorbs or adsorbs the chemical analyte, inducing a mechanical or electrical change. In the static mode the sensitive coating on the cantilever sorbs the desired analyte from the surrounding medium. As the target molecules become affixed to the sensor, the microcantilever deflects due to the resulting surface stress and this deflection may be correlated to the concentration of the substance in the surrounding medium. In the dynamic mode, the cantilever is excited at a resonant frequency and undergoes a mass-induced frequency shift as the surrounding analyte is sorbed onto or into the coating.

Microcantilever-based sensors operating in the dynamic mode can be excited in one of several modes as shown schematically in Fig. 1-2:

- Lateral flexural modes (also referred to as “in-plane” flexural modes) are associated with bending about the “strong” (i.e., stiff) axis of the cross section
- Transverse flexural modes (also referred to as “out-of-plane” flexural modes) are associated with bending about the “weak” (i.e., flexible) axis of the cross section
- Torsional (twisting) modes involve the relative rotation of cross sections about the longitudinal axis of the microcantilever
- Axial modes correspond to extension or shortening of the microcantilever, i.e., deformations along the longitudinal axis

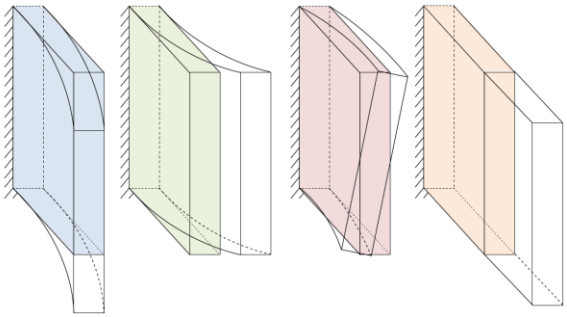

Figure 1-2: Modes of Excitation (Left to Right): Lateral (In-Plane), Transverse (Out-of-Plane), Torsional, and Axial

The deflection of the cantilever (in either static or dynamic mode) can be measured using a variety of techniques. Two relevant methods for this research include optical (detection via laser tracking of the tip of the cantilever) and piezoresistive (monitoring of strain-induced electrical changes via the use of piezoresistors near the support).

Microsensors have been used in both gas and liquid environments. In the case of gas-phase applications the most common mode that is dynamically excited is the transverse (i.e., out-of-plane) flexural mode. Excitation of this mode in a gas is facilitated by the fact that bending occurs about the weak axis and, as a result, this tends to be the "natural" or most easily excited mode. However, the performance of transverse-mode microcantilever-based sensors operating in liquid environments will be severely compromised due to the reduced resonant frequencies and quality factors caused by the liquid's added inertia and viscous energy dissipation. Although consideration of microcantilever-based sensors for liquid-phase sensing is of high interest due to the myriad of applications, it is important to note that the transverse-mode operation of a cantilever in a liquid negatively impacts the oscillatory response, often significantly, due to its "unstreamlined" orientation [Dufour et al., 2007a]. It has been observed that the quality factor of such a device is reduced by a factor of 10-100 in transitioning from gas to liquid [Chen, et al., 1994]. The in-fluid response (i.e., resonant frequency and quality factor) is reduced as a result of the added mass and damping associated with the fluid [Dufour et al., 2010; Cox et al., 2012]. In an effort to improve quality factor and, thus, the limit of detection (LOD), particularly in liquid sensing, the lateral mode of vibration may be employed. In fact, the use of this alternative mode has been shown experimentally [Beardslee et al., 2010a-d; Beardslee et al., 2012] and theoretically [Heinrich et al., 2010a, b; Cox et al., 2012] to improve sensing characteristics.

1.2 Motivation for Present Study

In-fluid chemical and biochemical sensing is an active and rapidly developing arena, resulting in the almost ubiquitous presence of MEMS in a variety of diagnostic, monitoring, and security applications. However, as noted earlier, a liquid environment poses significant challenges for dynamic-mode microcantilever-based sensors due to the drastic reduction in resonant frequency and quality factor that occurs. Recent research by the Marquette University/Georgia Tech/University of Bordeaux team [e.g., Dufour et al., 2004, 2007a, 2010; Vancura et al., 2008; Heinrich et al., 2010a,b; Beardslee et al., 2010d; Cox et al., 2012] has suggested that in-fluid sensor performance, especially in liquids, can be improved by utilizing lateral (in-plane) flexural motion in lieu of the conventional out-of-plane bending mode. Figure 1-3 shows an image of one of the group's microcantilever-based sensors with thermoresistors near the support for electrothermal lateral actuation and Wheatstone bridge for motion detection [Beardslee et al., 2010a]. This mode of vibration can reduce both the damping resistance and inertial effects of the

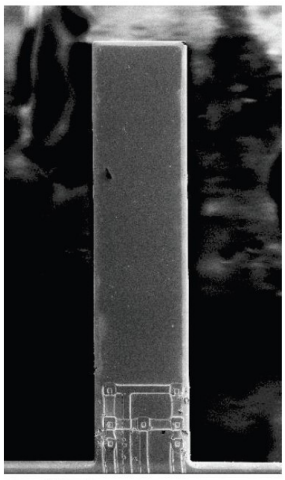

Figure 1-3: SEM Image of Microcantilever-based Chemical Sensor with Thermal Resistors for Lateral Actuation and Wheatstone Bridge for Motion Detection [Beardslee et al., 2010a]

fluid as compared to that of transverse (out-of-plane) motion, providing higher resonant frequencies and improved quality factors (sharper resonant peaks) which result in improved

sensor performance. In particular, the theoretical work by the group [Heinrich et al., 2010a,b] shows that the lateral-mode microcantilever designs offering the most promise in liquid-phase sensing applications are those for which the micro-beams are relatively short and wide. However, those conclusions were based on an Euler-Bernoulli beam theory whose accuracy is known to deteriorate for short, wide beams deforming in the lateral mode. This accuracy loss is due, at least in part, to the effects of shear deformation and rotatory inertia ("Timoshenko beam effects"), which are not considered in Euler-Bernoulli theory. In fact, discrepancies in theoretical and experimental trends for resonant frequency and quality factor arise as the beams become shorter and wider [Heinrich et al., 2010a,b; Beardslee et al., 2010a,b; Cox et al., 2012]; therefore, the development of a theoretical model for the beam/fluid interaction of a lateral-mode microcantilever – that also accounts for shear deformation and rotatory inertia – would be an important theoretical contribution to the fundamental mechanics literature as well as to the body of knowledge on microcantilever-based sensors. The derivation of such a model is therefore, the primary goal of the present dissertation. The inclusion of fluid effects in the derivation of this beam theory is of paramount importance due to the comparatively large energy losses associated with the fluid for beams vibrating in liquids in comparison with other loss mechanisms (i.e., internal damping, support losses, etc).

From a sensing perspective, the development of a Timoshenko beam model for the forced vibration of a lateral-mode microcantilever in a viscous fluid is needed because the improved estimates of resonant frequency and quality factor that would be furnished by such a model may be directly related to sensor performance metrics such as mass sensitivity, chemical sensitivity, and limit of detection (LOD). In the present study such a model will be achieved in a rigorous manner by the application of first principles, thereby contributing to an improved understanding of fluid-solid interaction for microcantilevers vibrating laterally in viscous fluids and, thus, a theoretical basis for improved designs of microcantilever-based chemical sensing devices.

1.3 Specific Objectives of Present Study

The objectives of this research are three-fold: (1) to perform detailed derivations from first principles of several boundary value problems (BVPs) for different loading and environmental conditions that are particularly relevant to sensing applications; (2) to obtain analytical solutions to the BVPs and use these solutions to generate numerical results for key features of the vibrational response (e.g., resonant frequency and quality factor) to investigate the impact of Timoshenko parameters and other material and geometric parameters on beam response; and (3) to relate the new theoretical results for microbeam response in viscous fluids to the performance of laterally excited microcantilever-based liquid-phase sensors.

By combining Timoshenko beam theory, which accounts for the shorter, wider beams by the inclusion of shear deformation and rotatory inertia effects, with a Stokes-type fluid resistance assumption, an improved model will be derived for dynamic mode, in-fluid operation of lateral-mode microcantilever-based chemical sensors. This model will also be verified by reduction to theoretically known limiting cases such as the Euler-Bernoulli model for both in-vacuum and in-fluid operation.

As part of the dissertation research, several boundary-value problems (BVPs) will be derived for a Timoshenko cantilever beam under the following load and environmental conditions:

(a) Free Vibration in Vacuum

(b) Forced Vibration via Harmonic Tip Load in Vacuum

(c) Forced Vibration via Rotational Support Excitation in Vacuum

(d) Forced Lateral-Mode Vibration via Harmonic Tip Load in Viscous Fluid

(e) Forced Lateral-Mode Vibration via Rotational Support Excitation in Viscous Fluid

For the case of in-vacuum, free vibration, the following results are obtained and compared to results found in literature:

(a) The beam response, in terms of total deflection $v(x,t)$ and beam rotation $\varphi(x,t)$, as a function of both the position along the beam (i.e., mode shapes) and time.

(b) The natural frequencies and the impact of Timoshenko parameters on natural frequencies in comparison with the results of the EB model.

For the cases of in-fluid, forced vibration (harmonic tip load and harmonic support rotation), the impact of Timoshenko and fluid resistance parameters on the theoretical results are presented. The results include:

(a) The beam response, in terms of total deflection $v(x,t)$ and beam rotation $\varphi(x,t)$.

(b) The resonant frequencies for in-plane excitations, obtained by plotting the beam displacement over a range of exciting frequencies, and comparing the theoretical resonant frequency results to experimental data.

(c) The quality factor, Q, based on applying the 3-dB bandwidth method to the theoretical frequency response curves, and comparing to experimental data.

(d) The mass sensitivity, S_m, determined using the change in resonant frequency for a given sorbed mass. The method for conversion of mass sensitivity to chemical sensitivity is also provided.

(e) Finally, the limit of detection, LOD, will be related to the resonant frequency, quality factor and chemical sensitivity.

Regarding (d) and (e), only illustrative example calculations will be presented for mass sensitivity and LOD, i.e., comprehensive parametric studies will not be performed for these sensor performance metrics. Nevertheless, the results presented herein lay the groundwork for these types of exhaustive studies to be performed in the future as the mass and chemical sensitivities and the LOD are related to the resonant frequency and Q in specific ways as presented in the latter part of this dissertation. Thus, an improved model for the theoretical prediction of resonant frequency and Q , the primary objective of the present study, will translate to improved estimates of the sensitivities and the LOD.

1.4 Literature Review: Experimental Research and Analytical Modeling

The following literature review focuses on the state of experimental and analytical modeling of microcantilever-based sensors by tracing the evolution of transverse-mode AFM microcantilevers in gaseous and fluid environments to lateral-mode microcantilever-based sensors in fluids. First, experimental and analytical work relating to AFM is summarized and related to the development of transverse-mode sensing applications. Second, the experimental and analytical work focusing on transverse in-fluid microcantilever sensors is surveyed and related to recent experimental work on in-fluid microcantilever-based sensors excited in the lateral mode. As a result of the lateral-mode experiments, some EB analytical methods have been developed. It is important to note that much of the existing analytical work for both transverse and lateral modes of vibration employs EB theory which may not be applicable for certain lateral mode geometries. As a result, this review concludes with an overview of Timoshenko beam theory and recent applications to microsensors.

Initial investigation of in-fluid, microcantilever-based behavior stems from AFM applications [Barnes et al., 1994; Thundat et al., 1994; Thundat et al., 1995]. As a result, the predominant mode of excitation for a preponderance of the initial literature is that of the transverse (i.e., out-of-plane) flexural mode. The concomitant boundary conditions (BCs) are typically either that of a traditional fixed-free cantilever or elastic spring stiffness at the cantilever tip, representing the AFM interactions. In the early 1990s, it was observed that microcantilevers employed in AFM offer interesting possibilities as chemical sensors due to apparent resonant frequency changes with adsorption of mercury. Since these experiments were performed in the presence of vapors containing mercury mixtures it was also observed that the deflection (for static-mode operation) and frequency shift (for dynamic-mode operation) were significantly dependent on thermal and humidity parameters [Thundat, 1994]. While studying AFM cantilevers, Schaffer noted that submersion in liquids significantly altered the vibrational

response [Schaffer et al., 1996]. The observed resonant frequencies were lower in water than in air and the concomitant quality factors were reduced by factors ranging from 10-100, due to the hydrodynamic fluid resistance. In order to address the fluid effects, investigations were made into a transverse tapping-mode of operation which increased quality factors, although not to previous in-gas or in-vacuum levels [Chen et al., 1994]. With the importance of beam response dependence on fluid parameters becoming increasingly evident as a result of experimental work, Sader presented a detailed theoretical analysis of the frequency response of a forced vibration of a cantilever beam in a viscous fluid with an arbitrary external driving force [Sader, 1998]. This analysis focused on the effects of beam geometry and fluid parameters on the vibrational response by introduction of the hydrodynamic function to account for dependence of the fluid effect on the cross-sectional geometry. Due to the particular relevance to AFM applications, the particular case of out-of-plane flexural-mode vibration (for the case in which length L greatly exceeds the cross-sectional dimensions) cantilevers of arbitrary cross section was studied, with particular emphasis on circular and thin rectangular cross sections. Subsequent research investigated the hydrodynamic model of fluid-structure interaction for cases of cylinders near a wall [Green and Sader, 2005], transverse and torsional oscillation of flexible blades in an inviscid fluid [Van Eysden and Sader, 2006], higher-order modal response of flexible blades in a viscid fluid [Van Eysden and Sader, 2007] and the oscillation of rectangular cylinders of arbitrary aspect ratio [Brumley et al., 2010]. Ghatkesar et al., [2008] investigated the transverse (i.e., out-of-plane) vibrational response of resonant-mode microcantilevers by using Sader's extended viscous model [Van Eysden and Sader, 2007] to provide theoretical comparison for Ghatkesar's experimental results (quality factor and resonant frequency). Using an array of microcantilevers and optically measuring the tip response, the quality factors were obtained. The results for the quality factor ranged between 1-30 for modes 1-16 [Ghatkesar et al., 2008]. Such values demonstrated again the significantly lower values for in-fluid quality factors compared to in-air. The results also demonstrated the increase of quality factor and resonant frequency with higher

modes of vibration. While higher-mode operation may be desirable (due to increased sensing stability, reduced added fluid mass and a concomitant increase in mass sensitivity), the feasibility of excitation and measurement remains challenging due to higher resonant frequencies and smaller vibration amplitudes associated with higher modes.

In an effort to achieve a simplified approach to the modeling of the fluid, recent work [Heinrich et al., 2010a, b] applies the solution of Stokes second problem [Stokes, 1851 or, e.g., White, 2006] to the case of in-fluid, lateral vibration of microcantilever-based sensors. This method focuses on the fluid effects on the wide faces of the beam and neglects the fluid pressure effects on the narrow sides of the beam. Accordingly, it is expected that this approximate method will be most effective for thin, laterally vibrating microcantilevers and will over-predict the resonant frequency and quality factor as the thickness is increased. Initial work has shown that this assumption greatly simplifies the fluid-structure interaction and leads to simple analytical results for the quality factor that are of reasonable accuracy for commonly encountered lateral-mode microcantilever-based sensor geometries and associated fluid resistance parameters [Heinrich et al., 2010b].

As noted earlier, Sader considered the vibrational response of an out-of-plane microcantilever in the presence of a viscous fluid for the AFM application [Sader, 1998]. However, unlike the homogeneous beam considered by Sader, the microcantilever-based sensor is coated with a chemically sensitive, and possibly viscoelastic, layer. Research into the generalized equations of motion shows the impact of non-mass loading effects and the viscoelastic sensing layer on resonant frequency and quality factor for the forced vibration of microcantilever-based chemical sensors [Cox et al., 2007]. In addition to the effects of the sorption of chemical analytes, the apparent vibrational response dependence on the width for in-fluid, out-of-plane sensors is noteworthy. Experimental data for transverse vibrations shows that increasing the cantilever's width increases the added fluid mass and results in decreases in the

resonant frequency while increasing the width results in an increase in quality factor [Vancura et al., 2008].

Optimization of the quality factor is a significant part of sensor design, particularly for in-fluid applications, and in order to maximize quality factors, all energy losses should be evaluated [Naeli and Brand, 2009]. Typical losses include those associated with the surrounding medium, the beam support, thermoelasticity, volume losses (e.g., viscoelaticity), and surface losses. However, for in-fluid applications, the losses due to damping from the fluid usually dominate and render other losses negligible. Consequently, there is a significant focus on the effects of fluid resistance on the frequency shift of these types of sensing devices. Both continuous and single-degree of freedom (SDOF) models have been developed which include the fluid effects either through the hydrodynamic function [Cox et al., 2008] or through generalized damping and mass coefficients [Lin, 2010]. Lin presents an analytical solution for his AFM system (which also includes the effects of an angle of inclination), which includes the results for quality factor as obtained using a generic damping coefficient that is not correlated to the fundamental fluid properties. However, his solution for the AFM boundary value problem considers the transverse vibration based on Euler-Bernoulli theory of a modified cantilever with a spring stiffness at the tip.

In an effort to mitigate some of the negative fluid effects on sensor performance, several groups [e.g., Basak et al., 2006; Dufour et al., 2007a; Beardslee et al., 2010a] have investigated excitation of resonant microcantilever-based sensors in unconventional modes. Work by Basak et al. [2006] investigated the in-fluid lateral vibration of microcantilevers using three-dimensional finite element modeling. Additionally, this work investigated various cantilever geometries (e.g., "slotted," "paddle" and "triangular") and presented suggestions for optimization of geometries for lateral-mode vibrations. Recent experimental investigations have shown that the lateral mode of excitation for microcantilevers improves the quality factor in both air and liquid environments compared to transverse modes [Beardslee et al., 2010a]. Since the vast majority of prior research

has investigated the transverse mode, sensing applications for this mode have remained largely limited to air and other gas environments due to the pronounced negative effects of a liquid. However, by exploring "unconventional" modes of operation like transverse and extensional modes, the effects of the fluid are reduced as compared to the more common transverse mode [Dufour et al., 2007a]. By investigating the lateral mode, the negative impacts of added mass and damping are minimized due to reduction of the vibrating profile in the fluid. As a result, advantages of the lateral mode sensor, including improved quality factor (i.e., better frequency stability) and increased vibrational stiffness leading to higher resonant frequency, serve as motivation for further study. Such studies have included geometrical optimization for improved quality factor [Beardslee et al., 2010a] and compared theoretical results with experimental data [Beardslee et al., 2010c; Cox et al., 2012].

In order to more completely model the lateral vibration of a thermally excited microcantilever, Heinrich et al. [2010b] derived a multi-mode continuous system model that incorporated frequency-dependent damping and fluid mass coefficients based on a Stokes-type fluid resistance assumption. The resulting frequency and quality factor plots were obtained and compared to a previously derived SDOF model based on the use of the fundamental, in-vacuum mode shape of an Euler-Bernoulli beam [Heinrich et al., 2010a]. The results showed good agreement with the previous research and while the continuous model provides some additional results (i.e., frequency and quality factor at multiple, not just the first, resonant peaks) it largely served to verify the applicability of the SDOF model for particular microsensor applications. Note that some experimental work done [Beardslee et al., 2010a-d] employs excitation via thermo-resistors near the support like the device shown in Fig. 1-3. Consequently, the analytical investigation by Heinrich et al. [2010b] is significant in that it takes into account the specific method of excitation, i.e., the authors model the electrothermal loading of the actual devices as an equivalent imposed support rotation of the microcantilever, which is a more realistic, mechanics-based representation of the load than the tip force loading that was considered in the earlier paper

[Heinrich et al., 2010a]. While a point load at the tip may be an accurate method for representing AFM applications and other means of sensor excitation (like motion induced via Lorenz forces as depicted for the transverse mode in the device of Fig. 1-1), the microcantilever-based sensors employed by colleagues at Georgia Tech are more appropriately modeled by an equivalent support rotation [Heinrich et al., 2010b].

While the lateral mode of vibration alleviates some of the adverse fluid effects by reducing the area of the microcantilever exposed to the pressure effects of the fluid, i.e., "slicing" through the liquid, it also introduces some challenges for models that employ Euler-Bernoulli beam theory. This difficulty is highlighted by revisiting the aforementioned geometric optimization and modeling: laterally vibrating microcantilever-based sensors operating in viscous fluids yield higher quality factors and higher resonant frequencies as the length decreases and the width increases [Beardslee et al., 2010a; Heinrich et al., 2010a, b; Cox et al., 2012] and these enhanced resonant characteristics may result in improved sensor performance. However, the optimized sensor geometries violate the geometric limitations of Euler-Bernoulli theory due to their large width-to-length ratio. This can be observed in the deviation between predicted and experimental frequencies for short, wide cantilevers in which the EB theory overestimates the frequency. In order to accurately model the more ideal sensor geometries, a more exact beam model is required [Beardslee et al., 2010a]. Consequently, the incorporation of an improved theory, known as Timoshenko beam (TB) theory, is warranted and provides the motivation for the current study. Therefore, the remainder of the literature review will focus on the differences between TB theory and Euler-Bernoulli (EB) theory and the application of TB theory to in-fluid, microcantilever-based sensors.

An improved beam theory, incorporating shear deformation and rotatory inertia, was first published nearly a century ago [Timoshenko, 1921] and has been studied extensively in various applications since its introduction. While Euler-Bernoulli theory only considers bending deformation and transverse inertial effects, Timoshenko beam theory includes the shear

deformation and rotatory inertia terms. In addition to the inclusion of these terms, Timoshenko also demonstrated that for vibrational responses of prismatic beams the effect of transverse shear is greater than the effect of the rotatory inertia [Timoshenko, 1921; Ghugal and Sharma, 2010]. As a result of omitting these additional effects, EB theory is less accurate than TB theory for static and dynamic problems, particularly those with small geometric ratios of length-to-depth since small length-to-depth ratios result in behavior that is increasingly influenced by shear and rotatory inertia effects. Moreover, in dynamic problems, particularly those considering higher modal excitation, EB theory tends to overestimate the resonant frequencies due to the artificially high stiffness of the Euler-Bernoulli model. However, while inclusion of the shear and inertial terms improves the accuracy compared to EB theory, it is important to note that the TB theory still has limitations associated with its assumptions. Notably, some authors [e.g., Ghugal and Sharma, 2009] point out that TB theory assumes constant distribution of transverse shear strain over the cross section, incorporated into the theory through the use of the shear coefficient, k. This factor is used to account for the strain energy due to the relative shearing of cross sections; however, it does violate the surface boundary conditions that specify shear stress of zero at the "extreme fibers" of the cross section. Originally, Timoshenko assumed a value of $k = 2/3$ for the shear coefficient for rectangular cross sections. In subsequent years, significant discussions ensued regarding the appropriate values for k based on cross-sectional shape in order to account for the shear effects. Cowper originally derived improved equations for the shear correction factor, and when the value of Poisson's ratio is taken as zero, his result for a rectangular cross section reduces to the widely used value of $k = 5/6$. Cowper also compared his results (from a plane stress method) to those of several other authors using exact elasticity solutions [Cowper, 1966]. More recently, Hutchinson has derived analytical expressions for k for several shapes of cross sections. For the case of a rectangle, his analytical results are shown to have dependence on the aspect ratio of the cross section [Hutchinson, 2001]. In that work, the value for a circular cross section is in perfect agreement to that presented originally by Cowper [1966]. For the rectangular

cross section, Hutchinson's shear coefficient matches that of Cowper for the case of a Poisson's ratio of zero.

Since the TB theory more accurately models a beam than EB theory (i.e., it yields a more flexible and more massive system due to additional parameters), it produces improved frequency results. The ramifications of these parameters on the resonant frequency for in-vacuum (i.e., undamped) vibrations were investigated by Kruszewski [1949] and Huang [1961], two references that will be used as benchmarks for the present research. For this reason a detailed derivation of the in-vacuum free-vibration formulation and solution for a Timoshenko beam is included in portions of Chapters 2 and 3 with the solution methodology following the description given by Huang.

A few applications of Timoshenko beam models to the vibration of microcantilevers (in air and in fluid) have been introduced recently [Hsu et al., 2007; Mahdavi et al., 2008; Lee and Chang, 2009; Horng, 2009; Abbasion et al., 2009]. Hsu et al. introduced TB theory to the application of an AFM mechanical machining tip which in addition to having rigidity nearly 1000 times greater than a typical AFM tip, also has significantly larger width to length ratios than commonly encountered in common AFM cantilevers. These increased ratios of width to length necessitate consideration of the shear and rotatory inertial effects by TB theory. In Hsu's research, the boundary conditions also incorporate a contact stiffness at the tip (unlike a cantilever sensor which has zero shear force at the free end) and the focus of the research was on optimization of beam parameters with consideration of various contact stiffnesses. These results reinforced well-known trends: that the effects of the shear and rotatory inertia are increasingly important at higher modes, increasing cross-sectional dimensions increases the resonant frequency, while increasing the length decreases the frequencies. However, the results also introduced some new observations regarding the impact of contact stiffness: the ratio of TB frequencies to EB frequencies is almost linear for low contact stiffness values. Extending the work of Hsu, Mahdavi modeled the AFM cantilever using a continuous TB system incorporating

the shear and rotatory inertia of the cantilever as well as the mass and rotatory inertia at the sensing tip [Mahdavi et al., 2008]. Again, the frequency results verified trends provided in earlier papers [Hsu et al., 2007]. The effects of surface elasticity and residual surface tension on the free vibration of nanoscale beams have also been studied using a Timoshenko model by Abbasion et al., [2009]. Using an energy method, Abbasion et al., developed a model that includes surface tension and shows that the impact of the surface tension is more significant in lower modes than in higher modes. It was also found that when the beam length increases from nano- to microscale the surface effects disappear and converge to that of a TB model without surface effects [Abbasion et al., 2009]. While these studies employed the TB theory with respect to modeling the continuous cantilever system, important damping effects inherent in the beam and due to surroundings (fluid, support, etc.) were neglected. In 2009, Lee and Chang studied fluid effects by incorporating a generic distributed damping coefficient [Lee and Chang, 2009]. While this work was able to show a strong impact of the fluid resistance on the structure's vibration frequency, the model employed an independent damping parameter whose value was not directly related to the fluid properties or to the frequency of vibration. Moreover, Lee and Chang neglected the added mass due to hydrodynamic interaction for simplification. However, it has been well documented that the added fluid mass is not negligible for many sensor geometries and operating frequencies and should be included [Sader, 1998; Van Eysden and Sader, 2007; Heinrich et al., 2010a, b]. It is also noteworthy that additional work has been done employing TB theory for an AFM cantilever with a tip load, which includes a generic damping coefficient that is not directly dependent on fluid properties or beam frequency [Horng, 2009] and also models which neglect damping altogether [Horng, 2011].

Based on the preceding literature review, the current state of the in-fluid, lateral vibration of a microcantilever-based chemical sensor has been described from experimental and analytical perspectives. The results indicate that the ideal geometry (short and wide) of these devices tends to violate the assumptions undergirding the EB theory on which most of the current models are

based. The few models that do employ TB theory remain too generic to have predictive capabilities for the application of interest herein because they: (1) use a generic, frequency-independent fluid damping parameter (or neglect damping altogether), (2) model AFM boundary conditions as opposed to those applicable to chemical sensing devices, and/or (3) focus on the transverse mode of excitation. The work presented herein aims to overcome the limitations associated with EB models and the aforementioned TB models.

By deriving the boundary value problem for a Timoshenko beam and incorporating a frequency-dependent distributed fluid resistance parameter (which incorporates the translational and rotational damping due to the fluid), the current research seeks to establish an improved analytical model for lateral vibration of short, wide beams excited by either a harmonic tip load or a harmonic support rotation. Inclusion of a frequency-dependent fluid resistance parameter based on the solution to Stokes's second problem will help to develop a much fuller understanding of the interplay of system parameters, including those of the fluid environment (fluid density and viscosity), and how they affect the microcantilever dynamic behavior and, therefore, the performance characteristics of microcantilever-based chemical sensors.

1.5 Problem Statement

This research focuses on deriving theoretical models for determining the in-plane vibrational motion of a microcantilever beam in a viscous fluid, the motion being caused by two particular forms of in-plane loading: (a) a harmonically varying tip force, and (b) a harmonically varying rotation at the supported end. Here, "in-plane" refers to the plane of the thin beam that is being considered; this plane is denoted as the x-y plane throughout. Figures 1-4 and 1-5 define the geometric, material, and loading parameters to be considered as well as the reference axes.

The derived models will incorporate the effects of shear deformation and rotatory inertia in the beam ("Timoshenko beam effects") and the effects of the surrounding viscous fluid. The

boundary value problems (BVPs) associated with the dynamic motion of the beam/fluid system will be formulated and solved. Quantities of particular interest will be extracted from the time-

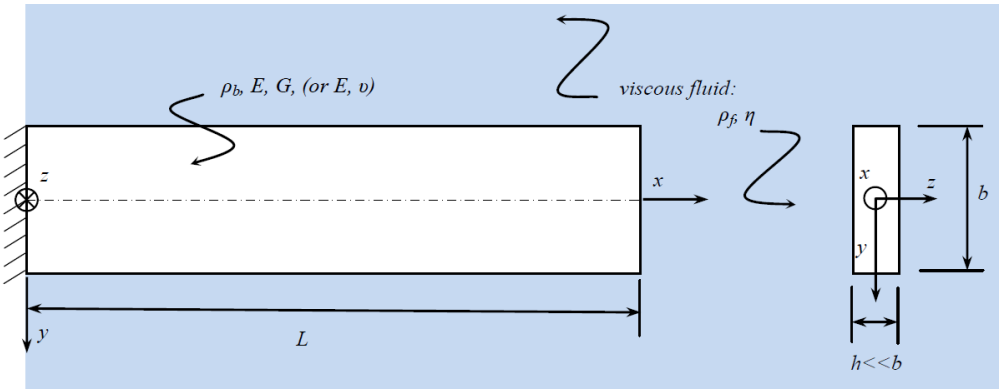

Figure 1-4: Definitions of Geometry and Material Parameters

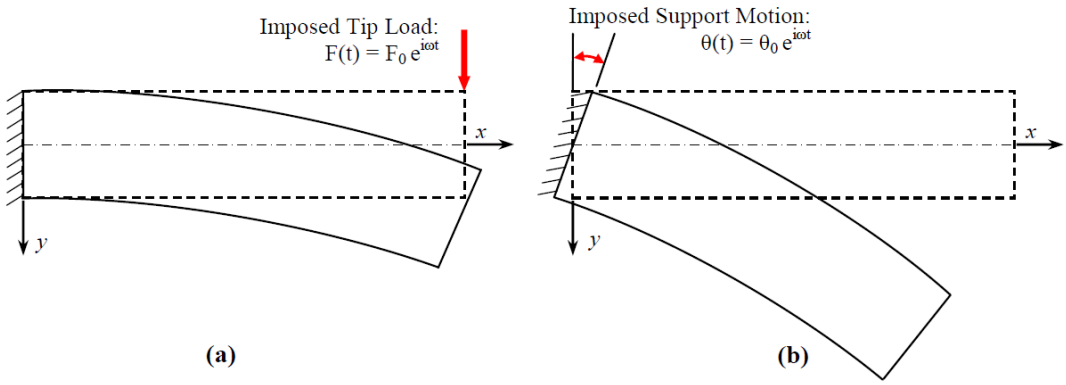

Figure 1-5: (a) Load Case 1 – Imposed Harmonic Tip Load
(b) Load Case 2 – Imposed Harmonic Support Rotation

and space-dependent beam motion. The results that will be presented will be based on normalized forms of two particular response quantities: (1) the total displacement at the beam tip, $v(L,t)$, and (2) the bending-deformation displacement, $v_{B-D}(L,t)$, at the beam tip, i.e., the portion of the tip displacement due to bending deformation *only* (not due to shear deformation or rigid body rotation). To further elaborate on the load types considered and the output quantities of interest, some comments on the problem kinematics are in order.

For the case of an imposed support rotation (see Figs. 1-5b and 1-6), the total displacement, $v(x,t)$, includes displacements due to both shear, $v_S(x,t)$, and bending, $v_B(x,t)$, while the bending displacement, $v_B(x,t)$, includes displacements due to both rigid body rotation, $v_R(x,t)$, and bending *deformation*, $v_{B-D}(x,t)$. The total displacement at the tip is the relevant response quantity for sensor applications that utilize optical (laser) system monitoring of total tip displacement (or total tip slope, which is proportional to total tip displacement) [Lavrik et al., 2004], while the bending-deformation displacement at the tip (bending displacement less the effect of the rigid body motion) in the vicinity of a resonant peak is approximately proportional to the beam's bending strain, which for some sensors is monitored by piezoresistive elements near the beam support [e.g., Beardslee et al., 2010a]. (This proportionality is a result of the vibrational shape due to bending being relatively constant.) Since optical tip measurement may be difficult to implement for lateral vibrations in liquids, the experimental scheme utilized in the lateral-mode devices tested at Georgia Tech (e.g., [Beardslee et al., 2010a]) detects beam motion via piezoresistive elements (acting as extensional strain gauges at the beam's "extreme fibers") near the microcantilever support. As such, it is important to model an output that is proportional to the measured quantity (i.e., bending strain), the bending-deformation displacement at the tip serving as such a quantity.

For the case of a harmonic tip force loading (Fig. 1-5a), similar comments apply as in the previous paragraph; however, there is now no rigid body rotation to consider; thus, the level of bending strain in the beam for this case can be monitored by simply focusing on the value of $v_B(L,t)$, i.e., simply taking $v_{B-D}(L,t) = v_B(L,t) - v_R(L,t) = v_B(L,t) - 0 = v_B(L,t)$.

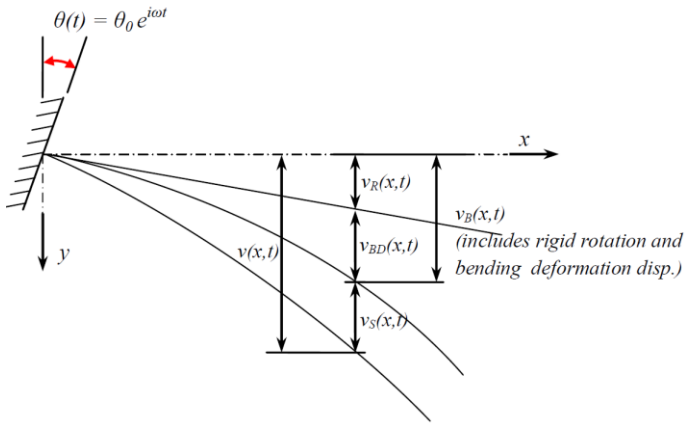

Figure 1-6: Total Deflection Composed of Rigid, Bending-Deformation, and Shear Components

For the two loading cases (tip force and support rotation) and the two output quantities [$v(L,t)$ and $v_{B-D}(L,t)$] the following quantities will be obtained: the resonant frequency (i.e., the exciting frequency that causes maximum displacement response) and the quality factor associated with viscous losses in the surrounding fluid, with the primary emphasis on the fundamental (i.e., mode-1) in-plane flexural response.

As noted above, solutions will be derived for two different methods of microcantilever excitation: a harmonic tip force loading and a harmonic rotational support excitation. These loading cases are considered because they are two of the more commonly used types of excitations in microcantilever-based sensing applications. The first load case arises often in atomic force microscopy (AFM) applications (in which the cantilever interacts with a surface at its tip) and is also the load type that is often induced when electromagnetic actuation methods are used for sensing applications. The motivation for the second loading case is provided by recent successes in lateral-mode sensor development [e.g., Beardslee et al., 2010a] in which electro-thermal excitation has been utilized near the cantilever support, which can be represented kinematically as an imposed harmonic rotation at the support [Heinrich et al., 2010b]. Results for the two loading cases will be compared with each other and to previously derived solutions [e.g., Heinrich et al., 2010a, b]. The resonant frequency and quality factor results will also be related to

the sensor performance metrics of sensitivity and limit of detection (LOD) for those cases in which the microcantilever is utilized for chemical, mass, or biological sensing purposes; the focus herein will be on chemical sensing applications. The numerical results generated from the new analytical solutions derived in this study will be confirmed by comparing with the results of numerical simulation. Also, the new theoretical results will be compared to existing experimental data to see what improvements, if any, are furnished by the new model in comparison with existing Bernoulli-Euler beam models.

1.6 Organization of Dissertation

The overall structure of the dissertation begins with the derivation of the mathematical formulations of the relevant BVPs (both dimensional and non-dimensional forms), followed by the derivations of the solutions of the BVPs and subsequent presentation, discussion, and verification of numerical results.

Chapter 2 opens by presenting the modeling assumptions for system geometry, material properties and loading cases. Next, the equation of motion (EOM) for in-vacuum, lateral (i.e., in-plane) vibration of cantilever beams due to harmonic loading is derived by following Timoshenko [1921, 1922], Kruszewski [1949] and Huang [1961]. The in-vacuum EOM is presented as both a single fourth-order equation and as two second-order equations. The fourth- and second-order forms of the equations are equivalent and are presented for completeness and to facilitate comparison to literature. Both forms are converted from dimensional to non-dimensional equations for use in the remainder of the dissertation. Once the in-vacuum case is established, the EOM for the in-fluid case is obtained by inclusion of translational and rotational Stokes-type fluid effects. Again, the EOM for the in-fluid case is presented as both fourth- and second-order equations in dimensional and non-dimensional form. Finally, the BCs are derived for the cases of free vibration of a cantilever, a tip-loaded cantilever, and a cantilever excited by an imposed support rotation. The complete BVP for the Timoshenko cantilever in a viscous fluid is verified

by reduction to a Timoshenko system in a vacuum, which, in turn, is reduced to the familiar Euler-Bernoulli system in vacuum.

Chapter 3 presents derivations of the solutions of the BVPs that are formulated in Chapter 2. Initially, the classical solution to the in-vacuum, free vibration case [Kruszewski, 1949; Huang, 1961; Huang 1963] is reproduced. This is followed by the derivation of new solutions for the forced vibration (via harmonic tip load and support rotation) of a laterally vibrating Timoshenko beam in a fluid environment. Once the in-fluid forced vibration cases have been solved, the in-vacuum cases may easily be obtained for the two specific forms of excitation by setting the fluid resistance parameter equal to zero.

Chapter 4 discusses the results obtained from the new analytical solutions obtained in the preceding chapter. The results include the following system response quantities: frequency response curves of tip displacement, resonant frequencies, quality factors, and vibrational shapes. These results are compared with the following: (1) in-vacuum Timoshenko theory results, (2) recent results in the literature for the in-fluid case based on Euler-Bernoulli theory, (3) results for the in-vacuum case based on Euler-Bernoulli theory, (4) numerical simulation results utilizing MATLAB, and finally, (5) the theoretical resonant frequency and quality factors are compared to experimental data.

Application of the frequency and quality factor results to microcantilever-based chemical sensors requires that they be correlated to mass sensitivity, chemical sensitivity, and limit of detection (LOD) for the Timoshenko beam for in-fluid conditions. Chapter 5 summarizes the necessary relationships among resonant frequency, Q, LOD and the sensitivities to indicate how improved accuracy in theoretical determination of the resonant frequency and Q can influence theoretical estimates of sensor performance as measured by the LOD and the sensitivities.

Finally, Chapter 6 summarizes the main conclusions of this study and makes recommendations for future work.

CHAPTER 2: BOUNDARY VALUE PROBLEM (BVP) OF A THIN TIMOSHENKO CANTILEVER BEAM VIBRATING LATERALLY IN A VISCOUS FLUID

2.1 Introductory Remarks

In Chapter 2 the boundary-value problems (BVPs) of a thin Timoshenko beam (TB) vibrating laterally are explicitly formulated for both the in-vacuum and in-fluid cases. The equations of motion (EOMs) are derived by employing d'Alembert's principle and using the Newtonian method (force and moment equilibrium on a differential element). Resulting EOMs are presented as both a pair of second-order partial differential equations (PDEs) and a single fourth-order PDE. These equations are derived in dimensional form and then converted to non-dimensional form for simplicity and convenience of parametric studies in subsequent chapters. Finally, the concomitant initial conditions are discussed and boundary conditions are derived. Both are presented in dimensional and non-dimensional form. Three forms of excitation are examined and addressed via the EOMs and boundary conditions: free vibration (for the in-vacuum case), forced vibration by a harmonic tip load and forced vibration by an imposed harmonic support rotation.

2.2 Modeling Assumptions

Mathematical modeling of any physical system involves the intelligent conversion from an infinite reality to a limited mathematical model. The physical system of the microcantilever (MC) and surrounding medium (either vacuum or viscous fluid) is idealized by employing the following assumptions:

1. The beam is homogeneous and made of a material that is linear elastic and isotropic. (Thus, when applied to silicon – an anisotropic material – care must be taken in utilizing the appropriate elastic moduli in the isotropic model.) In addition, the beam is assumed to

be of rectangular cross section and prismatic, i.e., the cross section is uniform along the beam length.

2. The slope of the deformed beam centerline is much smaller than unity.
3. The beam has a condition of perfect fixity (i.e., zero displacement and bending slope) at one end.
4. The loading is harmonic and applied in-plane, resulting in only in-plane flexural/shear deformation. Similarly, for any free-vibration cases considered, only vibrations involving in-plane flexural/shear deformation are considered.
5. The cross section is relatively thin, i.e., $h<<b$, so that the fluid resistance associated with the pressure on the smaller faces (of dimension h) is negligible compared with that due to the fluid's shear resistance on the larger faces (of dimension b).
6. The shear stress exerted by the fluid on the beam is modeled as fluid damping and fluid mass terms that are obtained from the solution of Stokes's second problem for harmonic, in-plane oscillations of an infinite rigid plate in a viscous fluid [Stokes 1851; e.g., White 2006.]
7. For the in-fluid case, it is assumed that viscous energy losses in the fluid are the dominant loss mechanism, i.e., all other losses are neglected.

The combination of assumptions 5 and 6 will be referred to as the assumption of "Stokes fluid resistance," which is a generalization of the assumption made in Heinrich et al. [2010a, b] for Bernoulli-Euler beam theory to the case of Timoshenko beam theory. The assumption of Stokes fluid resistance should be valid for sufficiently thin beams at sufficiently high Reynolds numbers.

2.3 Derivation of Governing Equations for In-Vacuum Case

Both the dimensional and the non-dimensional second- and fourth-order PDEs are derived as follows for the in-vacuum case, as these will be used as a baseline for comparison of the subsequent in-fluid case. The derivations follow the method employed by both Kruszewski

[Kruszewski, 1949] and Huang [Huang, 1961], which were based on the original contributions of Timoshenko [Timoshenko, 1921; Timoshenko, 1922].

2.3.1 Dimensional Equation of Motion for In-Vacuum Case

The derivation of the BVP for the in-vacuum case begins with the determination of the equations of motion (EOMs) for the beam shown in Figure 2-1, in which all quantities are shown in their positive directions:

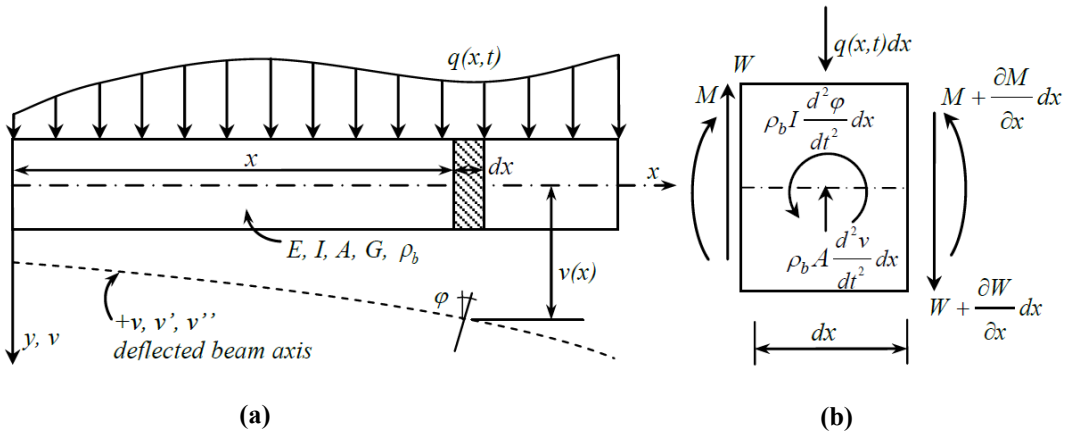

Figure 2-1: Idealized System for Newtonian Method of EOM Derivation: (a) Beam, (b) Differential Element

Relevant notation for Figure 2-1 is as follows:

E = modulus of elasticity of the beam material,

I = second moment of area of beam cross section,

A = cross-sectional area,

ρ_b = mass density per unit volume of beam material,

$q(x,t)$ = distributed in-plane external loading (applied force per unit length),

$v(x,t)$ = beam displacement in the y-direction,

$\varphi(x,t)$ = angle of rotation of cross section,

G = shear modulus of beam material,

W = transverse shear force,

M = bending moment.

In addition, throughout this dissertation the beam mass per unit length, $\bar{m}_b$, will be referred to at times, where $\bar{m}_b \equiv \rho_b A$, or $\bar{m}_b \equiv \rho_b bh$ for a rectangular cross section.

Applying force equilibrium (including the inertial force) on the differential element in Fig. 2-1b results in the following force balance equation:

$$\frac{\partial W}{\partial x} = \rho_b A \frac{\partial^2 v}{\partial t^2} - q(x,t) \tag{2-1}$$

Similarly, moment equilibrium (including the inertial couple and neglecting the higher-order terms) yields

$$W - \frac{\partial M}{\partial x} = \rho_b I \frac{\partial^2 \varphi}{\partial t^2} \,. \tag{2-2}$$

Inclusion of the Timoshenko beam theory considerations for shear deflection and rotatory inertia result in a more accurate description of beam response, especially for relatively deep beams. Accordingly, the total deflection is written in terms of the deflection due to bending and the deflection due to shear as follows:

$$v(x,t) = v_B(x,t) + v_S(x,t), \tag{2-3}$$

where v_b is the deflection due to bending and v_s is the deflection due to shear. The slope of the curve can be described as

$$\frac{\partial v}{\partial x} = \frac{\partial v_B}{\partial x} + \frac{\partial v_S}{\partial x} \equiv \varphi(x,t) + \psi(x,t), \tag{2-4}$$

where φ is the slope of the bending deflection curve, which is the same as the previously introduced cross-sectional rotation angle, and ψ is the slope of the shear deflection curve, which is identical to the angle of shear (i.e., shear strain) at the neutral axis. These separate effects (bending and shear) contribute to the overall displacement as shown in Figures 2-2 and 2-3.

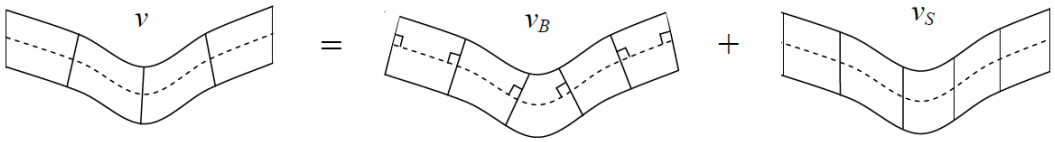

Figure 2-2: Schematic Indicating Bending and Shear Contributions to Total Displacement According to Timoshenko Theory

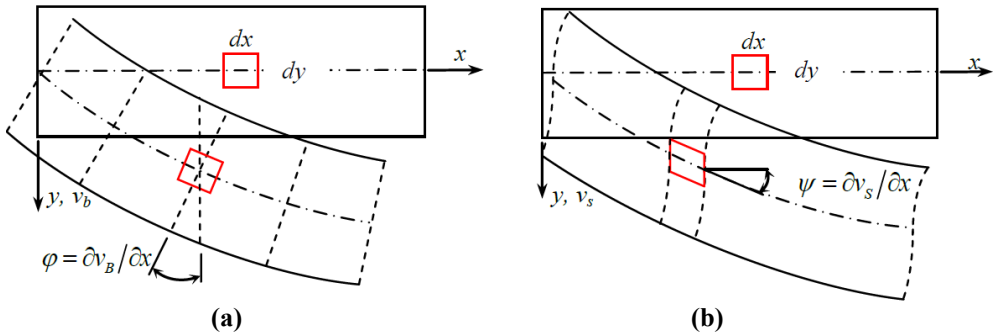

(a) **(b)**

Figure 2-3: Timoshenko Beam Effects: (a) Rotatory Inertia is Due to Rotation of Cross Sections; (b) Shear Deformation is Due to Relative Cross Sectional "Sliding"

Employing elementary mechanics of materials, the moment-curvature relationship is

$$M = -EI\frac{\partial \varphi}{\partial x}, \tag{2-5}$$

and the shear stress-shear strain relationship takes the form

$$\tau = \frac{W(x,t)}{kA(x)} = G\psi \,, \tag{2-6}$$

where k is a numerical constant that depends on the shape of the cross section to account for the nonuniformity of shear stress [e.g., Cowper, 1966; Renton, 1991; Hutchinson, 2001; Dong, et al., 2010]. When specifying a value of k in this study for a rectangular cross section, the commonly used value of k =5/6 will be employed throughout this work, although the theoretical value of k for a rectangle varies over a small range depending on the method of derivation. Using Eq. (2-4), (2-6) becomes

$$W(x,t) = kAG\left(\frac{\partial v}{\partial x} - \varphi\right). \tag{2-7}$$

Applying (2-5) and (2-7) to (2-1) and (2-2), and assuming a prismatic beam with material properties E and G constant along x and setting $\rho_b = \bar{m}_b / A$ results in the following coupled, second-order PDEs governing the deformation of a Timoshenko beam of arbitrary cross section under the application of an arbitrary distributed load:

$$kAG\left(\frac{\partial^2 v}{\partial x^2} - \frac{\partial \varphi}{\partial x}\right) - \bar{m}_b \frac{\partial^2 v}{\partial t^2} = -q(x,t) \tag{2-8}$$

$$EI\frac{\partial^2 \varphi}{\partial x^2} + kAG\left(\frac{\partial v}{\partial x} - \varphi\right) - \bar{m}_b \frac{I}{A}\frac{\partial^2 \varphi}{\partial t^2} = 0 \tag{2-9}$$

Often in the literature the mathematical model of a Timoshenko beam is expressed as two uncoupled fourth-order equations in terms of either total displacement or the rotation angle. Following the description of Timoshenko and Young [Timoshenko and Young , 1955], the equation in terms of total deflection may be obtained by first solving (2-8) for $\frac{\partial \varphi}{\partial x}$:

$$\frac{\partial \varphi}{\partial x} = \frac{\partial^2 v}{\partial x^2} - \frac{\bar{m}_b}{kAG}\frac{\partial^2 v}{\partial t^2} + \frac{q(x,t)}{kAG} \tag{2-10}$$

Taking the derivative of (2-9) with respect to x and assuming further that material density, ρ_b, is uniform in x leads to

$$EI\frac{\partial^3 \varphi}{\partial x^3} + kAG\left(\frac{\partial^2 v}{\partial x^2} - \frac{\partial \varphi}{\partial x}\right) - \bar{m}_b \frac{I}{A}\frac{\partial^3 \varphi}{\partial t^2 \partial x} = 0. \tag{2-11}$$

Substituting (2-10) into (2-11) results in the fourth-order PDE that describes Timoshenko beam motion in terms of the total displacement, v:

$$\begin{aligned} &EI\frac{\partial^4 v}{\partial x^4} + \bar{m}_b\frac{\partial^2 v}{\partial t^2} - \frac{\bar{m}_b I}{A}\left(1+\frac{E}{kG}\right)\frac{\partial^4 v}{\partial x^2 \partial t^2} + \frac{\bar{m}_b^2 I}{kA^2 G}\frac{\partial^4 v}{\partial t^4} \\ &= q(x,t) - \frac{EI}{kAG}\frac{\partial^2 q(x,t)}{\partial x^2} + \frac{\bar{m}_b I}{kA^2 G}\frac{\partial^2 q(x,t)}{\partial t^2} \end{aligned}. \tag{2-12}$$

An analogous equation governing φ may be derived using the same method as outlined above:

$$EI\frac{\partial^4 \varphi}{\partial x^4} + \bar{m}_b\frac{\partial^2 \varphi}{\partial t^2} - \frac{\bar{m}_b I}{A}\left(1+\frac{E}{kG}\right)\frac{\partial^4 \varphi}{\partial x^2 \partial t^2} + \frac{\bar{m}_b^2 I}{kA^2 G}\frac{\partial^4 \varphi}{\partial t^4} = \frac{\partial q(x,t)}{\partial x}. \tag{2-13}$$

2.3.2 Non-Dimensional EOM for In-Vacuum case

The dimensional forms of the EOM can be re-written in non-dimensional form by the introduction of the following dimensionless quantities and assuming harmonic loading/response:

$\xi \equiv x/L$ = dimensionless spatial coordinate (2-14)

$\tau \equiv \omega t$ = dimensionless time (where $\omega \equiv$ angular frequency of vibration) (2-15)

$\bar{v} \equiv v/L$ = dimensionless displacement. (2-16)

$q(x,t) = Q(x)e^{i\omega t}$ = distributed load in dimensional form (2-17)

$\bar{q}(\xi,\tau) = \bar{Q}(\xi)e^{i\tau}$ = distributed load in dimensionless form (2-18)

$$\bar{Q}(\xi) = \frac{L^3 Q(x)}{EI} \tag{2-19}$$

Applying (2-14) through (2-19) to (2-8) and (2-9) results in the following dimensionless second-order PDEs:

$$\frac{\partial^2 \bar{v}}{\partial \xi^2} - \lambda^4 s^2 \frac{\partial^2 \bar{v}}{\partial \tau^2} - \frac{\partial \varphi}{\partial \xi} = -s^2 \bar{Q}(\xi) e^{i\tau} \tag{2-20}$$

$$s^2 \frac{\partial^2 \varphi}{\partial \xi^2} - \lambda^4 r^2 s^2 \frac{\partial^2 \varphi}{\partial \tau^2} - \varphi + \frac{\partial \bar{v}}{\partial \xi} = 0 \tag{2-21}$$

where the following non-dimensional parameters have been introduced:

$$r^2 \equiv \frac{I}{AL^2} \equiv \text{ rotational inertia parameter } = \frac{1}{12}\left(\frac{b}{L}\right)^2 \text{ for a rectangular cross section,} \tag{2-22}$$

$$s^2 \equiv \frac{EI}{kAGL^2} \equiv \text{ shear deformation parameter}$$

$$= \frac{1}{12}\left(\frac{b}{L}\right)^2 \left(\frac{E}{kG}\right) \text{ for a rectangular cross section,} \tag{2-23}$$

$$\lambda^4 \equiv \frac{\omega^2 \bar{m}_b L^4}{EI} \equiv \text{ dimensionless frequency parameter}$$

$$= \omega^2 \left(\frac{12\rho_b L^4}{Eb^2}\right) \text{ for a rectangular cross section,} \tag{2-24}$$

and the mass per unit length for a rectangular cross section is

$$\bar{m}_b = \rho_b bh\,. \tag{2-25}$$

Similarly, application of (2-14) through (2-19) to (2-12) and (2-13) results in the dimensionless fourth-order PDEs:

$$\begin{aligned}&\frac{\partial^4\bar{v}}{\partial\xi^4}+\lambda^4\frac{\partial^2\bar{v}}{\partial\tau^2}-\lambda^4\left(r^2+s^2\right)\frac{\partial^4\bar{v}}{\partial\xi^2\partial\tau^2}+\lambda^8r^2s^2\frac{\partial^4\bar{v}}{\partial\tau^4}\\&=\left[\left(1-\lambda^4r^2s^2\right)\bar{Q}(\xi)-s^2\frac{\partial^2\bar{Q}(\xi)}{\partial\xi^2}\right]e^{i\tau}\end{aligned}\tag{2-26}$$

$$\frac{\partial^4\varphi}{\partial\xi^4}+\lambda^4\frac{\partial^2\varphi}{\partial\tau^2}-\lambda^4\left(r^2+s^2\right)\frac{\partial^4\varphi}{\partial\xi^2\partial\tau^2}+\lambda^8r^2s^2\frac{\partial^4\varphi}{\partial\tau^4}=\frac{\partial\bar{Q}(\xi)}{\partial\xi}e^{i\tau}\tag{2-27}$$

2.4 Derivation of Governing Equations for In-Fluid Case

The following is the derivation of the Timoshenko beam (TB) equation of motion with all viscous fluid (mass and damping) effects (translational and rotatory) incorporated via the assumption of Stokes resistance. The TB equation of motion (EOM) is derived using the same method as in Section 2.3 with the inclusion of the additional fluid forces presented below. It is noteworthy that, due to the Stokes fluid resistance assumption, the equations derived in this section are limited to the case of a thin rectangular cross section.

2.4.1 Dimensional Equation of Motion for In-Fluid Case

The fluid resistance effects will be examined by first considering the shear stress, denoted by τ in this section, exerted by the fluid on the vibrating beam due to the transverse deflection of a differential slice of the beam as shown in Figure 2-4. (Fluid resistance to the rotation of the differential slice will be considered subsequently.)

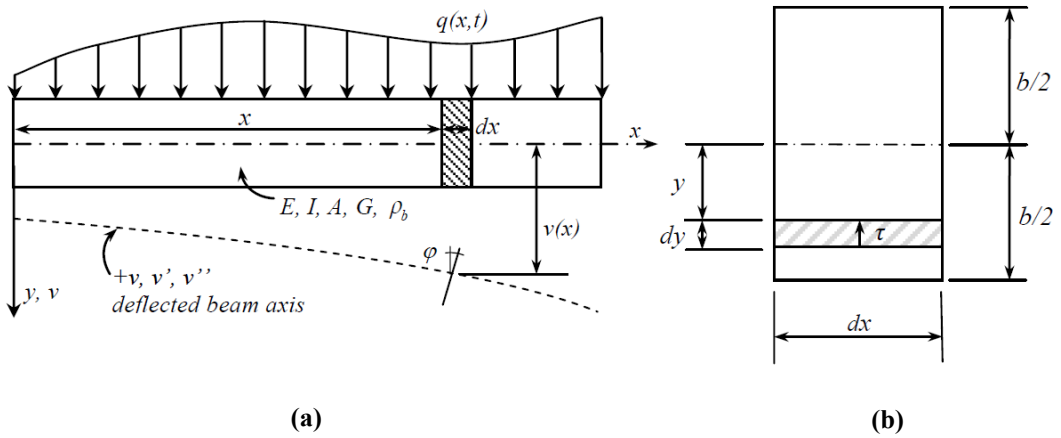

Figure 2-4: Idealized In-Fluid System for Newtonian Method of EOM Derivation: (a) Beam; (b) Differential Beam Element with Fluid Shear Stress Due to Transverse Motion

Fluid forces are obtained and taken into account via the application of Stokes's solution, which is based on the in-plane oscillation of an infinite plate in contact (on one surface) with a semi-infinite viscous fluid [Stokes, 1851]. From Stokes's solution, the shear stress exerted by the fluid on the plate is obtained as

$$\tau(t) = \bar{\bar{m}}_f \frac{d^2 v(t)}{dt^2} + \bar{\bar{c}}_f \frac{dv(t)}{dt}, \tag{2-28}$$

where

$$\bar{\bar{m}}_f = \sqrt{\frac{\rho_f \eta}{2}} \frac{1}{\sqrt{\omega}}, \tag{2-29}$$

$$\bar{\bar{c}}_f = \sqrt{\frac{\rho_f \eta}{2}} \sqrt{\omega}, \tag{2-30}$$

ρ_f is the fluid density, η is the fluid's dynamic viscosity and ω is the frequency of vibration. Equations (2-29) and (2-30) may be interpreted as a distributed effective fluid mass coefficient and a distributed effective fluid resistance coefficient, respectively, each being per unit area of the plate. Since Stokes's solution is based on fluid on only one side of the plate, but in the present

application both of the large surfaces of the beam are in contact with fluid, the shear stress (2-28) must be converted into a distributed force per unit length of beam by integrating over *y* and multiplying by 2. In addition, the *x*-dependence of the beam deflection and, thus, the resisting shear stress provided by the fluid, must be included. The resulting distributed fluid force per unit length of beam (taking downward as positive) is determined as

$$q_{fluid}(x,t) = -2\int_{-b/2}^{b/2} \tau(x,t)\,dy = -\bar{m}_f \frac{\partial^2 v(x,t)}{\partial t^2} - \bar{c}_f \frac{\partial v(x,t)}{\partial t}, \tag{2-31}$$

where

$$\bar{m}_f = \frac{\sqrt{2\rho_f \eta b^2}}{\sqrt{\omega}} \tag{2-32}$$

$$\bar{c}_f = \sqrt{2\rho_f \eta b^2}\sqrt{\omega} \tag{2-33}$$

are, respectively, the effective fluid mass and damping resistance coefficients per unit length of beam.

The fluid resistance to the rotation of the differential beam section will be modeled by applying Stokes's solution "locally," i.e., by assuming that the stress due to rotation φ acts horizontally on the shaded differential area of Fig. 2-5 and is that associated with Stokes's solution. Thus, it will depend on the horizontal velocity and acceleration of the shaded area, which depend on the time-history of φ. Multiplying the force on *dy* by the moment arm y and integrating over *y* enables one to obtain the distributed fluid resisting couple (per unit length of beam), i.e.,

$$C_{fluid}(x,t) = 2\int_{-b/2}^{b/2} y\left[\left(\sqrt{\frac{\rho_f \eta}{2\omega}}\right)\left(y\frac{\partial^2\varphi}{\partial t^2}\right)+\left(\sqrt{\frac{\rho_f \eta\omega}{2}}\right)\left(y\frac{\partial\varphi}{\partial t}\right)\right]dy$$
$$= \frac{\bar{m}_f b^2}{12}\frac{\partial^2\varphi}{\partial t^2}+\frac{\bar{c}_f b^2}{12}\frac{\partial\varphi}{\partial t} \qquad (2\text{-}34)$$

where the sign convention employed for the distributed fluid resisting couple is counterclockwise being positive.

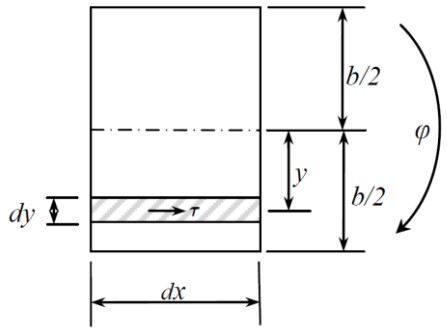

Figure 2-5: Differential Beam Element with Fluid Shear Stress Due to Rotation

Introducing the additional distributed force, Eq. (2-31), and distributed couple, Eq. (2-34), into the force and moment equilibrium analysis of Section 2.3 and noting that, for a beam of rectangular cross section, the mass per unit length $\bar{m}_b = \rho_b bh$ and second moment of area of the cross section $I = \frac{hb^3}{12}$, results in the following coupled, second-order PDEs governing the deformation of a Timoshenko beam of rectangular cross section under the application of a harmonic distributed load in a fluid providing Stokes-type resistance to both transverse deflection and rotation of beam:

$$kAG\left(\frac{\partial^2 v}{\partial x^2}-\frac{\partial\varphi}{\partial x}\right)-\left(\bar{m}_b+\bar{m}_f\right)\frac{\partial^2 v}{\partial t^2}-\bar{c}_f\frac{\partial v}{\partial t} = -Q(x)e^{i\omega t} \qquad (2\text{-}37)$$

$$EI\frac{\partial^2\varphi}{\partial x^2}+kAG\left(\frac{\partial v}{\partial x}-\varphi\right)-\left(\bar{m}_b+\bar{m}_f\right)\frac{I}{A}\frac{\partial^2\varphi}{\partial t^2}-\bar{c}_f\frac{I}{A}\frac{\partial\varphi}{\partial t} = 0\,. \qquad (2\text{-}38)$$

The uncoupled, fourth-order PDEs that describe the in-fluid Timoshenko beam motion in terms of the total displacement, v, and angle of rotation, φ, may be derived from (2-37) and (2-38) in a manner analogous to the approach taken in Sect. 2.3:

$$\begin{aligned} & EI\frac{\partial^4 v}{\partial x^4}-\frac{\left(\overline{m}_b+\overline{m}_f\right)I}{A}\left(1+\frac{E}{kG}\right)\frac{\partial^4 v}{\partial x^2\partial t^2}-\frac{\overline{c}_f I}{A}\left(1+\frac{E}{kG}\right)\frac{\partial^3 v}{\partial x^2\partial t} \\ & +\overline{c}_f\frac{\partial v}{\partial t}+\left[\left(\overline{m}_b+\overline{m}_f\right)+\frac{\overline{c}_f{}^2 I}{kA^2G}\right]\frac{\partial^2 v}{\partial t^2}+\frac{2\overline{c}_f\left(\overline{m}_b+\overline{m}_f\right)I}{kA^2G}\frac{\partial^3 v}{\partial t^3}+\frac{\left(\overline{m}_b+\overline{m}_f\right)^2 I}{kA^2G}\frac{\partial^4 v}{\partial t^4} \\ & =\left\{\left[1-\frac{\omega^2\left(\overline{m}_b+\overline{m}_f\right)I}{kA^2G}+i\frac{\omega\overline{c}_f I}{kA^2G}\right]Q(x)-\frac{EI}{kAG}\frac{d^2Q(x)}{dx^2}\right\}e^{i\omega t} \end{aligned} \tag{2-39}$$

$$\begin{aligned} & EI\frac{\partial^4 \varphi}{\partial x^4}-\frac{\left(\overline{m}_b+\overline{m}_f\right)I}{A}\left(1+\frac{E}{kG}\right)\frac{\partial^4 \varphi}{\partial x^2\partial t^2}-\frac{\overline{c}_f I}{A}\left(1+\frac{E}{kG}\right)\frac{\partial^3 \varphi}{\partial x^2\partial t} \\ & +\overline{c}_f\frac{\partial \varphi}{\partial t}+\left[\left(\overline{m}_b+\overline{m}_f\right)+\frac{\overline{c}_f{}^2 I}{kA^2G}\right]\frac{\partial^2 \varphi}{\partial t^2}+\frac{2\overline{c}_f\left(\overline{m}_b+\overline{m}_f\right)I}{kA^2G}\frac{\partial^3 \varphi}{\partial t^3}+\frac{\left(\overline{m}_b+\overline{m}_f\right)^2 I}{kA^2G}\frac{\partial^4 \varphi}{\partial t^4} \\ & =\frac{dQ(x)}{dx}e^{i\omega t}. \end{aligned} \tag{2-40}$$

From Eqs. (2-37) - (2-40) it is observed that the effects of the fluid can be interpreted as distributed mass and damping resistance parameters. (Compare these generalized equations with their in-vacuum analogs given by Eqs. (2-10) to (2-13).) From the forms of Eqs. (2-37) to (2-40), the $\overline{m}_f$ parameter on the inertial terms can be interpreted as the added mass of the fluid uniformly distributed along the length of the beam. Similarly, the $\overline{c}_f$ parameter can be interpreted as being related to uniformly distributed (translational and rotational) damping coefficients due to the fluid. From a mechanical modeling viewpoint, the fluid effects may be interpreted as shown schematically in Figure 2-6.

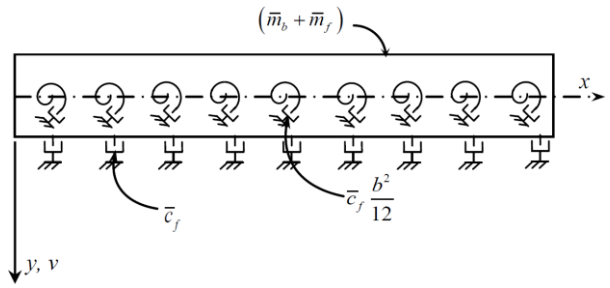

Figure 2-6: Beam Model with Distributed Mass and Fluid Resistance Due the Viscous Fluid Effects Associated with the Stokes Resistance Model

2.4.2 Non-Dimensional Equation of Motion for In-Fluid Case

The non-dimensional forms of (2-37) through (2-40) may be obtained by the introduction of a dimensionless fluid resistance parameter (as was introduced in the Bernoulli-Euler beam model of Heinrich et al., 2010b), defined by

$$\zeta \equiv \frac{L}{hb^{1/2}}\left(\frac{48\rho_f{}^2\eta^2}{E\rho_b{}^3}\right)^{1/4} \tag{2-41}$$

Application of (2-14) - (2-16), (2-19), (2-22) - (2-24), and (2-41) to Eqs. (2-37) and (2-38) results in the dimensionless second-order PDEs:

$$\frac{\partial^2\overline{v}}{\partial\xi^2} - \frac{\partial\varphi}{\partial\xi} - s^2\lambda^3\left(\lambda+\zeta\right)\frac{\partial^2\overline{v}}{\partial\tau^2} - s^2\lambda^3\zeta\frac{\partial\overline{v}}{\partial\tau} = -s^2\bar{Q}(\xi)e^{i\tau} \tag{2-42}$$

$$s^2\frac{\partial^2\varphi}{\partial\xi^2} + \frac{\partial\overline{v}}{\partial\xi} - \varphi - r^2s^2\lambda^3\left(\lambda+\zeta\right)\frac{\partial^2\varphi}{\partial\tau^2} - r^2s^2\lambda^3\zeta\frac{\partial\varphi}{\partial\tau} = 0 \tag{2-43}$$

Similarly, application of (2-14) - (2-16), (2-19), (2-22) - (2-24), and (2-41) to Eqs. (2-39) and (2-40) results in the dimensionless fourth-order PDEs:

$$\begin{aligned}&\frac{\partial^4\overline{v}}{\partial\xi^4}-\lambda^3\left(\lambda+\zeta\right)\left(r^2+s^2\right)\frac{\partial^4\overline{v}}{\partial\xi^2\partial\tau^2}-\lambda^3\zeta\left(r^2+s^2\right)\frac{\partial^3\overline{v}}{\partial\xi^2\partial\tau}+\lambda^3\zeta\frac{\partial\overline{v}}{\partial\tau}\\&+\left[\lambda^3\left(\lambda+\zeta\right)+\lambda^6\zeta^2s^2r^2\right]\frac{\partial^2\overline{v}}{\partial\tau^2}+2r^2s^2\lambda^6\zeta\left(\lambda+\zeta\right)\frac{\partial^3\overline{v}}{\partial\tau^3}\\&+\lambda^6s^2r^2\left(\lambda+\zeta\right)^2\frac{\partial^4\overline{v}}{\partial\tau^4}=\left\{\left[1-\lambda^3r^2s^2\left(\lambda+\zeta-i\zeta\right)\right]\overline{Q}(\xi)-s^2\frac{\partial^2\overline{Q}(\xi)}{\partial\xi^2}\right\}e^{i\tau}\end{aligned}\tag{2-44}$$

$$\begin{aligned}&\frac{\partial^4\varphi}{\partial\xi^4}-\lambda^3\left(\lambda+\zeta\right)\left(r^2+s^2\right)\frac{\partial^4\varphi}{\partial\xi^2\partial\tau^2}-\lambda^3\zeta\left(r^2+s^2\right)\frac{\partial^3\varphi}{\partial\xi^2\partial\tau}+\lambda^3\zeta\frac{\partial\varphi}{\partial\tau}\\&+\left[\lambda^3\left(\lambda+\zeta\right)+\lambda^6\zeta^2s^2r^2\right]\frac{\partial^2\varphi}{\partial\tau^2}+2r^2s^2\lambda^6\zeta\left(\lambda+\zeta\right)\frac{\partial^3\varphi}{\partial\tau^3}\\&+\lambda^6s^2r^2\left(\lambda+\zeta\right)^2\frac{\partial^4\varphi}{\partial\tau^4}=\frac{\partial\overline{Q}(\xi)}{\partial\xi}e^{i\tau}\end{aligned}\tag{2-45}$$

2.5 Reduction of EOMs to Known Cases

As a means of verification, the Timoshenko beam EOMs for the in-fluid case may be reduced to other known cases.

Special Case 1: Timoshenko Beam in Vacuum:

In the general second-order EOMs for a Timoshenko beam with Stokes fluid resistance [Eqs. (2-42) and (2-43)], if the fluid resistance parameter, ζ, is set equal to zero, the results clearly become the second-order EOMs for a Timoshenko beam in vacuum [Eqs. (2-20) and (2-21)]. A similar conclusion may be confirmed by examining the corresponding fourth-order EOMs, i.e., Eqs. (2-44) and (2-45) reduce to (2-26) and (2-27). Note that, in addition if one sets the applied load $\bar{Q}(\xi)$ equal to zero, the equations become consistent with those presented by Huang [1961] for the free vibration of a Timoshenko beam in vacuum.

Special Case 2: Bernoulli-Euler Beam with Stokes Fluid Resistance:

By zeroing out the Timoshenko parameters (*r* and *s*) in the fourth-order EOM given by Eq. (2-44) for in-fluid vibrations and considering the case of no applied external distributed load

($\bar{Q}(\xi) = 0$), that equation reduces to that presented by Heinrich et al. [2010b] for a Bernoulli-Euler beam experiencing Stokes fluid resistance:

$$\frac{\partial^4 \overline{v}}{\partial \xi^4} + \lambda^3 \left(\lambda + \zeta\right) \frac{\partial^2 \overline{v}}{\partial \tau^2} + \lambda^3 \zeta \frac{\partial \overline{v}}{\partial \tau} = 0 \quad . \tag{2-46}$$

Special Case 3: Bernoulli-Euler Beam in Vacuum:

Simultaneously setting the fluid resistance parameter and the Timoshenko beam parameters to zero in the fourth-order EOM [Eq. (2-44)] yields the EOM for the well-known case of a harmonically loaded Bernoulli-Euler beam in vacuum:

$$\frac{\partial^4 \overline{v}}{\partial \xi^4} + \lambda^4 \frac{\partial^2 \overline{v}}{\partial \tau^2} = \bar{Q}(\xi) e^{i\tau} . \tag{2-47}$$

2.6 Boundary Conditions

The complete formulations of the governing BVPs for the problems of interest require the specification of appropriate boundary conditions (BCs). Whether the EOMs are the uncoupled fourth-order equations or the coupled second-order equations, a total of four BCs will be required. Consequently, two BCs must be specified at each end of the beam in order to correspond to the physical conditions that are present at those locations. Problems of interest in the present study include free vibration and two cases of forced excitation (harmonic point load at the tip and harmonic support rotation). As a consequence, a total of six separate boundary conditions will be presented in what follows.

2.6.1 Relevant Boundary Conditions at Supported End

For the problems of interest herein, there exist a total of three relevant boundary conditions at the supported end (x = 0):

$$v(0,t) = 0 , \tag{2-48a}$$

$$\varphi(0,t) = 0\,, \tag{2-48b}$$

$$\varphi(0,t) = \theta(t) \equiv \theta_0 e^{i\omega t} \tag{2-48c}$$

where Eqs. (2-48a) and (2-48b) correspond, respectively, to the total displacement and the rotation angle being equal to zero (i.e., a perfectly clamped beam), while Equation (2-48c) describes an imposed harmonic support rotation. The latter BC was inspired by the electrothermal excitation method employed by colleagues at Georgia Tech [Beardslee et al., 2010a-d; Beardslee et al., 2011a], and is a Timoshenko-beam analog of the BC introduced in the Bernoulli-Euler beam model of Heinrich et al. [2010b] to model this type of loading. Note that this type of excitation imposes axial strains at the extreme fibers of the cross section (bending-type deformation) and results in little, if any, shear deformation. Thus, Eq. (2-48c) involves the rotation angle, i.e., the slope of the bending deflection, instead of the slope of the total deflection.

The dimensionless forms of (2-48a-c) corresponding to location $\xi = 0$ may easily be shown to be

$$\bar{v}(0,\tau) = 0\,, \tag{2-49a}$$

$$\varphi(0,\tau) = 0\,, \tag{2-49b}$$

$$\varphi(0,\tau) = \theta_0 e^{i\tau}\,. \tag{2-49c}$$

2.6.2 Boundary Conditions at Tip

The relevant boundary conditions at the tip (x = L) of the cantilever beam are (see, e.g., Huang, 1961)

$$\frac{\partial \varphi(L,t)}{\partial x} = 0 \tag{2-50a}$$

$$\frac{\partial v(L,t)}{\partial x} - \varphi\left(L,t\right) = 0 \tag{2-50b}$$

$$kAG\left[\frac{\partial v(L,t)}{\partial x}-\varphi\left(L,t\right)\right]=F_0e^{i\omega t} \tag{2-50c}$$

where (2-50a) and (2-50b) correspond to zero bending moment and zero shear force at the tip, respectively; thus, this pair of BCs would apply to the case of an unloaded tip. When the case of a harmonic shear force applied at the tip is considered (another common case in resonant microcantilever-based sensors excited, say, by electromagnetic means), then Eq. (2-50c) would apply in place of (2-50b).

The dimensionless forms of (2-50a-c) corresponding to location $\xi=1$ may easily be shown to be

$$\frac{\partial\varphi(1,\tau)}{\partial\xi}=0 \tag{2-51a}$$

$$\frac{\partial\overline{v}(1,\tau)}{\partial\xi}-\varphi\left(1,\tau\right)=0 \tag{2-51b}$$

$$\frac{\partial\overline{v}(1,\tau)}{\partial\xi}-\varphi\left(1,\tau\right)=s^2\overline{F}_0e^{i\tau} \tag{2-51c}$$

where

$$\overline{F}_0\equiv\frac{F_0L^2}{EI} \tag{2-52}$$

represents the dimensionless tip load amplitude.

2.7 Summary of Timoshenko Beam BVPs

The three load cases to be considered for the remainder of this investigation are free vibration, harmonic tip load and harmonic support rotation. The BVPs for these scenarios are summarized in this section utilizing the previously derived fourth-order EOMs and appropriate BCs.

2.7.1 Free Vibration BVP

The dimensionless fourth-order form of the BVP for the case of in-fluid, free vibration of a Timoshenko beam for $\bar{v}$ and φ is given below.

Free Vibration in Fluid:

$$\begin{aligned}&\frac{\partial^4\bar{v}}{\partial\xi^4}-\lambda^3\left(\lambda+\zeta\right)\left(r^2+s^2\right)\frac{\partial^4\bar{v}}{\partial\xi^2\partial\tau^2}-\lambda^3\zeta\left(r^2+s^2\right)\frac{\partial^3\bar{v}}{\partial\xi^2\partial\tau}+\lambda^3\zeta\frac{\partial\bar{v}}{\partial\tau}\\&+\left[\lambda^3\left(\lambda+\zeta\right)+\lambda^6\zeta^2s^2r^2\right]\frac{\partial^2\bar{v}}{\partial\tau^2}+2r^2s^2\lambda^6\zeta\left(\lambda+\zeta\right)\frac{\partial^3\bar{v}}{\partial\tau^3}\\&+\lambda^6s^2r^2\left(\lambda+\zeta\right)^2\frac{\partial^4\bar{v}}{\partial\tau^4}=0\end{aligned}\tag{2-53}$$

$$\begin{aligned}&\frac{\partial^4\varphi}{\partial\xi^4}-\lambda^3\left(r^2+s^2\right)\left(\lambda+\zeta\right)\frac{\partial^4\varphi}{\partial\xi^2\partial\tau^2}-\lambda^3\zeta\left(r^2+s^2\right)\frac{\partial^3\varphi}{\partial\xi^2\partial\tau}+\lambda^3\zeta\frac{\partial\varphi}{\partial\tau}\\&+\left[\lambda^3\left(\lambda+\zeta\right)+\lambda^6\zeta^2s^2r^2\right]\frac{\partial^2\varphi}{\partial\tau^2}+2r^2s^2\lambda^6\zeta\left(\lambda+\zeta\right)\frac{\partial^3\varphi}{\partial\tau^3}\\&+\lambda^6s^2r^2\left(\lambda+\zeta\right)^2\frac{\partial^4\varphi}{\partial\tau^4}=0\end{aligned}\tag{2-54}$$

$$\bar{v}(0,\tau)=\varphi(0,\tau)=\frac{\partial\varphi(1,\tau)}{\partial\xi}=\frac{\partial\bar{v}(1,\tau)}{\partial\xi}-\varphi\left(1,\tau\right)=0\quad .\tag{2-55a-d}$$

Note that the above BVP governing the free-vibration response corresponds to an eigenvalue problem in that the unknowns to be determined include not only the functions $\bar{v}$ and φ (whose spatially dependent portions are the eigenfunctions), but also the corresponding values of the unknown parameter λ (eigenvalues). It is further noted that, although the solution of the in-fluid BVP above has been deemed outside of the scope of the present study, the mathematical form is listed here for reference purposes and the in-vacuum BVP can be obtained by setting the fluid parameter, ζ, to zero. The solution to the latter case was presented by Huang [1961] and will be reviewed in Sect. 3.2.

2.7.2 Forced Vibration BVP: Harmonic Tip Load

The dimensionless fourth-order form of the BVP for the case of in-fluid, forced vibration (via harmonic tip load) of a Timoshenko beam takes the following form:

Forced Vibration in Fluid via Harmonic Tip Load:

$$\begin{aligned}&\frac{\partial^4\overline{v}}{\partial\xi^4}-\lambda^3\left(\lambda+\zeta\right)\left(r^2+s^2\right)\frac{\partial^4\overline{v}}{\partial\xi^2\partial\tau^2}-\lambda^3\zeta\left(r^2+s^2\right)\frac{\partial^3\overline{v}}{\partial\xi^2\partial\tau}+\lambda^3\zeta\frac{\partial\overline{v}}{\partial\tau}\\&+\left[\lambda^3\left(\lambda+\zeta\right)+\lambda^6\zeta^2s^2r^2\right]\frac{\partial^2\overline{v}}{\partial\tau^2}+2r^2s^2\lambda^6\zeta\left(\lambda+\zeta\right)\frac{\partial^3\overline{v}}{\partial\tau^3}\\&+\lambda^6s^2r^2\left(\lambda+\zeta\right)^2\frac{\partial^4\overline{v}}{\partial\tau^4}=0\end{aligned}\tag{2-56}$$

$$\begin{aligned}&\frac{\partial^4\varphi}{\partial\xi^4}-\lambda^3\left(r^2+s^2\right)\left(\lambda+\zeta\right)\frac{\partial^4\varphi}{\partial\xi^2\partial\tau^2}-\lambda^3\zeta\left(r^2+s^2\right)\frac{\partial^3\varphi}{\partial\xi^2\partial\tau}+\lambda^3\zeta\frac{\partial\varphi}{\partial\tau}\\&+\left[\lambda^3\left(\lambda+\zeta\right)+\lambda^6\zeta^2s^2r^2\right]\frac{\partial^2\varphi}{\partial\tau^2}+2r^2s^2\lambda^6\zeta\left(\lambda+\zeta\right)\frac{\partial^3\varphi}{\partial\tau^3}\\&+\lambda^6s^2r^2\left(\lambda+\zeta\right)^2\frac{\partial^4\varphi}{\partial\tau^4}=0\end{aligned}\tag{2-57}$$

$$\overline{v}(0,\tau)=\varphi(0,\tau)=\frac{\partial\varphi(1,\tau)}{\partial\xi}=0\,,\quad\frac{\partial\overline{v}(1,\tau)}{\partial\xi}-\varphi\left(1,\tau\right)=s^2\overline{F}_0e^{i\tau}\tag{2-58a-d}$$

Note that the corresponding in-vacuum BVP can be obtained by setting ζ=0.

2.7.3 Forced Vibration BVP: Harmonic Support Rotation

The dimensionless fourth-order form of the BVP for the case of in-fluid, forced vibration of a Timoshenko beam via harmonic support rotation is the following. (The corresponding in-vacuum BVP can be obtained by zeroing out the fluid parameter, ζ .)

Forced Vibration in Fluid via Harmonic Support Rotation:

$$\begin{aligned}&\frac{\partial^4\overline{v}}{\partial\xi^4}-\lambda^3\left(\lambda+\zeta\right)\left(r^2+s^2\right)\frac{\partial^4\overline{v}}{\partial\xi^2\partial\tau^2}-\lambda^3\zeta\left(r^2+s^2\right)\frac{\partial^3\overline{v}}{\partial\xi^2\partial\tau}+\lambda^3\zeta\frac{\partial\overline{v}}{\partial\tau}\\&+\left[\lambda^3\left(\lambda+\zeta\right)+\lambda^6\zeta^2s^2r^2\right]\frac{\partial^2\overline{v}}{\partial\tau^2}+2r^2s^2\lambda^6\zeta\left(\lambda+\zeta\right)\frac{\partial^3\overline{v}}{\partial\tau^3}\\&+\lambda^6s^2r^2\left(\lambda+\zeta\right)^2\frac{\partial^4\overline{v}}{\partial\tau^4}=0\end{aligned}\tag{2-59}$$

$$\frac{\partial^4\varphi}{\partial\xi^4}-\lambda^3\left(r^2+s^2\right)\left(\lambda+\zeta\right)\frac{\partial^4\varphi}{\partial\xi^2\partial\tau^2}-\lambda^3\zeta\left(r^2+s^2\right)\frac{\partial^3\varphi}{\partial\xi^2\partial\tau}+\lambda^3\zeta\frac{\partial\varphi}{\partial\tau}$$
$$+\left[\lambda^3\left(\lambda+\zeta\right)+\lambda^6\zeta^2s^2r^2\right]\frac{\partial^2\varphi}{\partial\tau^2}+2r^2s^2\lambda^6\zeta\left(\lambda+\zeta\right)\frac{\partial^3\varphi}{\partial\tau^3} \tag{2-60}$$
$$+\lambda^6s^2r^2\left(\lambda+\zeta\right)^2\frac{\partial^4\varphi}{\partial\tau^4}=0$$

$$\bar{v}(0,\tau)=\frac{\partial\varphi(1,\tau)}{\partial\xi}=\frac{\partial\bar{v}(1,\tau)}{\partial\xi}-\varphi\left(1,\tau\right)=0\,,\ \ \varphi(0,\tau)=\theta_0e^{i\tau} \tag{2-61a-d}$$

2.8 Derivation of Secondary Response Fields

Since the beam response is completely described using the "primary fields," $\bar{v}$ and φ, any additional ("secondary") fields should be derivable directly from $\bar{v}$ and φ. Note that the new dimensionless fields are defined in an analogous manner as $\bar{v}(\xi,\tau)$ in Eq. (2-16). The time-dependent beam displacement due to bending is obtained by recalling the definition of the bending displacement in Eq. (2-4) which results in

$$\bar{v}_B(\xi,\tau)=\int_0^{\xi}\varphi(\xi,\tau)d\xi+\bar{v}_B(0,\tau)=\int_0^{\xi}\varphi(\xi,\tau)d\xi\,, \tag{2-62}$$

where $\bar{v}_B(0,\tau)$ has been set equal to zero to account for the BC for the cantilevers considered in this study. The dimensionless bending displacement $\bar{v}_B$ is defined in a manner analogous to the definition of $\bar{v}$ in Eq. (2-16), i.e., $\bar{v}_B\equiv v_B/L$.

Similarly, the time-dependent beam response associated with shear displacement only is obtained by using the dimensionless analogue of Eq. (2-3) and Eq. (2-62). This yields

$$\bar{v}_S(\xi,\tau)\equiv\frac{v_S(\xi,\tau)}{L}=\bar{v}(\xi,\tau)-\int_0^{\xi}\varphi(\xi,\tau)d\xi\,. \tag{2-63}$$

Finally, the shear strain, $\psi(\xi,\tau)$, defined in Eq. (2-4), can be derived by taking the derivative of Eq. (2-63) with respect to ξ:

$$\psi(\xi,\tau)=\frac{\partial\bar{v}_S(\xi,\tau)}{\partial\xi}=\frac{\partial\bar{v}(\xi,\tau)}{\partial\xi}-\varphi(\xi,\tau)\,. \tag{2-64}$$

CHAPTER 3: METHOD OF SOLUTION OF BOUNDARY VALUE PROBLEM

3.1 Introductory Remarks

Chapter 3 begins with the presentation of the solution to the eigenvalue problem for the in-vacuum, free vibration of a Timoshenko beam. The solution for this case is presented initially since the subsequent problems are further generalizations and will be verified in part against the in-vacuum, free vibration results. Following the in-vacuum, free vibration solution, the solutions for the forced vibration (via harmonic tip load and harmonic support rotation) BVPs for in-fluid cases are presented, the in-vacuum results being included as special cases.

3.2 Free Vibration in Vacuum

The solution of the free vibration of a Timoshenko beam was presented in detail by Huang [1961] and is summarized here since this solution will serve as a point of reduction and comparison for the scenarios of forced vibration and in-fluid operation. The solution of the eigen-problem consists of deriving the frequency equation, obtaining the natural frequencies from the roots of the frequency equation, and determining the concomitant mode shapes for each associated natural frequency.

By setting $\bar{Q}=0$ in the general results of Sect. 2.3.2, the second- and fourth-order PDEs for in-vacuum, free-vibration of a Timoshenko beam are

$$\frac{\partial^2 \bar{v}}{\partial \xi^2} - \lambda^4 s^2 \frac{\partial^2 \bar{v}}{\partial \tau^2} - \frac{\partial \varphi}{\partial \xi} = 0\,, \tag{3-1}$$

$$s^2 \frac{\partial^2 \varphi}{\partial \xi^2} - \lambda^4 r^2 s^2 \frac{\partial^2 \varphi}{\partial \tau^2} - \varphi + \frac{\partial \bar{v}}{\partial \xi} = 0\,, \tag{3-2}$$

$$\frac{\partial^4 \bar{v}}{\partial \xi^4} + \lambda^4 \frac{\partial^2 \bar{v}}{\partial \tau^2} - \lambda^4 \left(r^2 + s^2\right) \frac{\partial^4 \bar{v}}{\partial \xi^2 \partial \tau^2} + \lambda^8 r^2 s^2 \frac{\partial^4 \bar{v}}{\partial \tau^4} = 0\,, \tag{3-3}$$

$$\frac{\partial^4 \varphi}{\partial \xi^4} + \lambda^4 \frac{\partial^2 \varphi}{\partial \tau^2} - \lambda^4 \left(r^2 + s^2\right) \frac{\partial^4 \varphi}{\partial \xi^2 \partial \tau^2} + \lambda^8 r^2 s^2 \frac{\partial^4 \varphi}{\partial \tau^4} = 0\,. \tag{3-4}$$

The concomitant BCs for free-vibration of a cantilever beam are listed in Eqs. (2-55a-d) and are restated here for convenience:

$$\bar{v}(0,\tau)=0\,, \tag{3-5a}$$

$$\varphi(0,\tau)=0\,, \tag{3-5b}$$

$$\frac{\partial\varphi(1,\tau)}{\partial\xi}=0\,, \tag{3-5c}$$

$$\frac{\partial\bar{v}(1,\tau)}{\partial\xi}-\varphi(1,\tau)=0\,. \tag{3-5d}$$

Solutions to Eqs. (3-1) through (3-5a-d) are sought in the following separable forms:

$$\bar{v}=\bar{V}(\xi)e^{i\tau} \tag{3-6}$$

$$\varphi=\Phi(\xi)e^{i\tau}\,. \tag{3-7}$$

Application of (3-6) and (3-7) to (3-1) through (3-5a-d) results in second- and fourth-order ODEs and associated BCs, where $(\,)'$ indicates a spatial derivative with respect to ξ and $(\dot{})$ indicates a time derivative with respect to τ:

$$\bar{V}''+\lambda^4 s^2\bar{V}-\Phi'=0\,, \tag{3-8}$$

$$s^2\Phi''-\left(1-\lambda^4 r^2 s^2\right)\Phi+\bar{V}'=0\,, \tag{3-9}$$

$$\bar{V}''''+\lambda^4\left(r^2+s^2\right)\bar{V}''-\lambda^4\left(1-\lambda^4 r^2 s^2\right)\bar{V}=0\,, \tag{3-10}$$

$$\Phi''''+\lambda^4\left(r^2+s^2\right)\Phi''-\lambda^4\left(1-\lambda^4 r^2 s^2\right)\Phi=0\,, \tag{3-11}$$

$$\bar{V}(0)=0\,, \tag{3-12a}$$

$$\Phi(0)=0\,, \tag{3-12b}$$

$$\Phi'(1)=0\,, \tag{3-12c}$$

$$\bar{V}'(1)-\Phi(1)=0\,. \tag{3-12d}$$

Note that in Eqs. (3-8) to (3-11) the only unknown parameter (for a given beam geometry and beam material) is the normalized frequency of vibration, λ.

Huang derived and presented the solutions to (3-10) and (3-11) by considering two separate cases in order to minimize the need for complex algebra. In the first case, corresponding to when $\lambda^4 < \frac{1}{r^2 s^2}$, the general solution of Eqs. (3-10) and (3-11) take the forms

$$\bar{V} = C_1 \cosh\left(\lambda^2 \alpha \xi\right) + C_2 \sinh\left(\lambda^2 \alpha \xi\right) + C_3 \cos\left(\lambda^2 \beta \xi\right) + C_4 \sin\left(\lambda^2 \beta \xi\right) \tag{3-13a}$$

$$\Phi = C_1' \sinh\left(\lambda^2 \alpha \xi\right) + C_2' \cosh\left(\lambda^2 \alpha \xi\right) + C_3' \sin\left(\lambda^2 \beta \xi\right) + C_4' \cos\left(\lambda^2 \beta \xi\right) \tag{3-13b}$$

where α and β are

$$\begin{matrix} \alpha \\ \beta \end{matrix} = \frac{1}{\sqrt{2}} \left\{ \mp \left(r^2 + s^2 \right) + \left[\left(r^2 - s^2 \right)^2 + \frac{4}{\lambda^4} \right]^{1/2} \right\}^{1/2} . \tag{3-14}$$

The notation in Eq. (3-14) implies that the upper sign is associated with the upper quantity (α in this case), etc.

In the second case, $\lambda^4 > \frac{1}{r^2 s^2}$, the general solution may be written as

$$\bar{V} = C_1 \cos\left(\lambda^2 \alpha' \xi\right) + iC_2 \sin\left(\lambda^2 \alpha' \xi\right) + C_3 \cos\left(\lambda^2 \beta \xi\right) + C_4 \sin\left(\lambda^2 \beta \xi\right) \tag{3-15a}$$

$$\Phi = iC_1' \sin\left(\lambda^2 \alpha' \xi\right) + C_2' \cos\left(\lambda^2 \alpha' \xi\right) + C_3' \sin\left(\lambda^2 \beta \xi\right) + C_4' \cos\left(\lambda^2 \beta \xi\right) \tag{3-15b}$$

where α' is now defined as follows

$$\alpha' = \frac{1}{\sqrt{2}} \left\{ \left(r^2 + s^2 \right) - \left[\left(r^2 - s^2 \right)^2 + \frac{4}{\lambda^4} \right]^{1/2} \right\}^{1/2} . \tag{3-16}$$

The coefficients C and C' in (3-13a-b) and (3-15a-b) are not independent, as they are related by the following equations which may be derived from either Eq. (3-8) or Eq. (3-9):

$$C_1 = \frac{L}{\lambda^2 \alpha} \left[1 - \lambda^4 s^2 \left(\alpha^2 + r^2 \right) \right] C_1' , \tag{3-17a}$$

$$C_2 = \frac{L}{\lambda^2 \alpha} \left[1 - \lambda^4 s^2 \left(\alpha^2 + r^2 \right) \right] C_2' , \tag{3-17b}$$

$$C_3 = -\frac{L}{\lambda^2\beta}\left[1+\lambda^4 s^2\left(\beta^2 - r^2\right)\right]C_3', \tag{3-17c}$$

$$C_4 = \frac{L}{\lambda^2\beta}\left[1+\lambda^4 s^2\left(\beta^2 - r^2\right)\right]C_4'. \tag{3-17d}$$

Application of the BCs (3-12a-d) and the coefficient relationships (3-17a-d) to either Eqs. (3-13a-b) for Case 1 or (3-15a-b) for Case 2 results in a system of four equations in terms of the four coefficients, C_i. For the solution of the resulting algebraic eigenvalue problem, the frequency equation is obtained by setting the coefficient matrix equal to zero and solving for the natural frequencies. Then, for each natural frequency the corresponding mode shape (i.e., the pair of functions, $\bar{V}(\xi)$ and $\Phi(\xi)$) for the free vibration of a Timoshenko cantilever in vacuum are determined to be the following:

Case 1: $\lambda^4 < \dfrac{1}{r^2 s^2}$

The frequency equation is

$$2+\left[\lambda^4\left(r^2-s^2\right)^2+2\right]\cosh\left(\lambda^2\alpha\right)\cos\left(\lambda^2\beta\right)-\frac{\lambda^2\left(r^2+s^2\right)}{\left(1-\lambda^4 r^2 s^2\right)^{1/2}}\sinh\left(\lambda^2\alpha\right)\sin\left(\lambda^2\beta\right)=0 \tag{3-18}$$

whose roots, λ_i, are the normalized natural frequencies. The corresponding mode shapes are

$$\bar{V} = D\left[\cosh\left(\lambda^2\alpha\xi\right)-\varepsilon\chi\delta\sinh\left(\lambda^2\alpha\xi\right)-\cos\left(\lambda^2\beta\xi\right)+\delta\sin\left(\lambda^2\beta\xi\right)\right], \tag{3-19a}$$

$$\Phi = H\left[\cosh\left(\lambda^2\alpha\xi\right)+\frac{\mu}{\varepsilon\chi}\sinh\left(\lambda^2\alpha\xi\right)-\cos\left(\lambda^2\beta\xi\right)+\mu\sin\left(\lambda^2\beta\xi\right)\right], \tag{3-19b}$$

where $\lambda=\lambda_i$, i=1, 2, ..., (the subscript "i" being suppressed for convenience) and

$$\varepsilon = \alpha/\beta, \tag{3-20}$$

$$\begin{aligned}\chi &= (\alpha^2+r^2)/(\alpha^2+s^2) = (\beta^2-s^2)/(\beta^2-r^2)\\ &= (\alpha^2+r^2)/(\beta^2-r^2) = (\beta^2-s^2)/(\alpha^2+s^2)\end{aligned}, \tag{3-21}$$

$$\delta = \frac{\frac{1}{\varepsilon}\sinh\left(\lambda^2\alpha\right)-\sin\left(\lambda^2\beta\right)}{\chi\cosh\left(\lambda^2\alpha\right)+\cos\left(\lambda^2\beta\right)}, \tag{3-22}$$

$$\mu = -\frac{\varepsilon \sinh\left(\lambda^2\alpha\right) + \sin\left(\lambda^2\beta\right)}{\frac{1}{\chi}\cosh\left(\lambda^2\alpha\right) + \cos\left(\lambda^2\beta\right)}. \tag{3-23}$$

The coefficients, *D* and *H*, are related through any of (3-17a-d), which results in

$$H = \frac{\varepsilon\chi}{\mu}\frac{\lambda^2}{L}\frac{\alpha^2 + s^2}{\alpha} D, \tag{3-24}$$

which may be shown by equating coefficients of (3-19b) and (3-13b) and employing (3-17a-d). Either the constant *D* or *H* can be chosen to be an arbitrary value due to the fact that an eigenfunction (mode shape) has an arbitrary magnitude.

Case 2: $\lambda^4 > \frac{1}{r^2 s^2}$

The frequency equation is obtained similarly as

$$2 + \left[\lambda^4\left(r^2 - s^2\right)^2 + 2\right]\cos\left(\lambda^2\alpha'\right)\cos\left(\lambda^2\beta\right) - \frac{\lambda^2\left(r^2 + s^2\right)}{\left(\lambda^4 r^2 s^2 - 1\right)^{1/2}}\sin\left(\lambda^2\alpha'\right)\sin\left(\lambda^2\beta\right) = 0 \tag{3-25}$$

whose roots, λ_i, are the normalized natural frequencies. The corresponding mode shapes are:

$$\bar{V} = D\left[\cos\left(\lambda^2\alpha'\xi\right) + \varepsilon'\chi\bar{\delta}\sin\left(\lambda^2\alpha'\xi\right) - \cos\left(\lambda^2\beta\xi\right) + \bar{\delta}\sin\left(\lambda^2\beta\xi\right)\right], \tag{3-26a}$$

$$\Phi = H\left[\cos\left(\lambda^2\alpha'\xi\right) - \frac{\bar{\mu}}{\varepsilon'\chi}\sin\left(\lambda^2\alpha'\xi\right) - \cos\left(\lambda^2\beta\xi\right) + \bar{\mu}\sin\left(\lambda^2\beta\xi\right)\right], \tag{3-26b}$$

where $\lambda = \lambda_i$, i=1, 2, ..., and

$$\bar{\delta} = \frac{\frac{1}{\varepsilon'}\sinh\left(\lambda^2\alpha'\right) - \sin\left(\lambda^2\beta\right)}{\chi\cosh\left(\lambda^2\alpha'\right) + \cos\left(\lambda^2\beta\right)}, \tag{3-27}$$

$$\bar{\mu} = \frac{\varepsilon'\sinh\left(\lambda^2\alpha'\right) - \sin\left(\lambda^2\beta\right)}{\frac{1}{\chi}\cosh\left(\lambda^2\alpha'\right) + \cos\left(\lambda^2\beta\right)}, \tag{3-28}$$

$$\varepsilon' = a'/\beta. \tag{3-29}$$

The coefficients, *D* and *H*, are related through any of (3-17a-d), which results in

$$H = \frac{\varepsilon' \chi}{\bar{\mu}} \frac{\lambda^2}{L} \frac{\alpha^2 + s^2}{\alpha} D \,. \tag{3-30}$$

Equation (3-30) is obtained by equating coefficients of (3-26b) and (3-13b). Again, the constant, *D,* is arbitrary due to the fact that an eigenfunction (mode shape) has an arbitrary magnitude.

3.3 Forced Vibration in Fluid – Harmonic Tip Load

In this section the solution of the in-fluid, forced vibration of a Timoshenko beam is presented in detail for the case of a harmonic tip force loading, with the in-vacuum analog being simply a special case ($\zeta = 0$) of the in-fluid case. The solution of this BVP consists of deriving the beam response as described by $\bar{v}(\xi, \tau)$ and $\varphi(\xi, \tau)$. From these displacement and rotation fields, subsequent information regarding resonant frequencies is obtained from frequency response plots, i.e., plots of tip displacement vs. exciting frequency. The corresponding quality factor results are then calculated from the frequency response plots using the 3-dB bandwidth method.

A solution to the fourth-order BVP for a laterally vibrating Timoshenko cantilever beam under the action of a harmonic tip force, including the effects of Stokes fluid resistance, will now be pursued. This BVP was summarized in Sect. 2.7.2 and is given explicitly by Eqs. (2-56), (2-57), and (2-58a-d). Assume $\bar{v}(\xi, \tau)$ and $\varphi(\xi, \tau)$ are separable and of the following forms:

$$\bar{v}(\xi, \tau) = \bar{V}(\xi) e^{i\tau}, \tag{3-31}$$

$$\varphi(\xi, \tau) = \Phi(\xi) e^{i\tau} \,. \tag{3-32}$$

Application of (3-31) and (3-32) to (2-56) through (2-58a-d) results in two fourth-order ODEs and associated BCs in terms of the spatially dependent functions $\bar{V}(\xi)$ and $\Phi(\xi)$:

$$\begin{aligned} &\bar{V}'''' + \lambda^3 \left(r^2 + s^2\right)\left[\lambda + (1-i)\zeta\right]\bar{V}'' \\ &-\lambda^3 \left[\lambda + (1-i)\zeta\right]\left\{1 - r^2 s^2 \lambda^3 \left[\lambda + (1-i)\zeta\right]\right\}\bar{V} = 0, \end{aligned} \tag{3-33}$$

$$\begin{aligned}&\Phi'''' + \lambda^3\left(r^2+s^2\right)\left[\lambda+(1-i)\zeta\right]\Phi'' \\ &-\lambda^3\left[\lambda+(1-i)\zeta\right]\left\{1-r^2s^2\lambda^3\left[\lambda+(1-i)\zeta\right]\right\}\Phi = 0,\end{aligned} \tag{3-34}$$

$$\bar{V}(0) = 0\,, \tag{3-35a}$$

$$\Phi(0) = 0\,, \tag{3-35b}$$

$$\Phi'(1) = 0\,, \tag{3-35c}$$

$$\frac{\bar{V}'(1)-\Phi(1)}{s^2} = \bar{F}_0\ , \tag{3-35d}$$

where ( )′ indicates a spatial derivative with respect to ξ. For convenience (3-33) and (3-34) are rewritten as

$$\bar{V}'''' + k_1\bar{V}'' + k_2\bar{V} = 0\,, \tag{3-36}$$

$$\Phi'''' + k_1\Phi'' + k_2\Phi = 0\,, \tag{3-37}$$

where

$$k_1 = k_1(\lambda) = \lambda^3\left(r^2+s^2\right)\left[\lambda+(1-i)\zeta\right], \tag{3-38}$$

$$k_2 = k_2(\lambda) = -\lambda^3\left[\lambda+(1-i)\zeta\right]\left\{1-r^2s^2\lambda^3\left[\lambda+(1-i)\zeta\right]\right\}. \tag{3-39}$$

By assuming a general solution form of Eq. (3-36) as

$$\bar{V}(\xi) = Ce^{n\xi}, \tag{3-40}$$

the characteristic equation for *n* becomes

$$n^4 + k_1n^2 + k_2 = 0\,, \tag{3-41}$$

whose roots are obtained as

$$n_1 = +\left[\left(\tfrac{1}{2}\right)\left(-k_1+\sqrt{k_1^{\,2}-4k_2}\right)\right]^{\frac{1}{2}}\ , \tag{3-42a}$$

$$n_2 = -\left[\left(\tfrac{1}{2}\right)\left(-k_1+\sqrt{k_1^{\,2}-4k_2}\right)\right]^{\frac{1}{2}}, \tag{3-42b}$$

$$n_3 = +\left[\left(\tfrac{1}{2}\right)\left(-k_1-\sqrt{k_1^{\,2}-4k_2}\right)\right]^{\frac{1}{2}}, \tag{3-42c}$$

$$n_4 = -\left[\left(\tfrac{1}{2}\right)\left(-k_1 - \sqrt{k_1^{\,2} - 4k_2}\right)\right]^{\frac{1}{2}}. \tag{3-42d}$$

Note that these roots are frequency-dependent, i.e., $n_i = n_i(\lambda)$, and satisfy the relationships $n_2(\lambda) = -n_1(\lambda)$ and $n_4(\lambda) = -n_3(\lambda)$. For definiteness, roots $n_1(\lambda)$ and $n_3(\lambda)$ are defined as the two roots having positive real values. With these relationships, the solution may be written in trigonometric/hyperbolic form as

$$\bar{V} = C_1 \cosh\left(n_1\xi\right) + C_2 \sinh\left(n_1\xi\right) + C_3 \cos\left(in_3\xi\right) + C_4 \sin\left(in_3\xi\right). \tag{3-43}$$

The general solution for $\Phi(\xi)$ may be obtained similarly as

$$\Phi = C_1' \cosh\left(n_1\xi\right) + C_2' \sinh\left(n_1\xi\right) + C_3' \cos\left(in_3\xi\right) + C_4' \sin\left(in_3\xi\right). \tag{3-44}$$

Analogous to the approach taken by Huang [1961], the relationship between C_i and C_i' in (3-43) and (3-44) is established by utilizing the 2nd-order PDEs [Eqs. (2-42) and (2-43)] which, for the present case of a harmonic tip load, will be homogeneous ($\bar{Q} = 0$). Substituting the separable forms given by Eqs. (3-31) and (3-32) into those PDEs results in the following 2nd-order ODEs:

$$\bar{V}'' + s^2\lambda^2\left[\lambda\left(\lambda+\zeta\right) - i\zeta\lambda\right]\bar{V} - \Phi' = 0, \tag{3-45}$$

$$s^2\Phi'' - \left\{1 - \left[\lambda\left(\lambda+\zeta\right) - i\zeta\lambda\right]s^2r^2\lambda^2\right\}\Phi + \bar{V}' = 0, \tag{3-46}$$

which are rewritten for conciseness as

$$\bar{V}'' + k_3\bar{V} - \Phi' = 0, \tag{3-47}$$

$$s^2\Phi'' + \bar{V}' - \left\{1 - r^2k_3\right\}\Phi = 0, \tag{3-48}$$

where

$$k_3 = k_3(\lambda) = s^2\lambda^2\left[\lambda\left(\lambda+\zeta\right) - i\lambda\zeta\right]. \tag{3-49}$$

Applying (3-43) and (3-44) to (3-47) results in the following relationships:

$$C_1' = \frac{n_1^2(\lambda) + k_3(\lambda)}{n_1(\lambda)} C_1, \tag{3-50a}$$

$$C_2' = \frac{n_1^2(\lambda) + k_3(\lambda)}{-n_1(\lambda)} C_2, \tag{3-50b}$$

$$C_3' = \frac{n_3^2(\lambda) + k_3(\lambda)}{n_3(\lambda)} C_3, \tag{3-50c}$$

$$C_4' = \frac{n_3^2(\lambda) + k_3(\lambda)}{-n_3(\lambda)} C_4. \tag{3-50d}$$

Note that the same results can be obtained by utilizing Eq. (3-48) in lieu of (3-47). Imposing the BCs (3-35a-d) on the general solution form given by (3-43) and (3-44), and using (3-50a-d), leads to the following linear algebraic system:

$$[e]\{C^*\} = \{f\} \tag{3-51}$$

where

$$[e] = \begin{bmatrix} 1 & 0 & 1 & 0 \\ 0 & \frac{n_1^2 + k_3}{n_1} & 0 & -\frac{n_3^2 + k_3}{in_3} \\ \left[n_1^2 + k_3\right] C(n_1) & \left[n_1^2 + k_3\right] S(n_1) & \left[n_3^2 + k_3\right] \mathrm{c}(in_3) & \left[n_3^2 + k_3\right] \mathrm{s}(in_3) \\ \frac{1}{s^2}\left[n_1 - \frac{n_1^2 + k_3}{n_1}\right] S(n_1) & \frac{1}{s^2}\left[n_1 - \frac{n_1^2 + k_3}{n_1}\right] C(n_1) & \frac{1}{s^2}\left[-in_3 - \frac{n_3^2 + k_3}{in_3}\right] \mathrm{s}(in_3) & \frac{1}{s^2}\left[in_3 - \frac{n_3^2 + k_3}{-in_3}\right] \mathrm{c}(in_3) \end{bmatrix} \tag{3-52}$$

$$\{C^*\} = \begin{Bmatrix} C_1 / \bar{F}_0 \\ C_2 / \bar{F}_0 \\ C_3 / \bar{F}_0 \\ C_4 / \bar{F}_0 \end{Bmatrix} = \begin{Bmatrix} C_1^* \\ C_2^* \\ C_3^* \\ C_4^* \end{Bmatrix}, \tag{3-53}$$

$$\{f\} = \begin{Bmatrix} 0 \\ 0 \\ 0 \\ 1 \end{Bmatrix}, \tag{3-54}$$

and $S() \equiv \sinh()$, $C() \equiv \cosh()$, $s() \equiv \sin()$, $c() \equiv \cos()$.

The coefficients, C_i^* , i = 1, 2, 3, 4, depend on r, s, ζ and λ and are obtained by solving Eq. (3-51). These constants may then be used to convert (3-43) into

$$\bar{V}(\xi) = \bar{F}_0 \left[C_1^* C(n_1\xi) + C_2^* S(n_1\xi) + C_3^* \, \mathrm{c}(in_3\xi) + C_4^* \, \mathrm{s}(in_3\xi) \right]. \tag{3-55}$$

Similarly, the form (3-44) for $\Phi(\xi)$ becomes

$$\Phi(\xi) = \bar{F}_0 \left[C_1^{*\prime} C(n_1\xi) + C_2^{*\prime} S(n_1\xi) + C_3^{*\prime} \, \mathrm{c}(in_3\xi) + C_4^{*\prime} \, \mathrm{s}(in_3\xi) \right]. \tag{3-56}$$

Having determined the spatial dependence of the solution as (3-55) and (3-56), the time-dependence of the solution is provided by utilizing (3-31) and (3-32), i.e.,

$$\bar{v}(\xi,\tau) = \bar{V}(\xi) e^{i\tau}, \tag{3-57a}$$

$$\varphi(\xi,\tau) = \Phi(\xi) e^{i\tau}. \tag{3-57b}$$

The complete time-dependent beam response is described in terms of Eqs. (3-57a, b). Consequently, the beam response due to bending may be obtained as a secondary field of interest by applying Eq. (3-57b) to Eq. (2-62), resulting in

$$\bar{v}_B(\xi,\tau) = \bar{V}_B(\xi) e^{i\tau}, \tag{3-57c}$$

where

$$\bar{v}_B = \frac{v_B}{L}, \tag{3-58}$$

and

$$\begin{aligned} \bar{V}_B(\xi) &\equiv \int_0^\xi \Phi(\xi)\, d\xi \\ &= \bar{F}_0 \left[\frac{C_1^{*\prime}}{n_1} S(n_1\xi) + \frac{C_2^{*\prime}}{n_1} C(n_1\xi) + \frac{C_3^{*\prime}}{in_3} s(in_3\xi) - \frac{C_4^{*\prime}}{in_3} c(in_3\xi) - \left(\frac{C_2^{*\prime}}{n_1} - \frac{C_4^{*\prime}}{in_3} \right) \right]. \end{aligned} \tag{3-59}$$

The secondary field associated with displacement due to shear may be obtained by substituting Eqs. (3-57a, b) into Eq. (2-63) and utilizing Eq. (3-59), resulting in

$$\bar{v}_S(\xi,\tau) = \bar{V}_S(\xi) e^{i\tau}, \tag{3-60}$$

in which

$$\bar{V}_S(\xi) \equiv \bar{V}(\xi) - \bar{V}_B(\xi) \tag{3-61}$$

and the detailed forms of $\bar{V}(\xi)$ and $\bar{V}_B(\xi)$ are given in Eqs. (3-55) and (3-59).

Of particular interest in this study is the magnitude of the beam response amplitude at or near the first resonant peak in lateral flexure. As discussed in Sect. 1.5, since sensor response is typically measured either optically at the tip or via piezoresistive elements monitoring bending strain near the support, the magnitude of both the total displacement, $\bar{V}(1)$, and the bending displacement, $\bar{V}_B(1)$, are of practical interest.

The magnitude of the total displacement amplitude at the tip, corresponding to (3-55) evaluated at $\xi = 1$, may be scaled by the static tip displacement of an Euler-Bernoulli beam, $V_{EB,static}(1)$, thereby resulting in the following normalized total tip displacement amplitude, D_T:

$$D_T \equiv \frac{\left|L\bar{V}(1)\right|}{V_{EB,static}(1)} = \frac{L\left|\bar{V}(1)\right|}{F_0 L^3/3EI} = \frac{3EI}{F_0 L^2}\left|\bar{V}(1)\right| = \frac{3}{\bar{F}_0}\left|\bar{V}(1)\right|. \tag{3-62}$$

Applying Eq. (3-55) to (3-62) results in

$$D_T = 3\left|C_1^* C(n_1) + C_2^* S(n_1) + C_3^* \,\mathrm{c}(in_3) + C_4^* \,\mathrm{s}(in_3)\right|. \tag{3-63}$$

In an analogous manner the normalized tip displacement amplitude due to bending only, D_B, may be defined by scaling the magnitude of the tip displacement amplitude due to bending by the static tip displacement of an Euler-Bernoulli beam. This provides

$$\begin{aligned} D_B &\equiv \frac{\left|L\bar{V}_B(1)\right|}{V_{EB,static}(1)} = \frac{3}{\bar{F}_0}\left|\bar{V}_B(1)\right| \\ &= 3\left|\frac{C_1^{*\prime}}{n_1} S(n_1) + \frac{C_2^{*\prime}}{n_1} C(n_1) + \frac{C_3^{*\prime}}{in_3} s(in_3) - \frac{C_4^{*\prime}}{in_3} c(in_3) - \left(\frac{C_2^{*\prime}}{n_1} - \frac{C_4^{*\prime}}{in_3}\right)\right|. \end{aligned} \tag{3-64}$$

Similarly, the magnitude of the shear displacement amplitude at the tip may be expressed in terms of a normalized quantity, D_S, representing the ratio of the magnitude of the tip displacement amplitude due to shear to the static tip displacement of an Euler-Bernoulli beam:

$$D_S \equiv \frac{\left|L\bar{V}_S(1)\right|}{V_{EB,static}(1)} = \frac{3}{\bar{F}_0}\left|\bar{V}(1) - \bar{V}_B(1)\right| \quad . \tag{3-65}$$

The explicit form of Eq. (3-65) can be obtained by substituting Eqs. (3-55) and (3-59) into (3-65).

Equations (3-63), (3-64) and (3-65) provide the normalized beam response at the tip for the amplitudes of total displacement, displacement due to bending, and displacement due to shear, respectively. Equation (3-63) is the relevant response quantity for applications that directly monitor the tip position, while Eq. (3-64) provides a response metric that is approximately proportional to the beam's bending strain. (See explanation in Sect. 1.5.) Thus, in the vicinity of a resonant peak the value furnished by (3-64) is a normalized version of the bending strain that would be measured by piezoresistors near the support, i.e., of the type used in the devices of the Georgia Tech/Marquette group [Beardslee et al., 2010a; 2012]. These results [(3-63) and (3-64)] will be used in Ch. 4 to determine the resonant frequencies for a tip-loaded microcantilever for the two different types of output signals. This will be accomplished by calculating the respective tip deflection over a range of excitation frequencies and identifying the frequency at which maximum tip deflection (i.e., resonance) occurs. Using the resulting theoretical frequency response plot, the quality factor may be calculated using the well-known 3-dB bandwidth method. Note that the resonant frequencies and corresponding bandwidth-based quality factors could depend on, not only the excitation scheme (loading type) used, but also on the method used for detecting the beam response (the type of output signal).

Also note that, by setting the fluid resistance parameter, ζ, to zero, the new solution derived in this section will reduce to the in-vacuum response of the Timoshenko beam under a harmonic tip load.

3.4 Forced Vibration in Fluid – Harmonic Support Rotation

The solution method for forced vibration of an in-fluid Timoshenko beam via an imposed harmonic support rotation is analogous to the procedure presented in Sect. 3.3 for forced vibration via a harmonic tip force. The general solution forms for the functions $\bar{V}(\xi)$ and $\Phi(\xi)$ are still given by (3-55) and (3-56); however, the BCs for the case of harmonic support rotation now are of the form [see Eqs. (2-61a-d)]

$$\bar{V}(0) = 0\,, \tag{3-66a}$$

$$\Phi(0) = \theta_0\,, \tag{3-66b}$$

$$\Phi'(1) = 0\,, \tag{3-66c}$$

$$\bar{V}'(1) - \Phi(1) = 0\,. \tag{3-66d}$$

Equations (3-66a-d) result in the following four-by-four system of linear algebraic equations:

$$[e]\{C^*\} = \{f\} \tag{3-67}$$

$$[e] = \begin{bmatrix} 1 & 0 & 1 & 0 \\ 0 & \dfrac{n_1^2 + k_3}{n_1} & 0 & -\dfrac{n_3^2 + k_3}{in_3} \\ \left[n_1^2 + k_3\right] C(n_1) & \left[n_1^2 + k_3\right] S(n_1) & \left[n_3^2 + k_3\right] \mathrm{c}(in_3) & \left[n_3^2 + k_3\right] \mathrm{s}(in_3) \\ \left[n_1 - \dfrac{n_1^2 + k_3}{n_1}\right] S(n_1) & \left[n_1 - \dfrac{n_1^2 + k_3}{n_1}\right] C(n_1) & \left[-in_3 - \dfrac{n_3^2 + k_3}{in_3}\right] \mathrm{s}(in_3) & \left[in_3 - \dfrac{n_3^2 + k_3}{-in_3}\right] \mathrm{c}(in_3) \end{bmatrix} \tag{3-68}$$

$$\{C^*\} = \begin{Bmatrix} C_1 / \theta_0 \\ C_2 / \theta_0 \\ C_3 / \theta_0 \\ C_4 / \theta_0 \end{Bmatrix} = \begin{Bmatrix} C_1^* \\ C_2^* \\ C_3^* \\ C_4^* \end{Bmatrix}\,, \tag{3-69}$$

$$\{f\} = \begin{Bmatrix} 0 \\ 1 \\ 0 \\ 0 \end{Bmatrix}. \tag{3-70}$$

The solution is obtained and written as was done in Sect. 3.3. The results for total displacement, bending slope and bending displacement are again given by the harmonic forms of Eqs. (3-57a-c), i.e.,

$$\bar{v}(\xi,\tau) = \bar{V}(\xi)e^{i\tau}, \tag{3-71}$$

$$\varphi(\xi,\tau) = \Phi(\xi)e^{i\tau}, \tag{3-72}$$

and

$$\bar{v}_B(\xi,\tau) = \bar{V}_B(\xi)e^{i\tau}, \tag{3-73}$$

but now the complex amplitudes take the following forms:

$$\bar{V}(\xi) = \theta_0\left[C_1^*C(n_1\xi) + C_2^*S(n_1\xi) + C_3^*\,\mathrm{c}(in_3\xi) + C_4^*\,\mathrm{s}(in_3\xi)\right], \tag{3-74}$$

$$\Phi(\xi) = \theta_0\left[C_1^{*\prime}C(n_1\xi) + C_2^{*\prime}S(n_1\xi) + C_3^{*\prime}\,\mathrm{c}(in_3\xi) + C_4^{*\prime}\,\mathrm{s}(in_3\xi)\right], \tag{3-75}$$

and

$$\bar{V}_B(\xi) = \theta_0\left[\frac{C_1^{*\prime}}{n_1}S(n_1\xi) + \frac{C_2^{*\prime}}{n_1}C(n_1\xi) + \frac{C_3^{*\prime}}{in_3}s(in_3\xi) - \frac{C_4^{*\prime}}{in_3}c(in_3\xi) - \left(\frac{C_2^{*\prime}}{n_1} - \frac{C_4^{*\prime}}{in_3}\right)\right]. \tag{3-76}$$

The tip response is obtained by evaluating the above equations at ξ=1.

Unlike the case of a harmonic tip force (Sect. 3.3), the case of imposed support rotation introduces some displacement due to rigid body motion, which is included in Eq. (3-73). Since the piezoresistive method of response detection only monitors bending *deformation* (i.e., strain due to bending), it is important to introduce a bending deformation-only response quantity that does not include the rigid-body motion contribution that is present in Eq. (3-73). To this end, an expression is sought for the "bending-deformation displacement," $\bar{V}_{B-D}(\xi)$, as follows. Recall that the time-varying, imposed support rotation is of the form

$$\theta(t) = \theta_0 e^{i\omega t}, \tag{3-77}$$

where θ_0 is the amplitude of the rotation. The time-dependent, rigid displacement associated with this excitation is therefore given by

$$v_R(x,t) = x\,\theta(t)\,, \tag{3-78}$$

in which the assumption of small rotations has been employed. The dimensionless deflection due to the rigid body motion is defined by

$$\bar{v}_R \equiv \frac{v_R}{L}\,. \tag{3-79}$$

Applying (3-77) and (3-79) to (3-78) yields the normalized form of the rigid displacement in terms of dimensionless coordinates ξ and τ :

$$\bar{v}_R(\xi,\tau) = \frac{x\theta_0 e^{i\omega t}}{L} = \xi\theta_0 e^{i\tau}\,. \tag{3-80}$$

At the tip (3-80) becomes

$$\bar{v}_R(1,\tau) = \theta_0 e^{i\tau}\,. \tag{3-81}$$

Recall, from Fig. 1-4, that the definition of the displacement due solely to bending *deformation* is

$$\bar{v}_{B-D}(\xi,\tau) \equiv \bar{v}_B(\xi,\tau) - \bar{v}_R(\xi,\tau)\,. \tag{3-82}$$

Applying (3-73) and (3-81) to (3-82) results in the tip deflection associated with bending deformation:

$$\bar{v}_{B-D}(1,\tau) = \bar{v}_B(1,\tau) - \bar{v}_R(1,\tau) = \bar{V}_{B-D}(1)e^{i\tau}\,, \tag{3-83}$$

where

$$\bar{V}_{B-D}(1) \equiv \bar{V}_B(1) - \theta_0 \qquad . \tag{3-84}$$

Equation (3-83) may be rewritten as

$$\bar{v}_{B-D}(1,\tau) = \left[\frac{\bar{V}_B(1)}{\theta_0} - 1\right]\theta_0 e^{i\tau} = \left[\frac{\bar{V}_{B-D}(1)}{\theta_0}\right]\theta_0 e^{i\tau}\,. \tag{3-85}$$

The complex coefficient of (3-85) may be written in polar form as

$$\frac{\bar{V}_{B-D}(1)}{\theta_0} = \frac{\bar{V}_B(1)}{\theta_0} - 1 = \left| \frac{\bar{V}_B(1)}{\theta_0} - 1 \right| e^{i(-\bar{\beta})}, \tag{3-86}$$

where

$$\bar{\beta} \equiv -\tan^{-1}\left\{ \frac{\mathrm{Im}\left[\frac{\bar{V}_B(1)}{\theta_0} - 1 \right]}{\mathrm{Re}\left[\frac{\bar{V}_B(1)}{\theta_0} - 1 \right]} \right\} \tag{3-87}$$

is the phase angle associated with the tip's bending-deformation displacement, i.e., it represents the angle by which the bending-deformation displacement at the tip lags the imposed support rotation. Applying (3-86) to (3-85) provides the bending-deformation displacement at the tip:

$$\bar{v}_{B-D}(1,\tau) = \left| \frac{\bar{V}_{B-D}(1)}{\theta_0} \right| \theta_0 e^{i(-\bar{\beta})} e^{i\tau} = \left| \frac{\bar{V}_B(1)}{\theta_0} - 1 \right| \theta_0 e^{i(\tau-\bar{\beta})} \quad . \tag{3-88}$$

Recall that θ_0 is the input amplitude and that it impacts the system linearly; therefore, for convenience all results can be scaled by θ_0 without loss of generality. To this end, Eqs. (3-76) and (3-88) are used to express the amplitude of $\frac{\bar{v}_{B-D}(1,\tau)}{\theta_0}$ as

$$\left| \frac{\bar{V}_{B-D}(1)}{\theta_0} \right| = \left| \frac{\bar{V}_B(1)}{\theta_0} - 1 \right| = \left| \frac{C_1^{*\prime}}{n_1} S(n_1) + \frac{C_2^{*\prime}}{n_1} C(n_1) + \frac{C_3^{*\prime}}{in_3} s(in_3) - \frac{C_4^{*\prime}}{in_3} c(in_3) - \left(\frac{C_2^{*\prime}}{n_1} - \frac{C_4^{*\prime}}{in_3} \right) - 1 \right|, \tag{3-89}$$

which provides an output quantity that is approximately proportional to the bending strain that is measured by the piezoresistors near the support of the Georgia Tech/Marquette devices. This quantity depends only on the dimensionless parameters *r* and *s* (Timoshenko beam parameters), λ (dimensionless exciting frequency), and ζ (fluid resistance parameter).

For the case of harmonic support rotation the quantity of most interest is the magnitude of the beam response amplitude at or near the first resonant peak in lateral flexure, as measured by both the total tip displacement, having complex amplitude $\bar{V}(1)$, and the bending-deformation tip displacement, of complex amplitude $\bar{V}_{B-D}(1)$. As was done for the tip-loading case, convenient normalized metrics for these quantities may be derived by introducing a physically

meaningful scaling factor. In the present case the scaling factor will represent the tip displacement amplitude associated with only the rigid beam rotation, $L\theta_0$.

The magnitude of the total displacement amplitude at the tip, corresponding to (3-74) evaluated at ξ=1, may be scaled by the rigid rotation amplitude, $L\theta_0$, thereby resulting in the following normalized tip displacement amplitude for the case of a harmonic support rotation, D_T:

$$D_T \equiv \frac{\left|L\bar{V}(1)\right|}{L\theta_0} = \frac{\left|\bar{V}(1)\right|}{\theta_0} . \tag{3-90}$$

Applying Eq. (3-74) to (3-90) results in

$$D_T = \left|C_1^* C(n_1) + C_2^* S(n_1) + C_3^* \,\mathrm{c}(in_3) + C_4^* \,\mathrm{s}(in_3)\right| . \tag{3-91}$$

The normalized tip displacement amplitude due to bending deformation only, $D_{B\text{-}D}$, may be defined by scaling the magnitude of the tip displacement amplitude due to bending deformation (utilizing (3-89)) by the rigid tip displacement:

$$D_{B-D} \equiv \frac{\left|L\bar{V}_{B-D}(1)\right|}{L\theta_0} = \frac{\left|\bar{V}_{B-D}(1)\right|}{\theta_0} = \left|\frac{C_1^{*\prime}}{n_1} S(n_1) + \frac{C_2^{*\prime}}{n_1} C(n_1) + \frac{C_3^{*\prime}}{in_3} s(in_3) - \frac{C_4^{*\prime}}{in_3} c(in_3) - \left(\frac{C_2^{*\prime}}{n_1} - \frac{C_4^{*\prime}}{in_3}\right) - 1\right| . \tag{3-92}$$

Similarly, the normalized tip displacement amplitude due to shear may be obtained by scaling the magnitude of the tip displacement amplitude due to shear (following the approach used in Sect. 3.3) by the rigid tip displacement amplitude:

$$D_S \equiv \frac{\left|L\left[\bar{V}(1) - \bar{V}_B(1)\right]\right|}{L\theta_0} = \frac{\left|\bar{V}(1) - \bar{V}_B(1)\right|}{\theta_0} \tag{3-93}$$

The explicit form of Eq. (3-93) can be obtained by evaluating (3-74) and (3-76) at the tip and substituting the results into (3-93).

Equations (3-91), (3-92) and (3-93) provide the normalized beam response at the tip for the amplitudes of total displacement, displacement due to bending deformation, and shear displacement, respectively. Equation (3-91) is relevant for applications that directly monitor the tip position, while Eq. (3-92) provides a response metric that corresponds to the beam's bending

strain. Thus, as noted in the previous section, the value furnished by (3-92) represents a normalized version of the bending strain that would be measured by piezoresistors near the support. These results [(3-91) and (3-92)] will be used in Ch. 4 to determine the resonant frequencies and quality factors for a microcantilever undergoing harmonic support rotation (e.g., via electrothermal excitation at the supported end) for the two different types of output signals using methods.

CHAPTER 4: NUMERICAL RESULTS AND DISCUSSION

4.1 Introductory Remarks

Chapter 4 opens with a presentation of results for the in-vacuum, free vibration of a Timoshenko beam followed by results for the in-fluid, forced vibration via harmonic tip force and support rotation, respectively. In the free-vibration case the natural frequencies given by Eqs. (3-18) and (3-25) are compared to those provided by Kruszewski [1949], Huang [1961] and Abramovich and Elishakoff [1990]. Achieving confidence in the calculation of in-vacuum, free-vibration results by comparison to existing literature is important before the introduction of complicating fluid effects. Having verified the methods for obtaining the eigenvalues for the in-vacuum case, the corresponding eigenfunctions, given by Eqs. (3-19) and (3-26), are compared to those provided by Huang [1963]. For both cases of in-fluid, forced vibration, the theoretical solutions derived in Ch. 3 are used to generate frequency response curves of the tip displacement amplitude, resonant frequencies, quality factors, and vibrational shapes. In addition the results for resonant frequency and quality factor are compared to experimental results. By presenting these numerical results, this chapter seeks to quantify the effects of Timoshenko beam parameters r and s (or, equivalently, b/L and $\sqrt{E/kG}$) as well as ζ (fluid resistance parameter) on beam response. Two types of forced vibration (imposed harmonic support rotation and harmonic tip force) are investigated and the results are presented for various system response parameters. In each loading case, results for the magnitude of the normalized total displacement amplitude at the beam tip (i.e., D_T) will be examined. In the case of the harmonic tip force the magnitudes of the normalized bending displacement and shear displacement amplitudes at the beam tip (i.e., D_B and D_S) will also be investigated. For the case of imposed harmonic support rotation some results will be expressed in terms of the magnitude of the normalized tip displacement amplitude due to bending deformation only (i.e., $D_{B\text{-}D}$) as well as that due to shear only (i.e., D_S). The results for the quality

factor are used to obtain a simplified analytical equation for estimating the quality factor for a thin Timoshenko beam vibrating laterally in a viscous fluid. Finally, for verification purposes the in-fluid, forced vibration results are compared to numerical results obtained from a MATLAB solver [Mathworks, 2010], to analogous results from the literature for in-fluid Euler-Bernoulli beam models, and to experimental data.

4.2 Parametric Study of Free Vibration of Timoshenko Beam in Vacuum

To validate the model summarized in Sect. 3.2, the following plots of frequency change due to Timoshenko beam effects (non-zero r and s values) compare results presented by Huang [1961] with those obtained as a result of Eqs. (3-18) and (3-25) as shown in Fig. 4-1a, b.

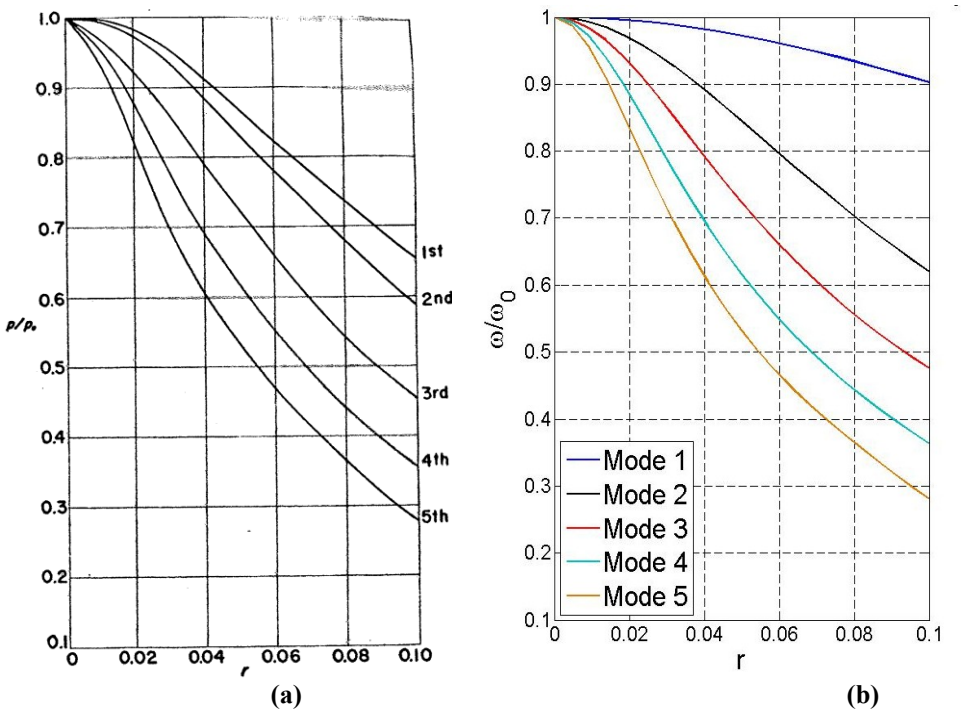

Figure 4-1: Corrections in Natural Frequencies ($p/p_0 = \omega/\omega_0$) of a Cantilever Beam Due to Rotatory Inertia (r) and Shear Deformation ($s = 2r$) for First Five Modes: (a) Huang [1961] (b) present study employing equations derived by Huang [1961].

The results of Fig. 4-1(b) were obtained by numerically determining the roots of the frequency equation, either Eq. (3-18) or (3-25), for the case of $s = 2r$ and then comparing with those appearing in Huang's original 1961 paper and reproduced here in Fig. 4-1(a). Clearly, there is a discrepancy between the results of frequency ratio vs. r for the first three modes as shown in Fig. 4-1. In an attempt to resolve this discrepancy, additional verification was performed using the results of Abramovich and Elishakoff [1990], who calculated the frequency ratio for the first four modes, which provide excellent quantitative comparison to the results generated in the present study (Fig. 4-1b). Specifically, the frequency ratios for the first four modes when $r = 0.02$ and $s = 2r = 0.04$ are given in Table 1:

Mode:	Abramovich & Elishakoff [1990]	Huang [1961]	Present study employing Eqs. derived by Huang [1961]
1	0.995	0.985	0.995
2	0.969	0.975	0.969
3	0.931	0.930	0.932
4	0.882	0.883	0.883

Table 4-1: Frequency Ratio for First Four Modes of Free Vibration of an In-Vacuum Timoshenko Beam for $r = 0.02$ and $s = 0.04$

As a final check of the eigenvalues, the natural frequency results as calculated in the present study are compared against the results given by Kruszewski [1949] in Fig. 4-2 for various combinations of r and s. Figure 4-2 demonstrates excellent agreement between the frequency results of Kruszewski and those generated in the present study. This comparison, in conjunction with the comparison displayed in Table 4-1, provides validation of the present free-vibration results for the in-vacuum case so that they may be used with confidence when interpreting the new forced-vibration results for the in-fluid case that will be presented subsequently. In summary, it appears that there exists an error in Huang's plot of the natural frequencies for the first three modes based on frequency comparisons among Kruszewski [1949], Huang [1961], Abramovich and Elishakoff [1990], and the present results (that are based on Huang's equations).

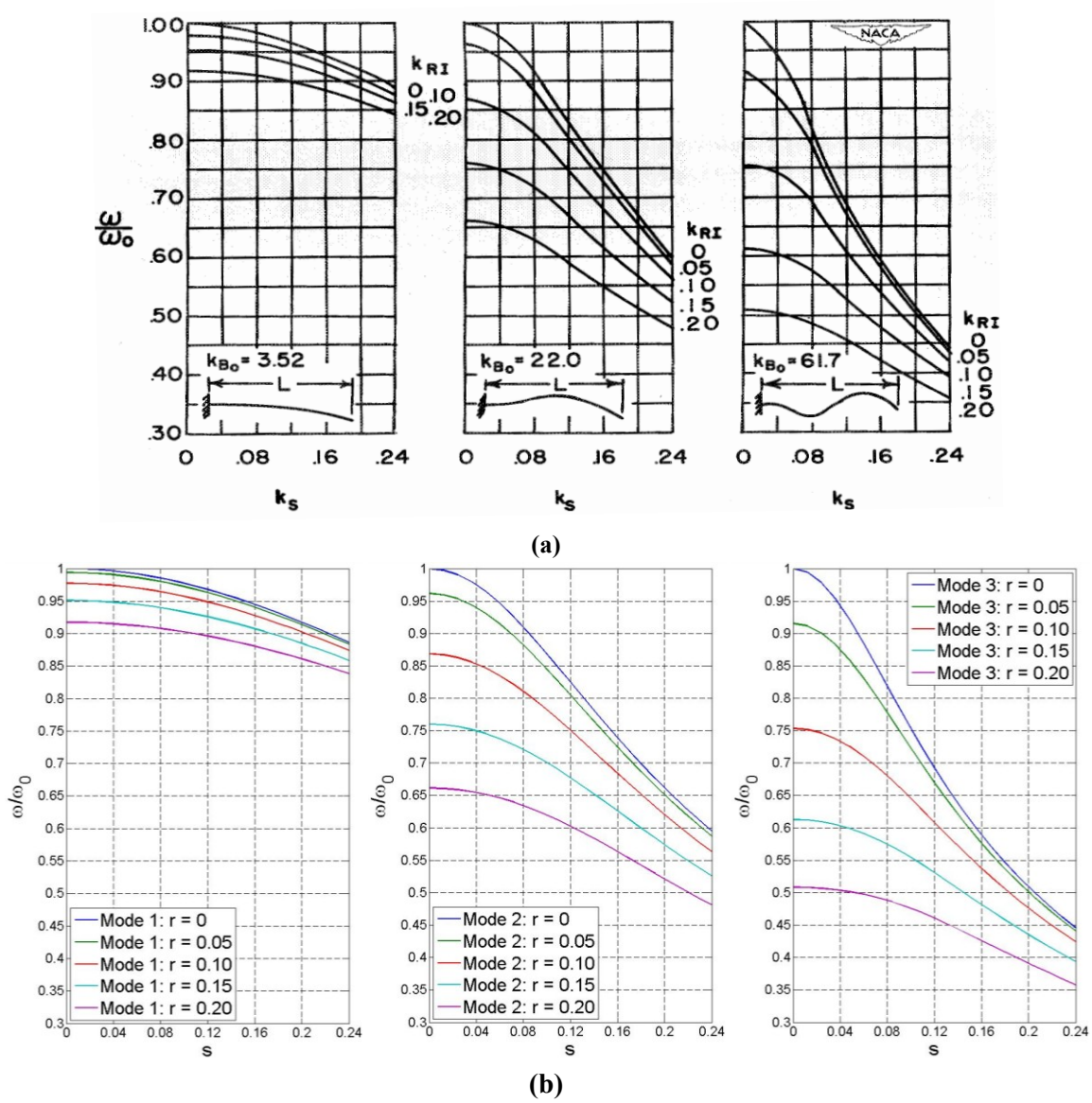

Figure 4-2: Corrections in Natural Frequency (ω/ω_0) of a Cantilevered Beam Due to Shear ($k_s = s$) and Rotatory Inertia ($k_{RI} = r$) for First Three Modes: (a) Kruszewski [1949] (b) present study employing equations derived by Huang [1961].

The natural frequency trends in Figs. 4-1 and 4-2 and in Table 4-1 are consistent: increasing the Timoshenko parameters (r and s) results in a reduction of the natural frequency — increasingly so at higher modes of vibration. To understand this trend, recall the definitions of the rotational inertia parameter,

$$r^2 \equiv \frac{1}{12}\left(\frac{b}{L}\right)^2, \tag{4-1}$$

and the shear deformation parameter,

$$s^2 \equiv r^2\left(\frac{E}{kG}\right). \tag{4-2}$$

For isotropic materials, the ratio of *E/G* can be expressed in terms of Poisson's ratio; however, here the ratio of *E*/*G* is employed so that Eq. (4-2) can be applied readily to an anisotropic material by specifying the appropriate values of *E* and *G*. More specifically, the value of *E* should correspond to the longitudinal (*x*) direction and *G* to the in-plane (*x*-*y*) directions. (See Fig. 2-4.)

The trends exhibited by the natural frequency results are readily interpreted in light of the analogous natural frequency definition for an undamped SDOF system ("$\omega = \sqrt{k/m}$") with and without consideration of Timoshenko effects. First, consider the effect of increasing the Timoshenko parameter associated with shear deformation, *s*. For a constant modulus of elasticity increasing the shear parameter may be interpreted as a decrease in the shear modulus (i.e., resistance to shear), which results in a more flexible system and, thus, a lower natural frequency. Second, consider the effect of the Timoshenko parameter associated with the rotational inertia of the system, *r*. An increase in the rotational inertia parameter corresponds to increased inertial mass effects, i.e., an increased effective mass, and consequently a reduced natural frequency. In summary, the Timoshenko effects will result in a more flexible system with higher mass effects than the artificially stiffer Euler-Bernoulli equivalent. As a result, the system with Timoshenko effects included will have a lower natural frequency than the one with described by Euler-Bernoulli theory.

Having verified the eigenvalues calculated herein for the in-vacuum case, a check on the eigenfunctions (mode shapes) based on Eqs. (3-19) and (3-26) (which were derived in Huang [1961]) may be made by comparison with the discrete values provided by Huang [1963] for the

special case of $r = 0.02$ and $s = 0.04$. Equations (3-19) and (3-26) are used to plot the first five continuous mode shapes for both the total displacement and the bending slope in Figs. 4-3 and 4-4, respectively, along with discrete values from Huang [1963]. The excellent agreement between the Huang values for total displacement, $V(\xi)$, and bending slope, $\Phi(\xi)$, and those provided by

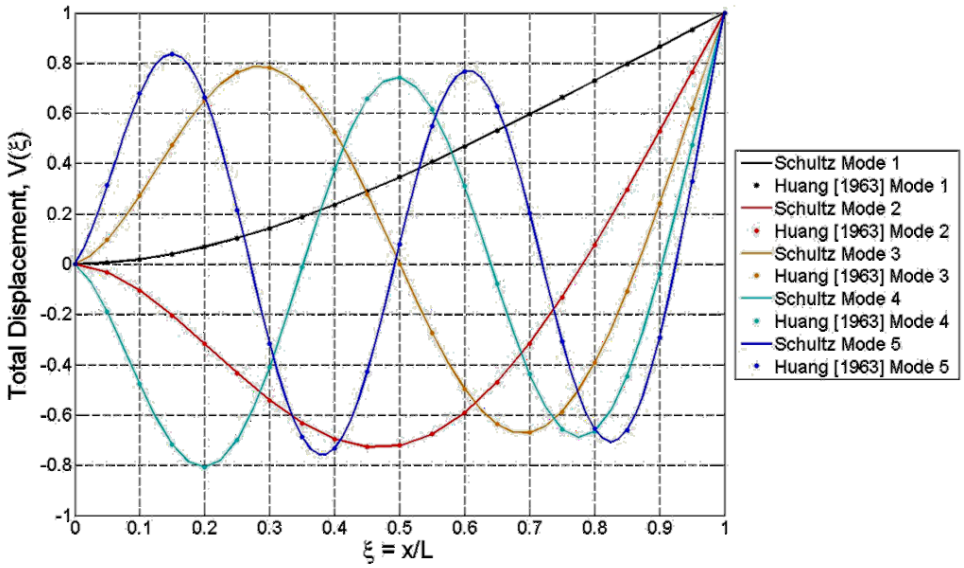

Figure 4-3: Huang [1963] and Present Model ("Schultz") Modes 1-5 Total Displacement Comparison, $r = 0.02$ and $s = 0.04$

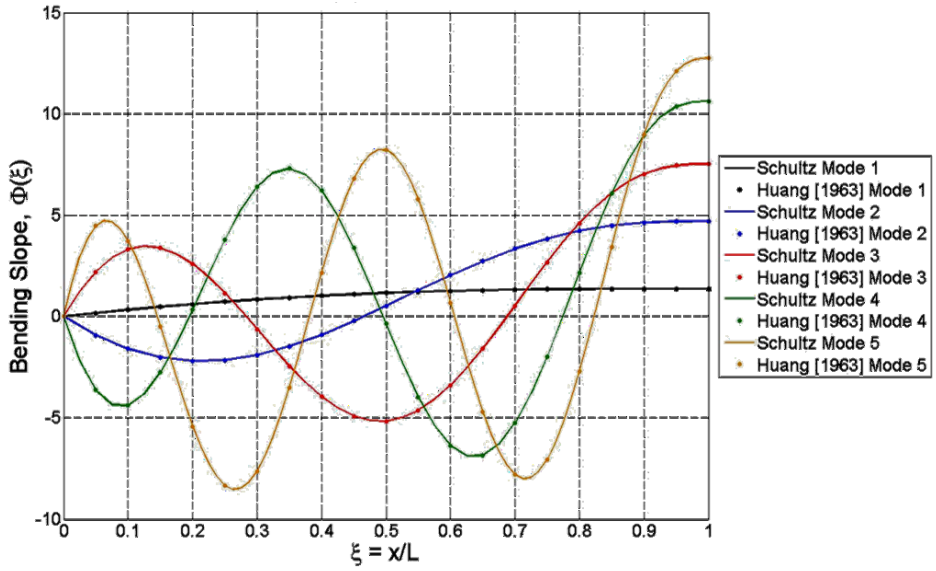

Figure 4-4: Huang [1963] and Present Model ("Schultz") Modes 1-5 Bending Slope Comparison, $r = 0.02$ and $s = 0.04$

Eqs. (3-19) and (3-26) as shown by Figs. 4-3 and 4-4 confirms the accuracy of the mode shapes as calculated in the present study, so that these shapes may serve as a reference for the interpretation of the vibrational shapes that will be examined in the cases of forced vibration.

4.3 Parametric Study: In-Fluid Lateral Vibration of a Thin Microcantilever Due to a Harmonic Tip Load

This section investigates the beam response of the in-fluid, lateral vibration of a thin microcantilever due to a harmonic tip load by presentation of the following: frequency response curves of tip displacement, the associated values of resonant frequency and quality factor, and the vibrational beam shapes. While the frequency response curves are generated over frequency ranges spanning multiple modes of vibration, the resonant frequency and quality factors for the first mode are the primary focus of this and subsequent sections of this chapter due to the practical difficulties of exciting higher-order (stiffer) lateral modes. The effects of beam geometry, beam material and fluid resistance on beam response (resonant frequency and quality factor) are presented. Recalling Eqs. (4-1) and (4-2), it is noted that r is proportional to b/L (i.e., geometry) and s is related to r via the factor $\sqrt{E/kG}$ (i.e., material). Thus, these pairs of parameters will be used interchangeably in the plots throughout this chapter. While this section explores the effects of the Timoshenko beam parameters and the fluid resistance parameter on beam response, it is not intended as an exhaustive parametric study. Instead, the plots are intended to highlight overall trends in the resonant frequency and quality factor with respect to Timoshenko and fluid resistance parameters.

The frequency response curves in Fig. 4-5 display the normalized tip displacement for a range of excitation frequencies in terms of the total displacement, D_T, the bending displacement, D_B, and the shear displacement, D_S. Figure 4-5a displays the multi-modal frequency response curves over a range of frequency $\lambda \in [1,5]$, while Fig. 4-5b zooms in on the first-mode response

(frequency range $\lambda \in [1.2, 2.2]$) and Fig. 4-5c the second-mode curves ($\lambda \in [2.5, 5]$). Figure 4-5 displays the frequency response curves for the specific value of $b/L = 0.45$ ($r = 0.13$) which corresponds to $L = 200$ μm and $b = 90$ μm (i.e., the dimensions of the shortest and widest specimen considered in associated experimental work [Beardslee et al., 2010a-d; Beardslee et al., 2011a]). The value of $\zeta = 0.05$ is employed as it represents the approximate value of the Stokes' fluid resistance parameter for the previously described geometry (taking h=5 μm, silicon properties of $E = 169$ GPa and $\rho_b = 2330$ kg/m^3, and fluid properties for water of $\rho_f = 1000$ kg/m^3 and $\eta = 0.001$ Pa-s). The results for the first-mode response curves in Fig. 4-5 highlight the following: (1) the impact of Timoshenko beam shear deformation (typified by $\sqrt{E/kG}$) on beam response and (2) the differences in the frequency response for different measured quantities at the tip (e.g., amplitude of total displacement and the amplitude of bending displacement).

The frequency response curves in Fig. 4-5a show the dramatic decrease in the amplitude of beam response between the first and second modes of vibration. The decrease between the amplitude of the first and second modes represents one advantage associated with using the first mode for sensing. However, Fig. 4-5a also highlights a change in the relative sizes of the total displacement and bending displacement amplitudes as the mode number is increased from 1 to 2; for example, while D_T is greater than D_B for the first mode, it is less than D_B for the second mode. Note that for the first mode, all three response quantities at or near the resonant frequency are in-phase; thus, the total displacement amplitude is the summation of the bending and shear displacement amplitudes. For the second mode, however, the fact that D_T is less than D_B may be explained by the fact that the total and bending displacements are in-phase with each other while the shear displacement is 180° out-of-phase with the total and bending displacements. This change in behavior could be particularly relevant since the bending displacement amplitudes at the second mode for devices with high Timoshenko and fluid resistance parameters have the added benefit of a higher resonant frequency and larger amplitudes than those associated with the

total displacement. Thus, if one may sufficiently excite the second mode, it might not only exhibit higher sensitivity (mass sensitivity is proportional to resonant frequency [e.g., Dufour et al., 2007a]), but this advantage may be exacerbated if the beam motion is monitored using an output signal that is based on bending deformation (e.g., piezoresistors at the extreme fibers near the supported end) in lieu of total displacement.

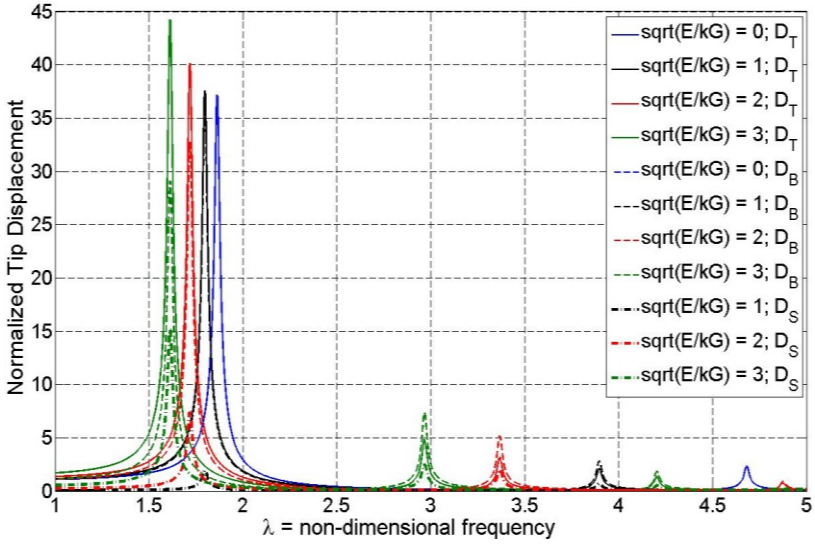

(a)

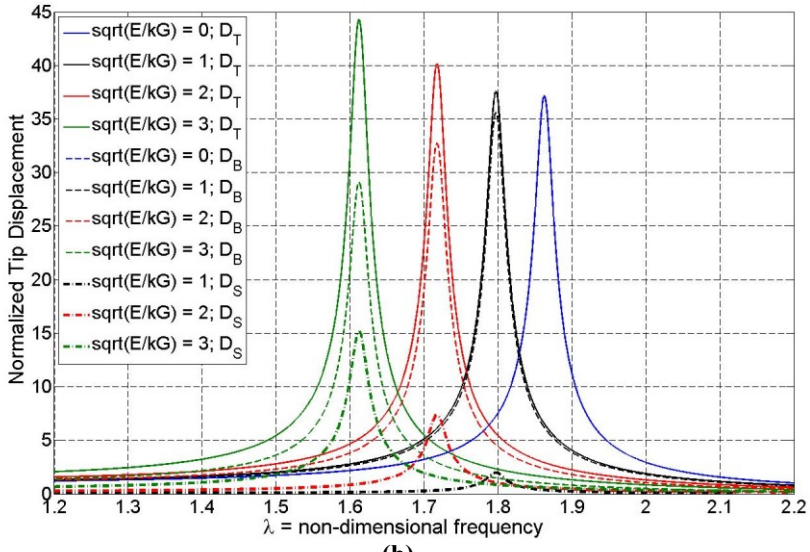

(b)

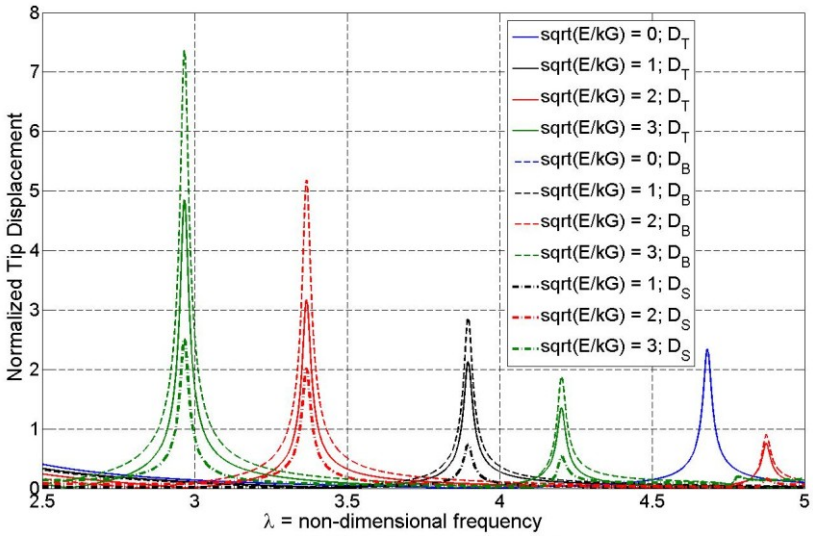

(c)

Figure 4-5: Frequency Response Curves of Normalized Tip Displacement for Various Material Properties, $\sqrt{E/kG}$, for $b/L = 0.45$ ($r = 0.13$) and $\zeta = 0.05$ Under Harmonic Tip Load as Measured by D_T, D_B and D_S: (a) $\lambda \in [1,5]$ (b) $\lambda \in [1.2,2.2]$ (c) $\lambda \in [2.5,5]$

For the range $\lambda \in [1,5]$ in Fig. 4-5a, an increase in $\sqrt{E/kG}$ results in changes in normalized total, bending and shear displacement amplitudes and resonant frequencies. Since D_T and D_B are both scaled by the static displacement of Euler-Bernoulli theory, the increase in $\sqrt{E/kG}$ may be interpreted solely as a decrease in the shear modulus (i.e., a decreased resistance to shear deformation) which results in increased displacement amplitudes for the total and shear displacements. However, for the first mode response in Fig. 4-5b, an increase in $\sqrt{E/kG}$ results in a decrease in the accompanying amplitude of D_B, while the second mode response in Fig. 4-5c shows an increase in the amplitude of D_B. Interestingly, the total displacement amplitude is greater than the bending displacement amplitude for the mode-1 case as shown in Fig. 4-5b, whereas the bending displacement amplitude is greater than the total displacement amplitude for higher modes as shown in Fig. 4-5c.

Comparing the plots a-c in Figure 4-5 shows that, as $\sqrt{E/kG}$ increases, the resonant frequency decreases with increases in this parameter. This is due to the decreased stiffness associated with increases in the Timoshenko parameter s as discussed in Sect. 4.2.

While Fig. 4-5 shows the impact of the shear parameter (i.e., $\sqrt{E/kG}$) and the measured response quantity (e.g., D_T, D_B or D_S) on the frequency response curves, Figs. 4-6 and 4-7 highlight the behavior of the system in the limiting case when the exciting frequency approaches zero (i.e., quasi-static loading scenario). The frequency response curves of Fig. 4-6 correspond to values of $\sqrt{E/kG} = (0,1,2,3)$, while those of Fig. 4-7 are plotted for b/L = (0.035, 0.17, 0.35, 0.52, 0.69). Figures 4-6 and 4-7 are plotted for a high value of the fluid resistance parameter, ζ = 2, in order to facilitate observation of the frequency response curves as the forcing frequency approaches zero, and also to highlight that the response (the total as well as the bending and shear portions) is in-phase even at high fluid resistance values. The behavior of the system as measured by D_B shows that as the frequency approaches zero, the normalized tip displacement approaches one for the static load case. However, if the behavior is observed using D_T, the tip displacement for non-zero $\sqrt{E/kG}$ values does not approach one, but instead approaches values greater than one. This behavior is readily explicable in light of the normalization of the system by the Euler-Bernoulli (EB) static tip displacement. Since the static EB theory does not account for the effects of shear deformation, as the $\sqrt{E/kG}$ parameter increases there will be increased displacement (beyond the bending portion) due to the shearing effects. It is observed in Figs. 4-6 and 4-7 that the peaks of the frequency response curves as measured by D_T and D_B occur at the same frequency. This indicates that, as noted earlier, the total, bending and shear response for the first mode are in-phase, even for the higher values of the Timoshenko ($\sqrt{E/kG} = 3$) and fluid resistance ($\zeta = 2$) parameters.

The normalized resonant frequency for mode 1 is shown in Figs. 4-8a-d as a function of the Timoshenko beam parameters and ζ. These frequency values are obtained from the first

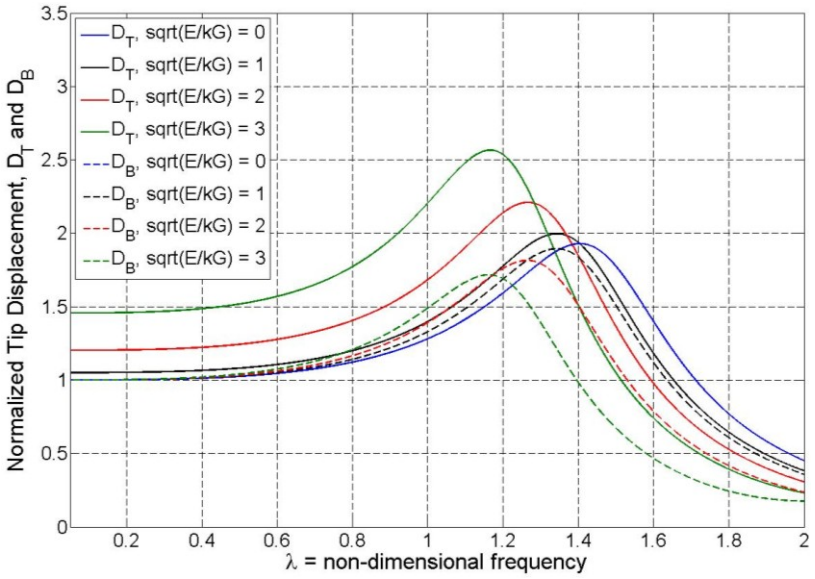

Figure 4-6: Frequency Response Curves of Normalized Tip Displacement of Various Material Properties, $\sqrt{E/kG}$ for b/L = 0.45 (r = 0.13) and ζ = 2.0 Under Harmonic Tip Load Measured by D_T and D_B for the First Mode Response

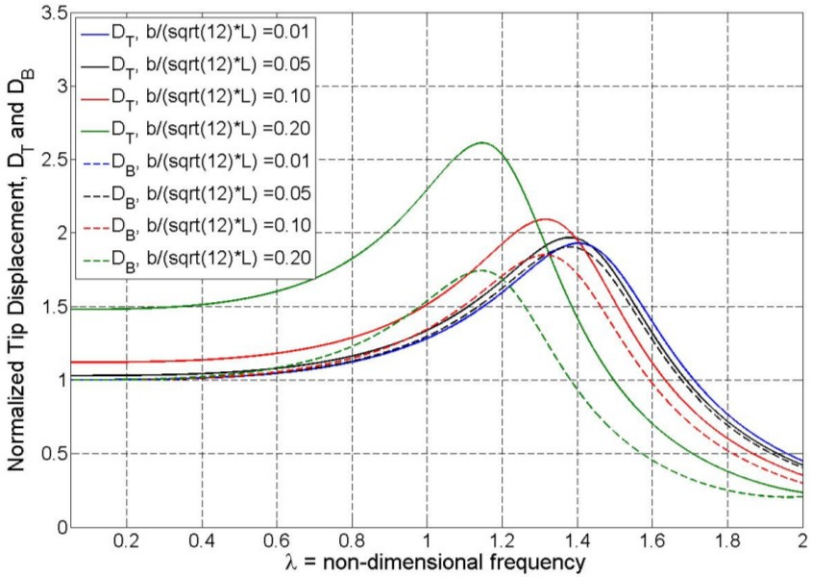

Figure 4-7: Frequency Response Curves of Normalized Tip Displacement of Various Geometries, $r = b/\left(L\sqrt{12}\right)$ for $\sqrt{E/kG} = 2$ and $\zeta = 2$ Under Harmonic Tip Load Measured by D_T and D_B for the First Mode Response

peaks of the normalized response curves of the tip displacement. The effects of the material ($\sqrt{E/kG}$), geometry (b/L) and fluid resistance (ζ) on the normalized resonant frequency are

shown in Fig. 4-8. The trend for the frequency over the range $\sqrt{E/kG} \in [0,3]$ and $b/L \in [0,0.69]$ (or, equivalently, $r \in [0,0.2]$) covers the range of common materials and those geometries most likely to necessitate application of Timoshenko beam theory. (Note that for pure silicon $\sqrt{E/kG} \approx 2$, assuming the orthotropic values of a standard (100) silicon wafer oriented with primary axis along [110]: E = 169 GPa, G = 50.9 GPa [Hopcroft et al., 2010] and k = 5/6 [Cowper, 1966; for case of Poisson's ratio of zero]). The fluid resistance parameter spans the

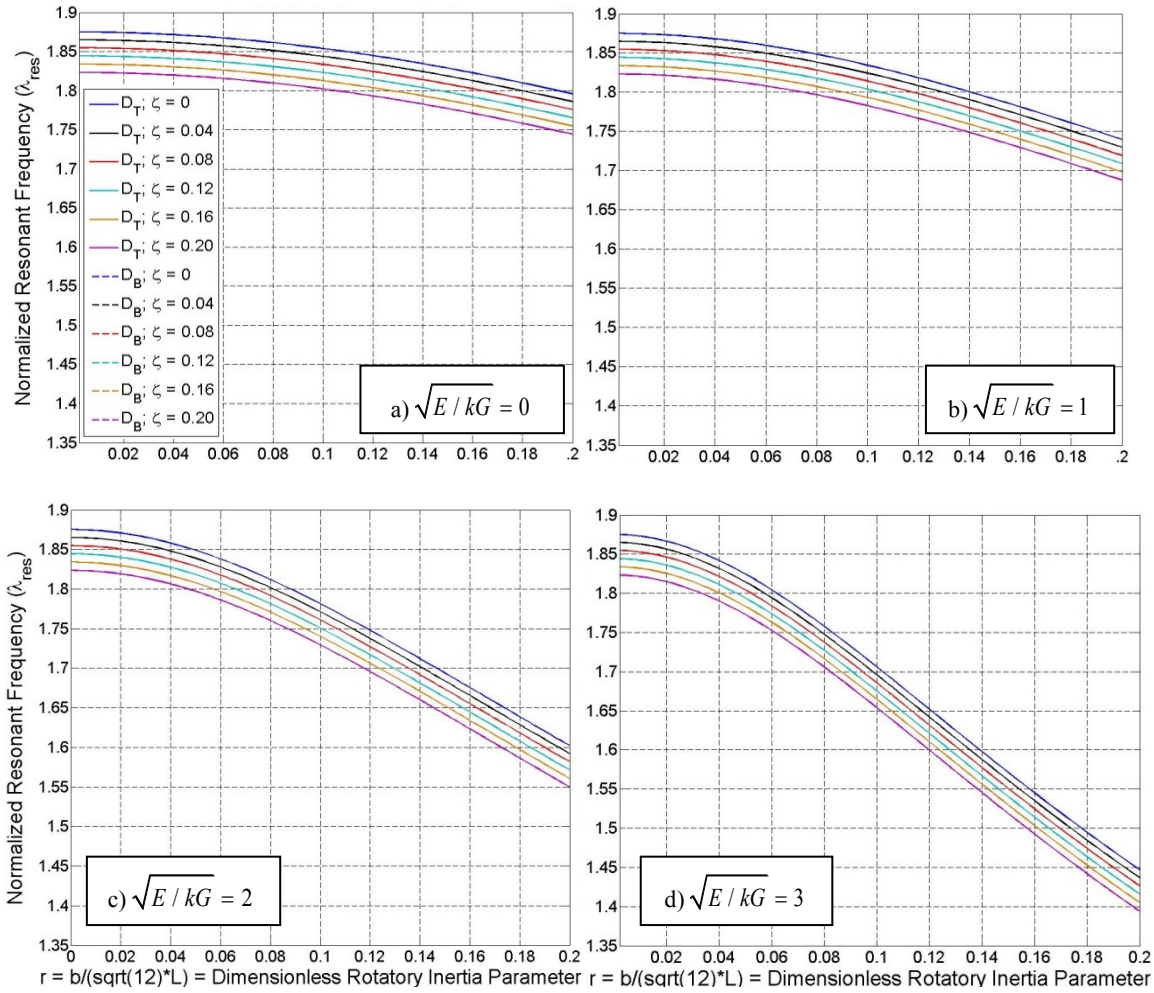

Figure 4-8: Resonant Frequency at Tip (ξ=1) for Various Fluid Resistance parameters (ζ), for $r = b/\left(L\sqrt{12}\right) \in [0,0.2]$ Measured by D_T and D_B: (a) $\sqrt{E/kG} = 0$, (b) $\sqrt{E/kG} = 1$, (c) $\sqrt{E/kG} = 2$, (d) $\sqrt{E/kG} = 3$

range $[0, 0.2]$, the lower limit being the in-vacuum case and the upper limit describing fluid resistance associated with geometries common in microcantilever-based devices [Heinrich et al., 2010b].

Figure 4-8 clearly illustrates several important trends: (1) a reduction in frequency due to an increase in fluid resistance (as expected, see [Heinrich et al., 2010a] for equivalent effect on Euler-Bernoulli beams in fluid) and Timoshenko parameters; and (2) essentially identical resonant frequency as measured by D_T and D_B. As noted earlier, the agreement between the total and bending signals in terms of resonant frequency indicates that the bending, shear and total response of the beam are all in-phase. In summary, over the practical range of Timoshenko and fluid parameters considered in Fig. 4-8, the maximum effect of r and $\sqrt{E/kG}$ on resonant frequency is to cause a reduction of approximately 23%.

As a verification of the normalized resonant frequency results, the value for the case $r = s = \zeta = 0$ in Fig.4-8a is $\lambda = 1.8751$, which is identical (to four decimal places) to the well-known eigenvalue provided by the in-vacuum case of Euler-Bernoulli beam theory.

Recall that the dramatic decrease in quality factor between the cases of in-vacuum or in-gas phase and the in-liquid counterpart served as the major impetus to investigate short, wide, lateral-mode microcantilevers for liquid-phase sensing. Therefore, in addition to resonant frequency results, the frequency response curves will also be used to extract the quality factor associated with viscous losses in the fluid. The quality factor may be defined in terms of the ratio of the maximum stored energy to the energy lost over a cycle of vibration. While there are several methods used to calculate the quality factor, all quality factor values displayed in subsequent figures are calculated using the 3-dB bandwidth method (also known as the bandwidth method). The 3-dB method permits one to estimate Q as the ratio of the resonant frequency to the 3-dB bandwidth of the resonant peak of the frequency response curve [e.g., Cox, 2011; Heinrich et al., 2010b]. The method is typically accurate for small-to-moderate levels of damping, i.e., for

damping ratios less than 20% or, equivalently, Q values greater than 2.5). Applying the 3-dB bandwidth method to the frequency response curves provides the quality factor for a range of fluid resistance and Timoshenko parameters. The quality factor for the harmonic support rotation is plotted in Fig. 4-9 for the range $\zeta \in [0,2]$ and in Fig. 4-10 for the range $\zeta \in [0,0.2]$.

Figure 4-9 shows the quality factor for $\zeta \in [0,2]$, $\sqrt{E/kG} = 1$ and $b/L = 0.45$ and highlights the increased quality factor obtained from the total displacement compared to that using the bending displacement at $\zeta > 0.2$. Note that for $\zeta > 0.2$ there is an increase in the difference between the quality factor as measured by the total and bending displacements; however, the resulting quality factors measured by the total and the bending displacements are essentially equal for small values of the fluid resistance parameter (e.g., $\zeta < 0.2$) that would be encountered in lateral-mode microcantilevers. Since Q is estimated by applying the 3-dB bandwidth method to both the D_T and D_B signals, one reason for the divergence of the quality factors at larger values of ζ may be the fact that, as noted earlier, this method loses accuracy for higher-loss systems (i.e., at larger values of ζ).

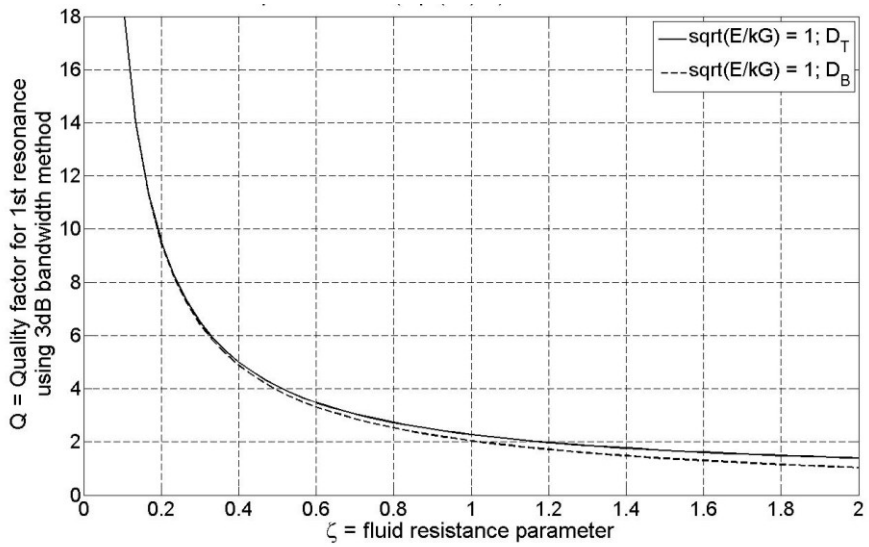

Figure 4-9: Quality Factor for Harmonic Tip Load Measured by D_T and D_B at 1st Resonance for $\sqrt{E/kG} = 1$, $b/L = 0.45$ ($r = 0.13$) and $\zeta \in (0,2)$

The impact of the Timoshenko and fluid resistance parameters on the quality factor is shown in Fig. 4-10 for various $\sqrt{E/kG}$ values and a fixed *b/L* value. (Note that similar trends apply for fixed $\sqrt{E/kG}$ and variable *b/L*, except that the effects are of lesser magnitude.) Figure 4-10a spans a common range of fluid resistance parameter that is applicable for most

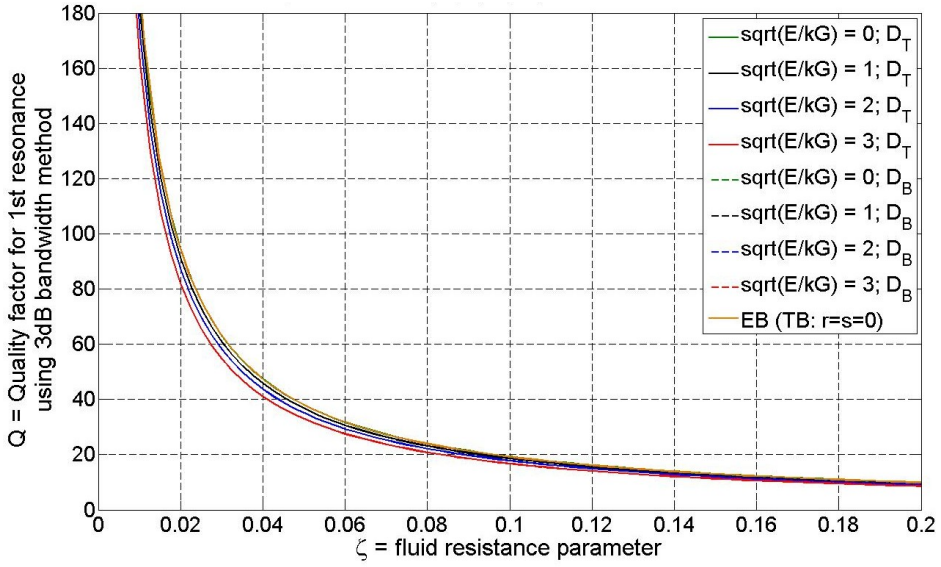

(a)

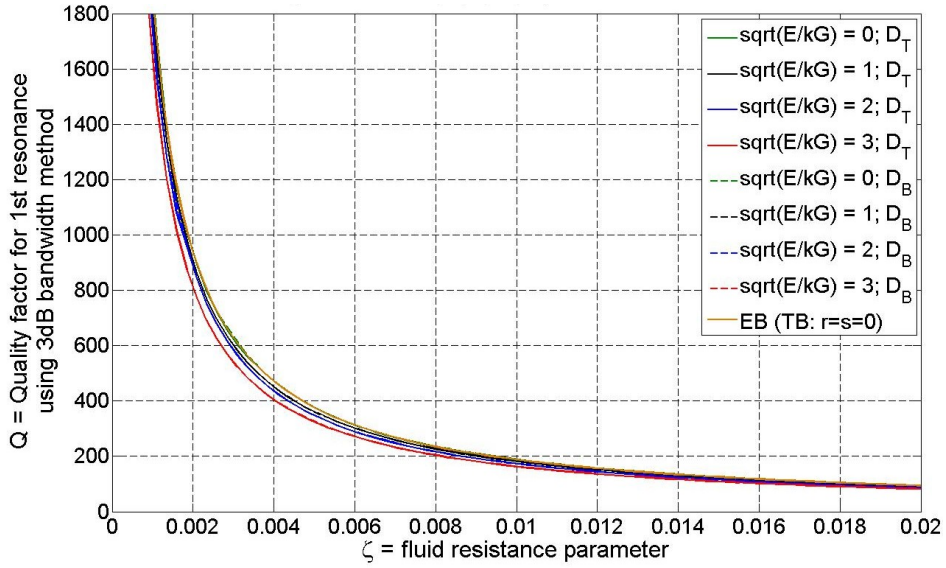

(b)

Figure 4-10: Quality Factor at First Resonance for Various Material Properties, $\sqrt{E/kG}$ for $b/\left(L\sqrt{12}\right) = 0.13$ as Measured by D_T and D_B: (a) $\zeta \in [0, 0.2]$ and (b) $\zeta \in [0, 0.02]$

microcantilevers in "water-like" fluids. Figure 4-10b provides a closer view of Q vs ζ for the lower range of fluid resistance parameter values. The trends in quality factor as a function of fluid resistance parameter are the same over all plotted values of ζ: for the particular value of b/L=0.45 considered, increasing the Timoshenko parameter, $\sqrt{E/kG}$, from 0 to 3 results in an approximately 15% reduction of the quality factor compared to the corresponding BE results (upper curves in Figs. 4-10a, b). The results of these figures also indicate that the quality factor values are essentially independent of the method of measurement (D_T or D_B).

Figure 4-11 shows the behavior of Q as a function of geometry (b/L) for fixed values of material $(\sqrt{E/kG})$ and fluid resistance (ζ) parameters. The effects of fluid resistance on the quality factor follow a particular trend: an increase in ζ results in a significant decrease in the quality factor, as indicated more explicitly in Fig. 4-10. The curves shown in Fig. 4-11a-c have very small slopes at low r for all values of $\sqrt{E/kG}$, but increasingly negative slopes with increasing r values. This indicates that the effects of r become increasingly significant for larger values of both r and $\sqrt{E/kG}$. From Fig. 4-11, it is also observed that increasing $\sqrt{E/kG}$ results in a reduction in the quality factor as discussed earlier. Again, it is observed that the value of Q does not depend on the output signal (D_T or D_B). Increases in both Timoshenko parameters (r and $\sqrt{E/kG}$) result in a reduction in Q compared to that predicted by EB theory. For a constant value of $\sqrt{E/kG}$, the effect of r is relatively constant over the range of ζ considered. For example, when $\sqrt{E/kG}$ = 1 (Fig 4-11a), changes in r over the range (0, 0.2) result in a ~7% reduction in Q regardless of the value of the fluid resistance parameter. Similarly, when $\sqrt{E/kG}$ = 2 (Fig 4-11b), increasing r over the specified range results in a ~14% reduction in Q and if $\sqrt{E/kG}$ = 3 (Fig 4-11c), the corresponding reduction in Q is 21-23%. Conversely, the trends in Q with respect to changes in $\sqrt{E/kG}$ may also be examined. For example, focusing on the most extreme value

of r=0.2 in the plots, the reduction in Q as $\sqrt{E/kG}$ is increased from 1 to 3 is ~16% for all values of ζ considered in the figures. In summary, over the practical range of Timoshenko and fluid parameters considered in Fig. 4-11, the maximum effect of r and $\sqrt{E/kG}$ on Q is to cause a reduction of approximately 23%. As was seen in the discussion of Fig. 4-10, it is expected that the dependence of Q on Timoshenko parameters will be relatively insensitive to the value of ζ. Thus, the effect of Timoshenko parameters on quality factor is expected to the similar for fluid resistance less than the minimum value of ζ =0.05 considered in Fig. 4-11.

The time-dependent vibrational shapes for the total, bending and shear displacement are presented in Fig. 4-12. The beam response is scaled by the respective components of the tip deflection and plotted for the following values: $b/L = 0.45$, $\sqrt{E/kG} = 2$, $\zeta = (0.05)$ and λ =1.6774. (The latter value represents a driving frequency slightly below the resonant value of 1.7178

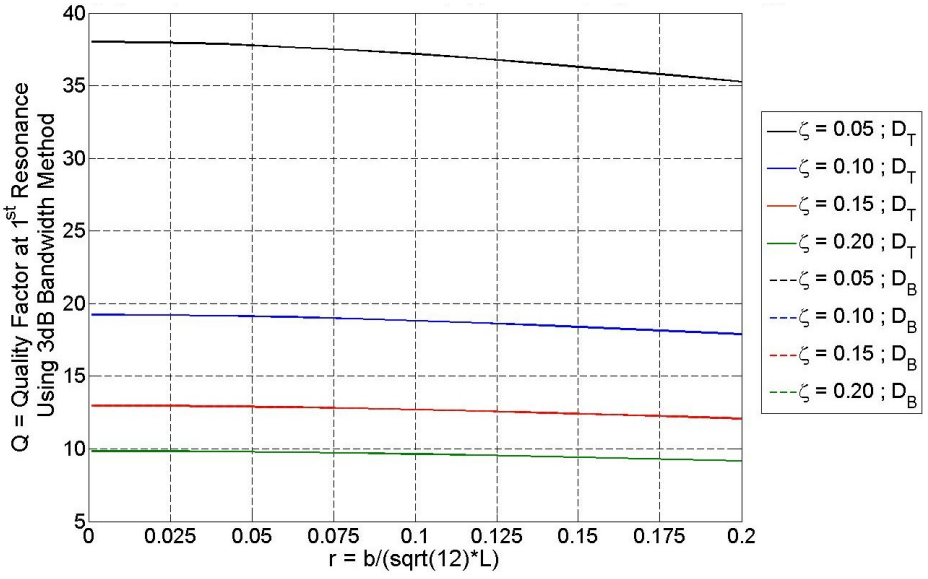

(a) $\sqrt{E/kG} = 1$

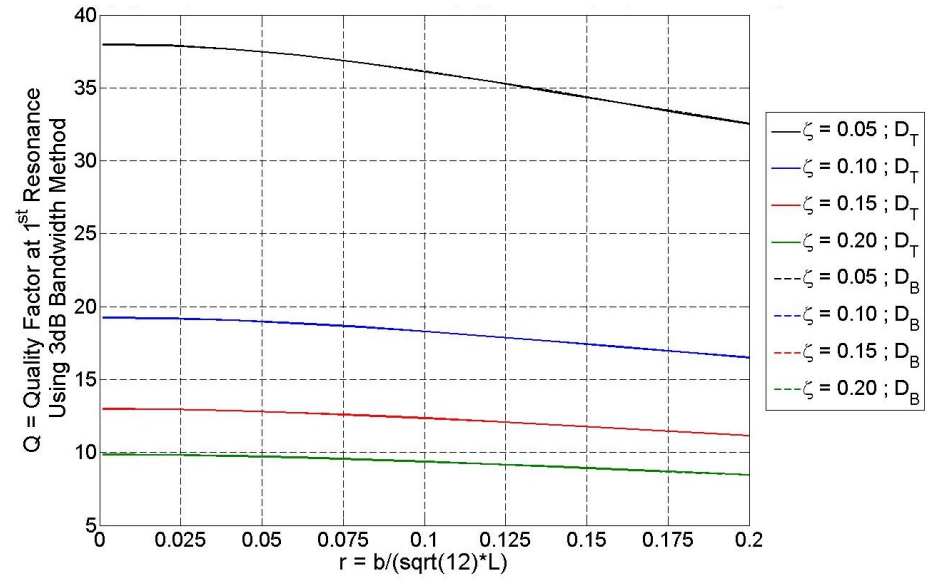

(b) $\sqrt{E/kG} = 2$

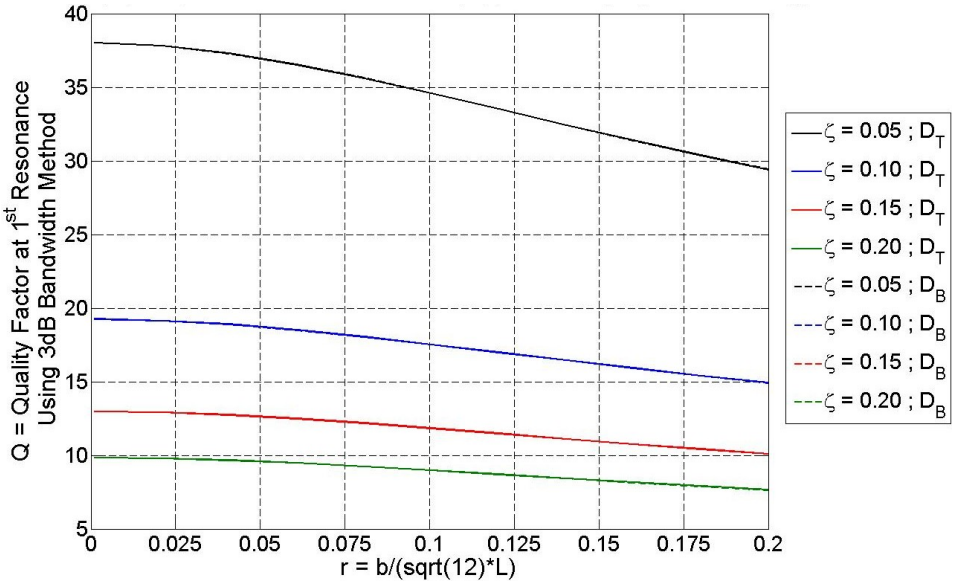

(c) $\sqrt{E/kG} = 3$

Figure 4-11: Quality Factor at First Resonance for Various Fluid Resistance Parameters, ζ, for $b/L \in [0, 0.69]$ ($r \in [0, 0.2]$), Under Harmonic Tip Load as Measured by D_T and D_B: (a) $\sqrt{E/kG} = 1$ (b) $\sqrt{E/kG} = 2$ (c) $\sqrt{E/kG} = 3$

for this case.) The resulting envelopes in Fig. 4-12 represent the maximum range of displacements of the vibrational shapes over a complete cycle. While the scaled beam shape does not remain constant throughout a cycle of steady-state vibration, the envelopes of the vibrational

shapes provided by the model are relatively tight and suggest that for the low values of fluid resistance parameter corresponding to lateral-mode beams with "Timoshenko geometries," it may be beneficial to develop a SDOF model using the time-independent, in-vacuum mode shape for a Timoshenko beam. These eigenfunctions were summarized in Sect. 3.2 and plotted in Sect. 4.2. For the case considered in Fig. 4-12, it has been confirmed graphically (not shown here) that these eigenfunctions are very good approximations to the forced vibration shapes plotted in the figure. Thus, the system behavior in the vicinity of a resonant peak is expected to be adequately estimated by a SDOF model based on an assumed shape given by the TB mode shape.

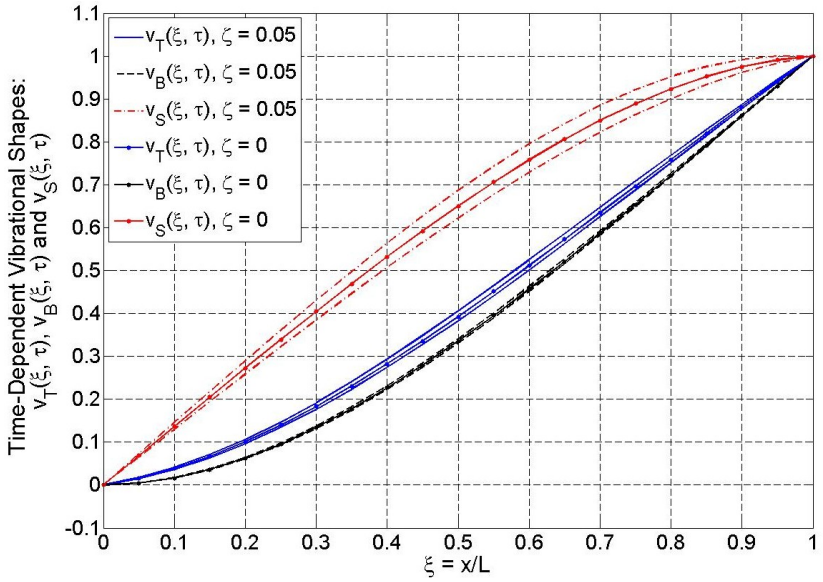

Figure 4-12: Vibrational Shapes $v_T(\xi,\tau), v_B(\xi,\tau),$ and $v_S(\xi,\tau)$ at Resonance Due to Harmonic Tip Force for λ = 1.6774 ζ = 0.05, *b/L* = 0.45 (*r* = 0.13) and $\sqrt{E/kG} = 2$

4.4 Parametric Study: In-Fluid Lateral Vibration of a Thin Microcantilever Due to a Harmonic Support Rotation

Section 4.4 presents the same results (frequency response curves for tip displacements, resonant frequencies, quality factors and vibrational shapes) as the preceding section for the beam response due to a harmonic support rotation. It is desirable to investigate and compare the results of the harmonic support rotation case to those for the harmonic tip force loading because, as

noted earlier, these are two common types of actuation used in cantilever-based sensors. Since common excitation methods are most effective for the first (most flexible) lateral mode, this section focuses on the results for the fundamental lateral mode of vibration for a microcantilever in a viscous fluid due to a harmonic support rotation. The subsequent results and figures are presented in the same order as in Sect. 4.3. Again, the results are presented using the Timoshenko parameters, where r is proportional to b/L (i.e., geometry) and s is related to r via $\sqrt{E/kG}$ (i.e., a material parameter). While this section presents results in terms of the total, bending, and shear displacements, note that the bending results in this section are the displacements associated with the bending *deformation* (i.e., the Timoshenko bending displacement minus the rigid body motion, as detailed in Sect. 1.5).

The frequency response curves in Fig. 4-13 display the normalized tip displacement for a range of excitation frequencies in terms of the amplitudes of the total displacement, D_T, the bending-deformation displacement, D_{B-D}, and the shear displacement, D_S. The plots in Fig. 4-13a-c display the frequency response curves for the specific values of $b/L = 0.45$ ($r = 0.13$) and $\zeta = 0.05$ for various values of $\sqrt{E/kG}$. While the reduction in tip response amplitudes is still evident between the first and subsequent modes (as shown in Fig. 4-13a and as noted previously for the case of tip force loading), the magnitude of this reduction for the case of a harmonic support rotation is much less than what occurs for the harmonic tip force case. (Compare Figs. 4-5a and 4-13a.) Consequently, while the harmonic tip load model provides similar results for total displacement amplitudes and resonant frequencies at the first mode, the models have significant differences in the magnitude of the tip displacement amplitude at the second (and possibly higher) modes. Therefore, this may be an indication that electrothermal excitation methods employed near the support may have inherent advantages over tip force (e.g., electromagnetic) actuation methods if lateral modes higher than the fundamental lateral mode are to be implemented.

The results for the first-mode frequency response shown in Fig. 4-13b display a reduction in both the resonant frequency and the amplitude of the resonant total tip displacement as the Timoshenko beam parameter (typified by $\sqrt{E/kG}$) is increased. This trend is exhibited for the resonant frequency regardless of whether obtained from D_T, $D_{B\text{-}D}$ or D_S. The bending-deformation displacement registers a slightly higher resonant frequency than the total displacement as shown in Fig. 4-13b, c. (Note that the frequency difference is small in these figures; for clearer examples at mode 1 see Figs. 4-14 and 4-15.). The increased resonant frequency obtained from $D_{B\text{-}D}$ is most likely due to that fact that the rigid motion from the applied load is out-of-phase with the beam's bending-deformation response.

Figure 4-13 shows the "switching" behavior of the displacement amplitudes for the support rotation case, previously noted for the harmonic tip load case: $D_T > D_{B\text{-}D}$ for the first mode, while $D_T < D_{B\text{-}D}$ for the second mode. As for the previous load case, this observation suggests that for higher values of Timoshenko and fluid resistance parameters, the bending-deformation displacement at the second mode will have greater displacement amplitudes than the total displacement; consequently, devices that utilize detection methods that monitor bending strain directly for mode 2 may have some sensing advantages.

It is important to note that Fig. 4-13 shows that, for the first mode of lateral vibration due to a harmonic support rotation, the three components of tip displacement at or near resonance are out-of-phase with each other, unlike in the harmonic tip load case for which they were completely in-phase. Consequently, the total bending displacement, shear displacement, bending-deformation displacement and rigid rotation do not reach their maxima at the same time and therefore exhibit different resonant (i.e., peak signal) frequencies. This behavior is less obvious at the low ζ value considered in Fig. 4-13 than at higher ζ values as shown in Figs. 4-14 and 4-15. In Fig. 4-14, the frequency response curves for the normalized tip displacements (total, bending- deformation and

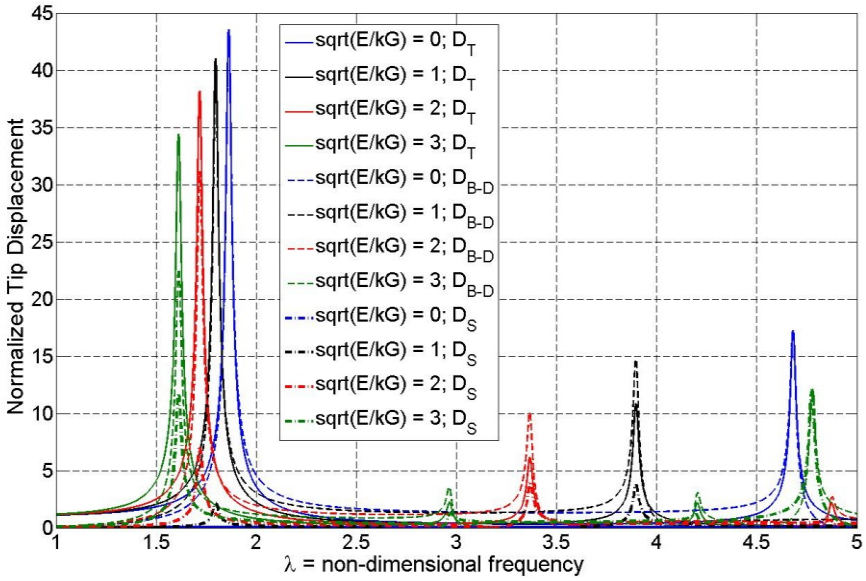
Normalized Tip Displacement
λ = non-dimensional frequency
sqrt(E/kG) = 0; D_T
sqrt(E/kG) = 1; D_T
sqrt(E/kG) = 2; D_T
sqrt(E/kG) = 3; D_T
sqrt(E/kG) = 0; D_B-D
sqrt(E/kG) = 1; D_B-D
sqrt(E/kG) = 2; D_B-D
sqrt(E/kG) = 3; D_B-D
sqrt(E/kG) = 0; D_S
sqrt(E/kG) = 1; D_S
sqrt(E/kG) = 2; D_S
sqrt(E/kG) = 3; D_S

(a)

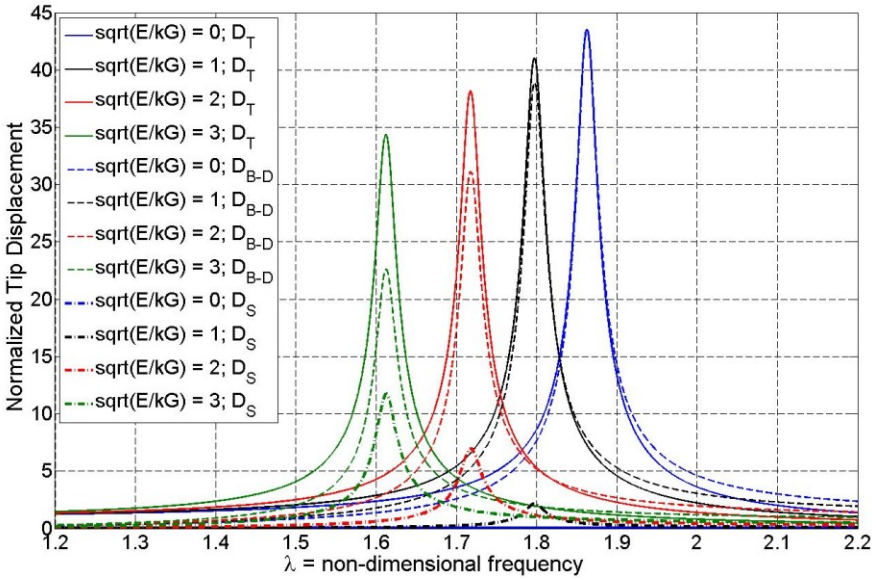
Normalized Tip Displacement
λ = non-dimensional frequency
sqrt(E/kG) = 0; D_T
sqrt(E/kG) = 1; D_T
sqrt(E/kG) = 2; D_T
sqrt(E/kG) = 3; D_T
sqrt(E/kG) = 0; D_B-D
sqrt(E/kG) = 1; D_B-D
sqrt(E/kG) = 2; D_B-D
sqrt(E/kG) = 3; D_B-D
sqrt(E/kG) = 0; D_S
sqrt(E/kG) = 1; D_S
sqrt(E/kG) = 2; D_S
sqrt(E/kG) = 3; D_S

(b)

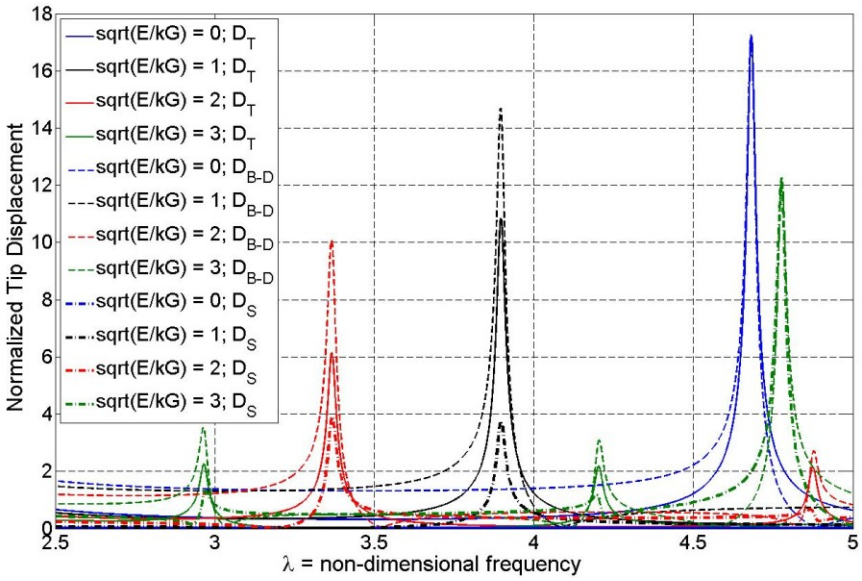

(c)

Figure 4-13: Frequency Response Curves of Normalized Tip Displacement for Various Material Properties, $\sqrt{E/kG}$, for *b/L* = 0.45 (*r* = 0.13) and ζ = 0.05 Under Harmonic Support Rotation as Measured by D_T, D_B and D_S: (a) $\lambda \in [1,5]$ (b) First Mode Response, $\lambda \in [1.2, 2.2]$ (c) Second Mode Response, $\lambda \in [2.5, 5]$

shear) are shown for $\zeta = 2.0$, $b/L = 0.45$ ($r = 0.13$), and $\sqrt{E/kG} = (0,1,2,3)$. Similarly, Fig. 4-15 provides the frequency response curves for the normalized tip displacements for $\zeta = 2.0$, $\sqrt{E/kG} = 2$ and various values of b/L. As the excitation frequency approaches zero (i.e., quasi-static) the total displacement approaches one, while the displacements due to bending deformation and shear deformation approach zero. This intuitively makes sense because a statically imposed support rotation will cause only a rigid-body rotation that will not result in any bending or shear deformation. Increases in the values of the Timoshenko parameters in Figs. 4-14 and 4-15 have similar qualitative effects on both the resonant amplitudes and resonant frequencies as measured by total, bending-deformation, and shear displacements. The latter is due to the fact that an increase in the Timoshenko parameter values will result in a more flexible, higher-mass beam with a correspondingly reduced resonant frequency.

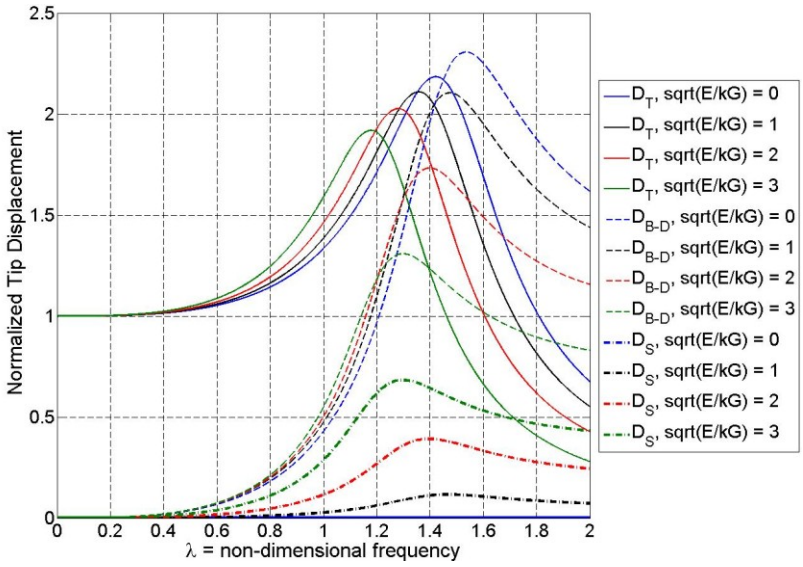

Figure 4-14: Frequency Response Curves of Normalized Tip Displacement of Various Material Properties, $\sqrt{E/kG}$ for b/L = 0.45 (r = 0.13) and ζ = 2.0 Under Harmonic Support Rotation Measured by D_T , $D_{B\text{-}D}$ and D_S for the First Mode Response

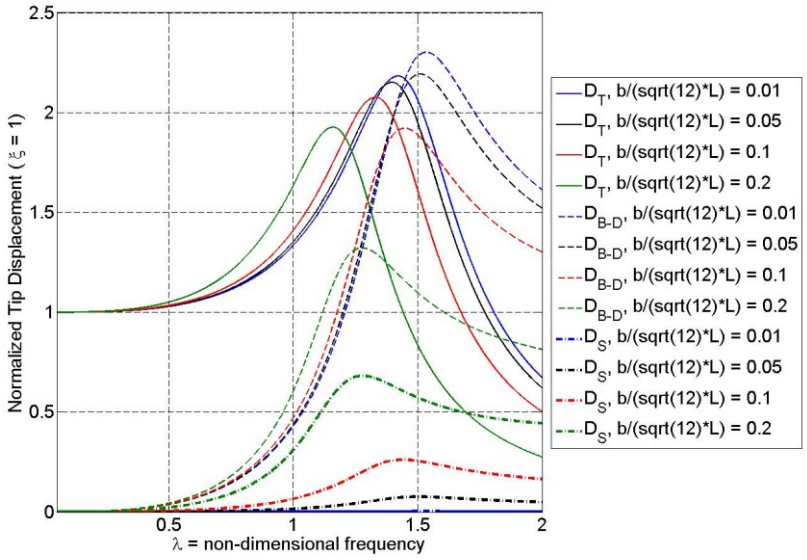

Figure 4-15: Frequency Response Curves of Normalized Tip Displacement of Various Geometries, $r = b/\left(L\sqrt{12}\right)$ for $\sqrt{E/kG} = 2$ and ζ = 2 Under Harmonic Support Rotation Measured by D_T , $D_{B\text{-}D}$ and D_S for the First Mode Response

The resonant frequencies for the case of a harmonic support rotation are plotted against r in Fig. 4-16 for four different values of $\sqrt{E/kG}$ and for several values of the fluid resistance parameter. The plots cover the same range of Timoshenko and fluid resistance parameters as the plots presented in Sect. 4.3 for the previous load case. While the overall trends in resonant frequency with respect to Timoshenko and fluid resistance parameters are similar to those associated with the harmonic tip force case, there is a slight, but noticeable, difference in the resonant frequency obtained using the bending-deformation displacement compared to the total displacement in the present case. Since all components of the beam response (total, bending and shear) are in-phase for the case of the harmonic tip load, the measured resonant frequency is the same regardless of the method of measurement. However, for the case of the harmonic support rotation, the components of the beam response (total, bending-deformation, and shear) are out-of-phase with the support rotation (and, thus, with the associated rigid-body displacement). As a result, for the range of ζ considered in Fig. 4-16, the resonant frequency determined via the bending deformation is slightly greater than that based on the total beam displacement for the first mode, and the difference increases as ζ increases. For example, as seen in Figs. 4-14 and 4-15, the difference in the two resonant frequency values is on the order of 10-15% when ζ =2. Note that this behavior (bending-deformation signal giving a higher resonant frequency than the total displacement signal) is reversed at the second mode (not shown here) due to the switching of the relative sizes of the total and bending-deformation displacement amplitudes as discussed in the previous section.

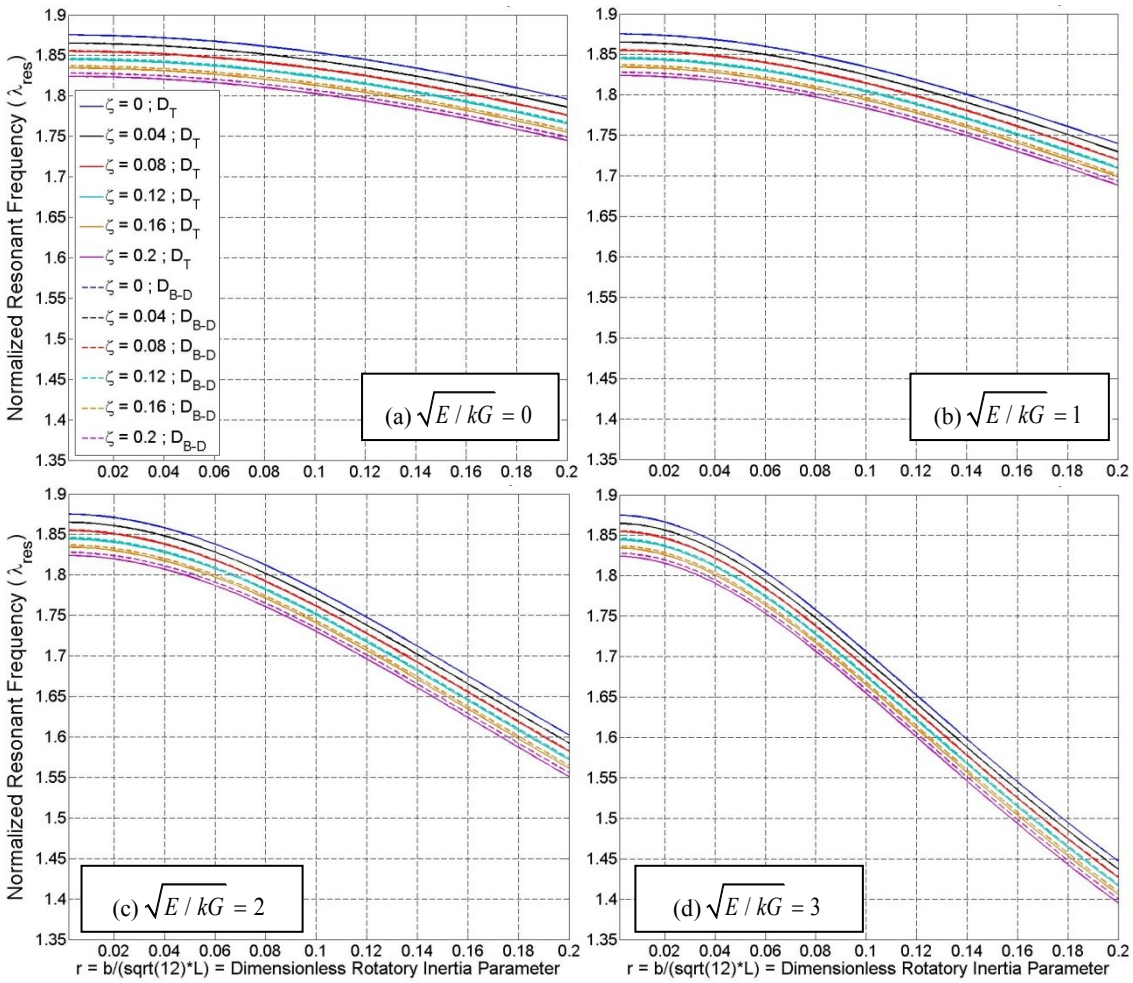

Figure 4-16: Resonant Frequency at Tip (ξ=1) for Various Fluid Resistance parameters (ζ), for $r = b/\left(L\sqrt{12}\right) \in [0, 0.2]$ Measured by D_T and $D_{B\text{-}D}$: (a) $\sqrt{E/kG} = 0$, (b) $\sqrt{E/kG} = 1$, (c) $\sqrt{E/kG} = 2$, (d) $\sqrt{E/kG} = 3$

The normalized frequency results that are presented in Fig. 4-16 may be checked by comparison to the in-vacuum, Euler-Bernoulli result. Indeed, the resonant frequency for $r = s = \zeta = 0$ from Fig.4-16a, $\lambda_{res} = 1.8751$, is identical (within the specified accuracy of four decimal places) to the well-known eigenvalue provided by the in-vacuum case of Euler-Bernoulli beam theory.

Applying the 3-dB bandwidth method to the theoretical frequency response curves, one may obtain the quality factor for a range of fluid resistance and Timoshenko parameters. For

example, the quality factor for the harmonic support rotation load case is plotted in Fig. 4-17 for the range $\zeta \in [0,2]$ and in Fig. 4-18 for the range $\zeta \in [0,0.2]$.

Figure 4-17 shows the quality factor for $\zeta \in [0,2]$, $\sqrt{E/kG} = 1$ and $b/L = 0.45$ and highlights the increased quality factor obtained from the total displacement compared to that using the bending-deformation displacement at $\zeta > 0.2$. Note that for $\zeta > 0.2$ there is an increase in the difference between the quality factor as measured by the total and bending-deformation displacements; however, the resulting quality factors measured by the total and the bending-deformation displacements are virtually identical for small values of the fluid resistance parameter (e.g., $\zeta < 0.2$) that would be typical of many lateral-mode microcantilevers. Note that the Q values plotted in Fig.4-17 are obtained using the 3-dB bandwith method which is valid for estimating Q at small values of ζ, so that the divergence of the two Q curves (corresponding to D_T and $D_{B\text{-}D}$) may be due to the larger values of ζ exceeding the "low-loss" limitation of the 3-dB method. (A similar comment was made for the case of a harmonic tip force; c.f. Fig. 4-9.) Also, note that Q is expected to be a function of resonant frequency and that the resonant frequency

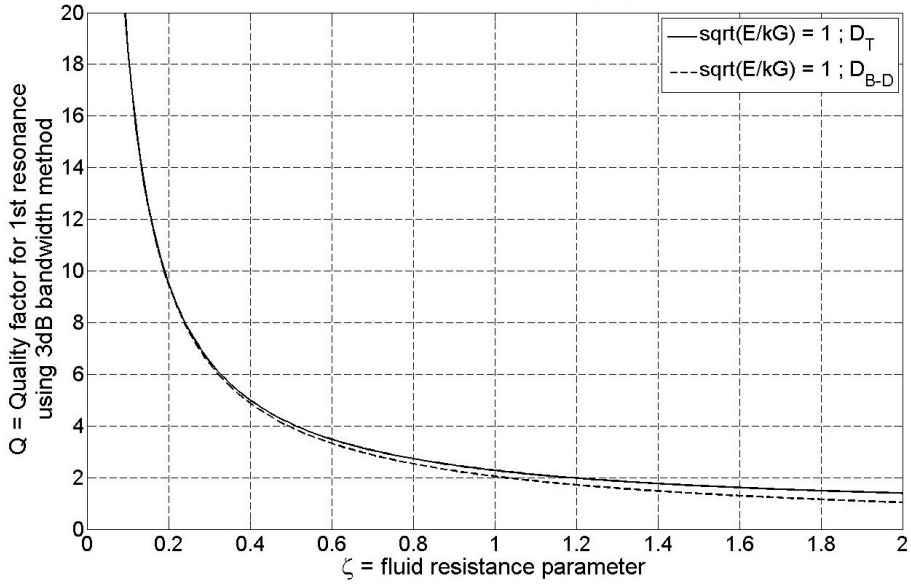

Figure 4-17: Quality Factor for Harmonic Support Rotation Measured by D_T and $D_{B\text{-}D}$ at 1st Resonance for $\sqrt{E/kG} = 1$, $b/L = 0.45$ ($r = 0.13$) and $\zeta \in (0,2)$

based on $D_{B\text{-}D}$ is slightly higher than that of D_T (c.f. Fig. 4-16), which may also contribute to a difference in the two quality factor curves shown in Fig. 4-17 at larger values of the fluid resistance parameter.

Figure 4-18 shows the quality factor for the range of $\zeta \in [0, 0.2]$ and displays the effects of the Timoshenko and fluid resistance parameters on the quality factor for various $\sqrt{E/kG}$ values and a fixed value of *b/L*=0.45. (As was noted in Sect. 4.3 and is applicable here as well, similar trends apply for fixed $\sqrt{E/kG}$ and variable *b/L*, except that the effects are of lesser magnitude.) Note that the range of the fluid resistance parameter in Fig. 4-18a is applicable for most microcantilevers in "water-like" fluids, while Fig. 4-18b provides a closer view of *Q* vs. ζ for the lower range of fluid resistance parameters. The trends in quality factor as a function of fluid resistance parameter are the same over all plotted values of ζ: for the particular value of *b/L*=0.45 considered, increasing the Timoshenko parameter, $\sqrt{E/kG}$, from 0 to 3 results in an approximately 15% reduction of the quality factor compared to the corresponding BE results (upper curves in Figs. 4-18a, b). The results of these figures also indicate that the quality factor values are essentially independent of the method of measurement (D_T or D_B) for the range of fluid resistance parameter considered. Note that, despite the difference between the quality factor as measured by D_T and $D_{B\text{-}D}$ at ζ > 0.2, the trends for the quality factor of a harmonic support rotation are essentially the same as those for the quality factor as determined from the response due to a harmonic tip load (presented in Sect. 4-3 in Figs. 4-9 and 4-10). There is a strong impact of the fluid resistance parameter on the quality factor, while changes in the Timoshenko parameters (typified in Fig. 4-18 by different values of $\sqrt{E/kG}$) affect the quality factor to a much smaller degree.

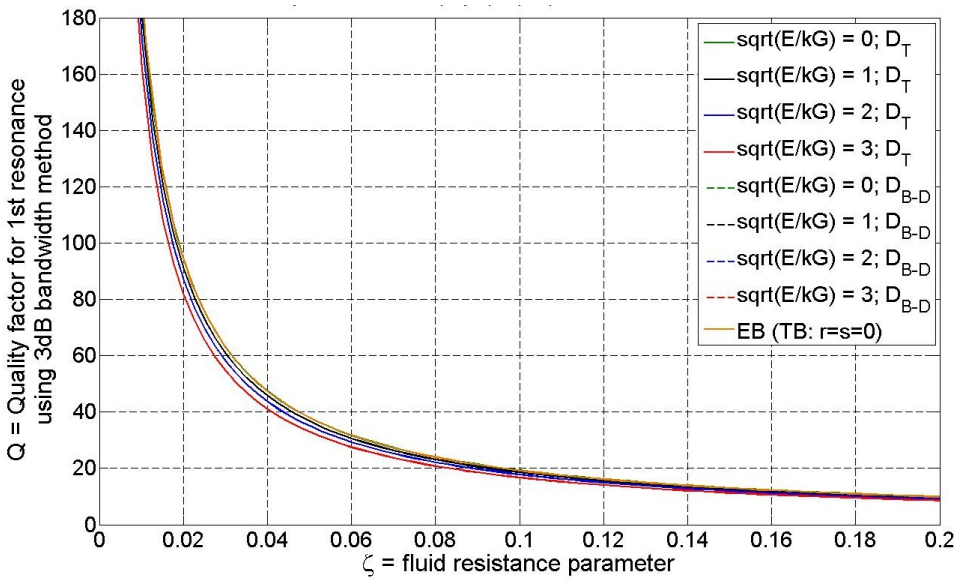

(a)

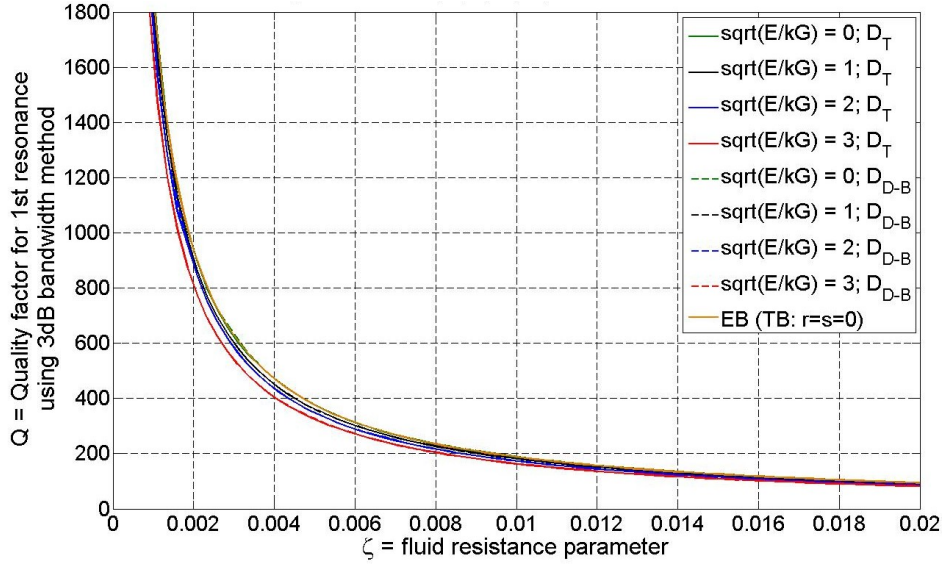

(b)

Figure 4-18: Quality Factor at First Resonance for Various Material Properties, $\sqrt{E/kG}$ for $b/\left(L\sqrt{12}\right) = 0.13$ as Measured by D_T and $D_{B\text{-}D}$: (a) $\zeta \in [0, 0.2]$ and (b) $\zeta \in [0, 0.02]$

Figure 4-19 displays the quality factor as a function of geometry (parameter *r*) for fixed values of the material parameter ($\sqrt{E/kG}$) and the fluid resistance parameter (ζ). Again, the effects of the fluid resistance parameter on the quality factor are seen to be significant.

Comparing Fig. 4-19 with Fig. 4-11 shows the agreement between the quality factors for different types of loading for $\zeta < 0.2$; therefore, the previous discussion of Fig. 4-11 is also applicable to Fig. 4-19 and will not be repeated here. For higher values of the fluid resistance parameter ($\zeta > 0.2$), the quality factor obtained for the support rotation load case via $D_{B\text{-}D}$ is lower than the quality factor based on D_T (see Fig. 4-17) and it is also lower than the value based on the tip-force load case. While notable, the common values of fluid resistance parameter usually associated with microcantilever-based sensors are in the range $\zeta \in (0, 0.2)$ where the difference remains negligible (i.e., <1%). (Recall that a similar conclusion was made for the case of the harmonic tip load.)

The time-dependent vibrational shapes for the total, bending-deformation, and shear displacement are presented in Fig. 4-20. The beam response is scaled by the respective components of tip deflection and plotted for the values $b/L = 0.45$, $\sqrt{E/kG} = 2$, $\zeta = 0.2$ and $\lambda = 1.6774$ (slightly below the fundamental lateral resonant frequency). The envelopes displayed in

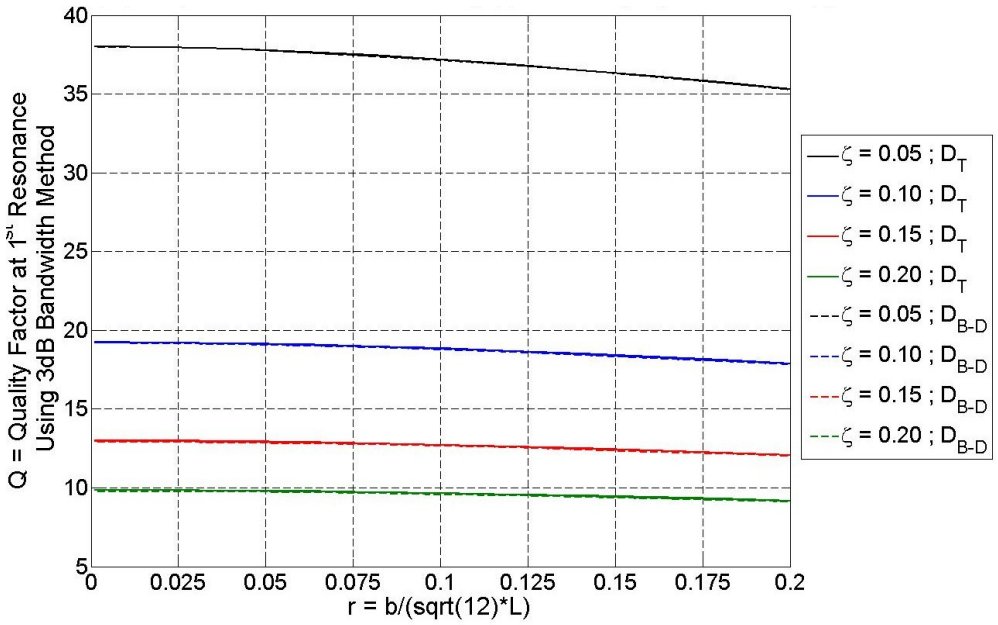

(a) $\sqrt{E/kG} = 1$

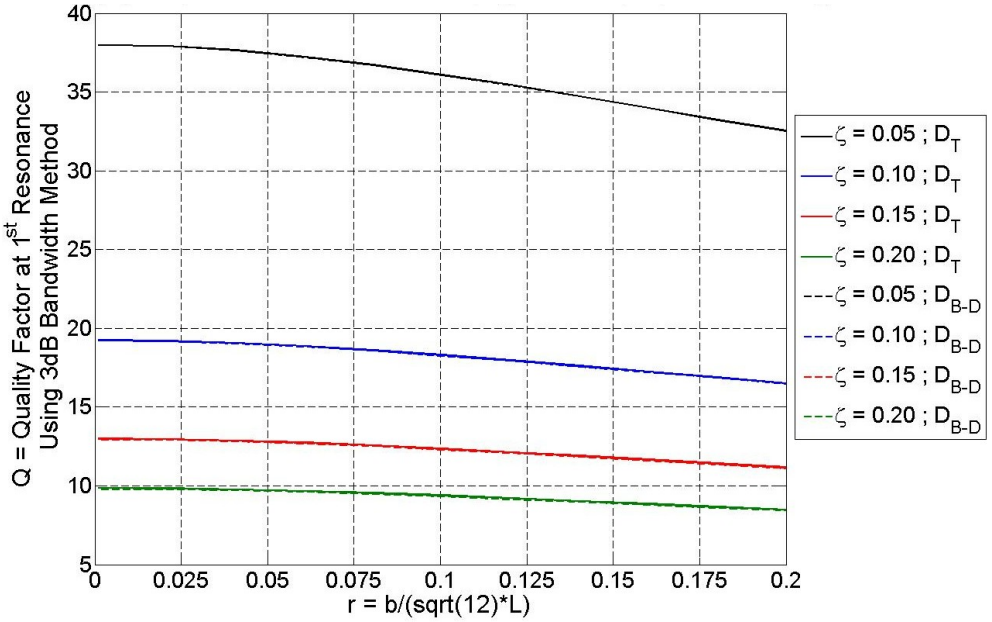

(b) $\sqrt{E/kG} = 2$

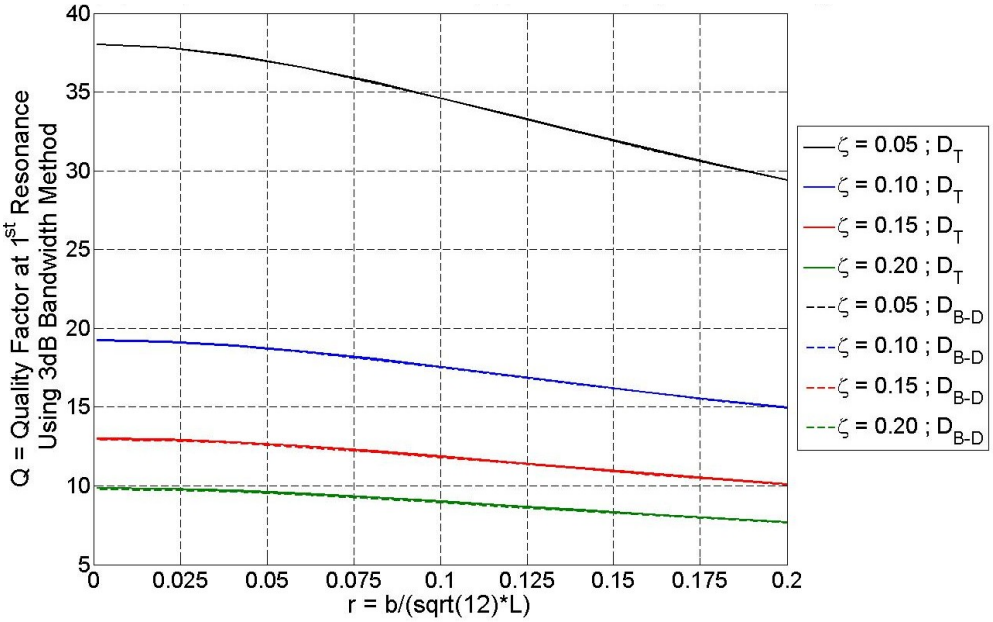

(c) $\sqrt{E/kG} = 3$

Figure 4-19: Quality Factor at First Resonance for Various Fluid Resistance Parameters, ζ, for $b/L \in [0, 0.69]$ ($r \in [0, 0.2]$), Under Harmonic Support Rotation as Measured by D_T and $D_{B\text{-}D}$: (a) $\sqrt{E/kG} = 1$ (b) $\sqrt{E/kG} = 2$ (c) $\sqrt{E/kG} = 2$

Fig. 4-20 represent the maximum displacement range of the vibrational shapes over a complete vibration cycle. These envelopes are relatively tight (as was seen for the previous load case), again suggesting that for small values of the fluid resistance parameter applicable to beams with "Timoshenko geometries," it may be beneficial to develop a SDOF model using in-vacuum, TB mode shape as the assumed shape function. .

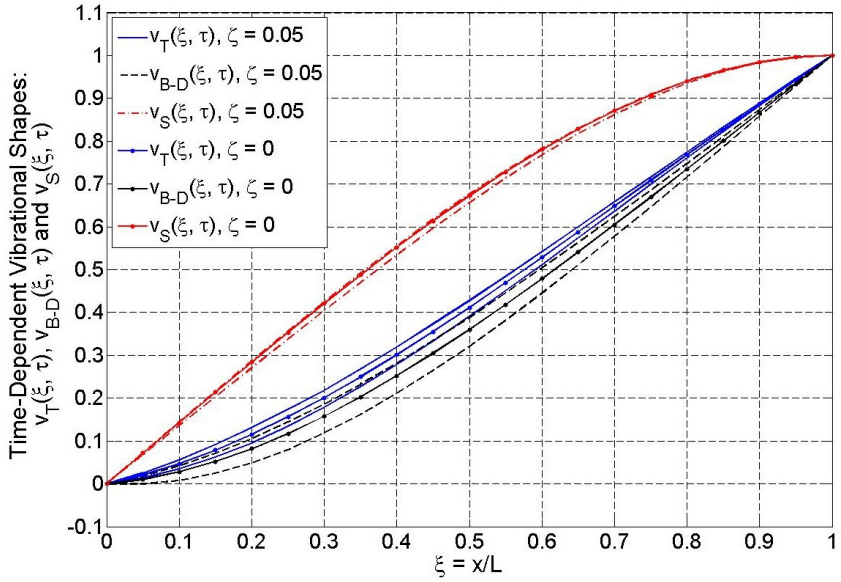

Figure 4-20: Vibrational Shapes $v_T(\xi,\tau), v_{B\text{-}D}(\xi,\tau)$, and $v_S(\xi,\tau)$ Due to Harmonic Support Rotation for λ = 1.6674, ζ = 0.05, *b/L* = 0.45 (*r* = 0.13) and $\sqrt{E/kG} = 2$

4.5 Comparison of Results from Harmonic Tip Load and Harmonic Support Rotation Cases

This section summarizes the similarities and differences in the results of the harmonic tip force and the harmonic support rotation load cases. Comparisons for beam response, resonant frequency and quality factor are as follows:

1. In both loading cases increasing the Timoshenko parameters (e.g., $\sqrt{E/kG}$) results in a reduction of the resonant frequency as determined according to the total displacement,

bending/bending-deformation, and shear displacement for all modes considered. (Figs. 4-5 and 4-13)

2. Increasing $\sqrt{E/kG}$ in the case of harmonic tip force loading causes an increase in the amplitude of the total tip displacement, while for the harmonic support rotation case the total tip displacement amplitude decreases with increasing $\sqrt{E/kG}$. However, if one considers the amplitude of the bending/bending-deformation tip displacement, both amplitudes decrease with increasing values of $\sqrt{E/kG}$. (See Figs. 4-6 and 4-14.) Similar conclusions apply with respect to changing the value of *r* (Figs. 4-7 and 4-15).
3. For the harmonic tip force case all methods of measuring the beam response (total, bending and shear displacements) appear to be in phase at the first resonant peak (Fig. 4-5b). For the second mode, the shear displacement appears to be 180° out of phase relative to the bending and total displacements, which remain in phase with each other (Fig. 4-5c). This differs from the various response components of the beam to the harmonic support rotation, which are out of phase at all modes examined, due to the rigid motion imposed by the support rotation (Figs. 4-13, 4-14 and 4-15).
4. Resonant frequency, as determined by the total displacement, is the same for both loading cases (Figs. 4-8 and 4-16). The resonant frequency for the harmonic tip load case is the same as determined by both the total displacement and bending displacement (Fig. 4-8). However, the resonant frequency for the harmonic support rotation case, as measured by the bending-deformation displacement, is slightly higher than that measured by the total displacement; moreover, this difference increases at higher values of the fluid resistance parameter (Fig. 4-16).
5. The quality factor is essentially the same regardless of loading type (harmonic tip force or harmonic support rotation) and regardless of the method of measurement (total or bending/bending-deformation displacement) for $\zeta < 0.2$ (Figs. 4-10, 4-11, 4-18, and 4-

19). For larger fluid resistance (i.e., $\zeta > 0.2$), Q based upon the total displacement is greater than that obtained using the bending-deformation displacement, regardless of the load case (Figs. 4-9 and 4-17). (E.g., for $\zeta = 0.2$, Q from D_T is ~1% greater than from $D_{B\text{-}D}$, while for $\zeta = 2$, Q from D_T is ~25% greater than that from $D_{B\text{-}D}$) for both load cases (Figs. 4-9 and 4-17).

4.6 Derivation of Analytical Expression for Quality Factor

Previous theoretical investigations of lateral-mode Euler-Bernoulli beams with Stokes-type fluid resistance [Heinrich et al., 2010a, b] have established an approximate analytical expression for the quality factor. That approximate expression indicated that the quality factor is of the form $Q \approx 1.8751/\zeta$, i.e., Q depends inversely on ζ. Moreover, the quality factor results for the in-fluid, Timoshenko model presented in Sects. 4.3 and 4.4, particularly those of Figs. 4-10 and 4-18, also indicate an approximately inversely proportional relationship between quality factor and the fluid resistance parameter, which is consistent with the earlier approximate results based on EB theory. Those same figures suggest that the dependence of the quality factor on the Timoshenko parameters is relatively simple. All of these observations provide motivation for pursuing a simplified analytical expression for the quality factor as a function of ζ and the Timoshenko parameters. Such an expression would be advantageous since it would provide quality factor results explicitly in terms of fundamental system parameters without resorting to the implementation of the relatively complicated solutions presented in Ch. 3 or interpolation of the graphical results of Ch. 4. Therefore, such an analytical expression will be derived in subsequent paragraphs. The application of this expression will be limited to the ranges of $\zeta =$ [0.01, 0.05], $r =$ [0, 0.2] and $e \equiv \sqrt{E/kG} = [0,3]$, since these ranges span most cases of practical interest.

To reflect the observed ζ-dependence the assumed form of the analytical expression for Q is taken as

$$Q \approx \frac{g(r,e)}{\zeta} \quad , \tag{4-3}$$

where the function $g(r,e)$ depends only on the Timoshenko parameters. Three conditions must be satisfied by Eq. (4-3): (1) for $r = 0$, Q should be independent of e (because $r = 0$ represents the EB limit by virtue of the fact that $s = re$); (2) $\partial Q/\partial r\big|_{r=0} = 0$; and (3) $\partial Q/\partial e\big|_{e=0} = 0$. Condition 2 is suggested by Figs. 4-11 and 4-19, as is Condition 3 by analogous plots (not included in the dissertation). It may be verified that the following form for Q meets these three conditions:

$$Q \approx \frac{a_0 - a_1 r^{a_2} - a_3 r^{a_4} e^{a_5}}{\zeta} \quad , \tag{4-4}$$

where the a_i, $i = 0, 1,..., 5$, are constants and a_2, a_4 and a_5 are all greater than 1. The value of a_0 is obtained by forcing Eq. (4-4) to agree with the "exact" Q results (see Sect. 4.4) for the case of $r = 0$ (i.e., the EB limit). This agreement is forced for a value of $\zeta = 0.03$, i.e., at the midpoint value of the range of interest, yielding $a_0 = 1.8903$. The values of the remaining constants are obtained by using Eq. (4-4) (with $a_0 = 1.8903$) to perform a least-squares surface fit (within MATLAB) of the exact quality factor results for $\zeta = 0.03$ as shown in Fig. 4-21. The resulting analytical expression for Q becomes

$$Q \approx \frac{1.8903 - 1.595 r^{1.902} - 0.6396 r^{1.422} e^{1.622}}{\zeta} \quad , \tag{4-5}$$

or, in terms of the fundamental system parameters (taking k=5/6),

$$Q \approx 0.7182 \frac{hb^{1/2}}{L} \left(\frac{E\rho_b^3}{\rho_f^2 \eta^2} \right)^{1/4} \left[1 - 0.0794 \left(\frac{b}{L} \right)^{1.902} - 0.0670 \left(\frac{b}{L} \right)^{1.422} \left(\frac{E}{G} \right)^{0.811} \right] . \tag{4-6}$$

Despite the fact that the constants in Eqs. (4-5) and (4-6) were derived for the case of $\zeta = 0.03$, the accuracy of the results over the practical range $\zeta = [0.01, 0.05]$ (and possibly beyond) is excellent. More specifically, the maximum percent difference between the analytical Q results and the exact results of the TB model (for Stokes-type fluid resistance) is only 2.6% (occurring at $\zeta = 0.05$, $r = 0.2$ and $e = 3$) over this entire range of ζ and over the ranges $r = [0, 0.2]$ and $e \equiv \sqrt{E/kG} = [0,3]$.

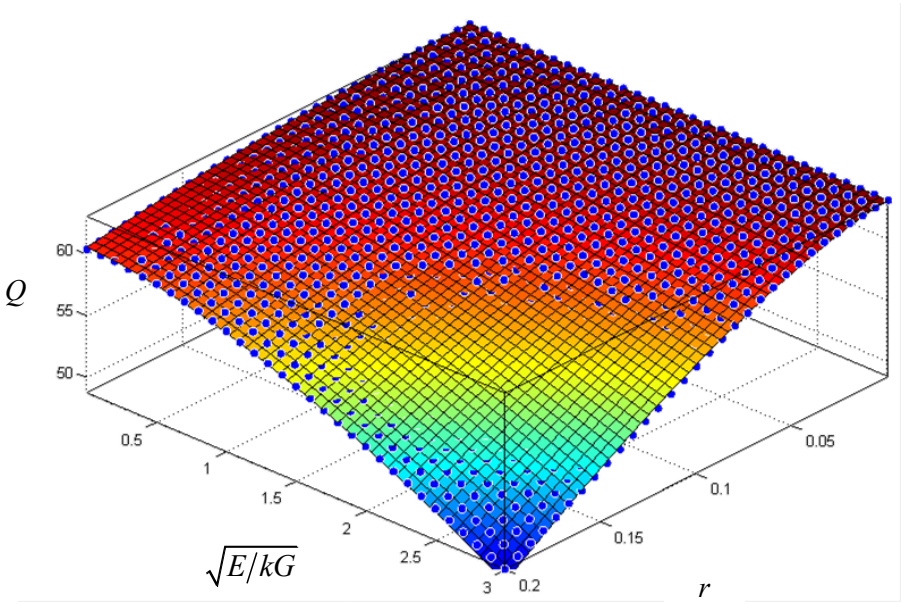

Figure 4-21: Plot of the Theoretical Quality Factor, Q, and the Best-Fit Surface for $\zeta = 0.03$ over the Ranges $\sqrt{E/kG} \in [0,3]$ and $r \in [0,0.2]$

4.7 Model Verification with Benchmark Solutions

This section provides numerical verification of the results presented in Sects. 4.3 and 4.4 by reduction of the in-fluid, forced vibration Timoshenko beam problem to in-vacuum and in-fluid Euler-Bernoulli equivalents for the purpose of comparison. As the initial confirmation on the resonant frequency results, the in-fluid, forced vibration of a Timoshenko beam is reduced to the well-known case of an in-vacuum, Euler-Bernoulli model. As further verification, the results (frequency and quality factor) are compared to recent published results of the forced vibration of

an Euler-Bernoulli beam with Stokes-type fluid resistance [Heinrich et al., 2010a, b]. Finally, the results of the current models for forced vibration of an in-fluid Timoshenko beam are compared to numerical solutions of the same case obtained via the MATLAB solver bvp4c.

4.7.1 Comparison of Resonant Frequency: Current Model and In-Vacuum, Euler-Bernoulli Model

Analogous to the analytical verification provided in Ch.2 (i.e., reduction to in-vacuum Euler-Bernoulli theory via elimination of the Timoshenko and fluid parameters), the results for both load types (harmonic tip force and harmonic support rotation) are compared to Euler-Bernoulli results for the limiting case of $r = s = \zeta = 0$ as shown in Sects. 4.3 and 4.4 using Figs. 4-8 and 4-15, respectively. At the in-vacuum, Euler-Bernoulli limit (setting $r = 0$ in both figures), the current in-fluid, Timoshenko model provides the expected resonant frequency result, λ_{res}= 1.8751, which is in perfect agreement with the resonant frequency provided by the classic in-vacuum, Euler-Bernoulli beam theory.

4.7.2 Comparison of Resonant Frequency and Quality Factor: Current Model and In-Fluid, Euler-Bernoulli Model

In order to verify frequency response results and the impact of the fluid resistance on the Timoshenko beam model with harmonic support rotation, Eq. (3-91) is plotted with $r = s = 0$ as a reduction to the in-fluid, Euler-Bernoulli case presented by Heinrich, et al., [2010b]. As shown in Fig. 4-22, the resulting frequency response curves for the total tip displacement of the in-fluid, Timoshenko (TB) model and the in-fluid, Euler-Bernoulli (EB) model are equivalent for $\zeta = (0,2,4,6,8,10)$ over the frequency range $\lambda \in [0,10]$.

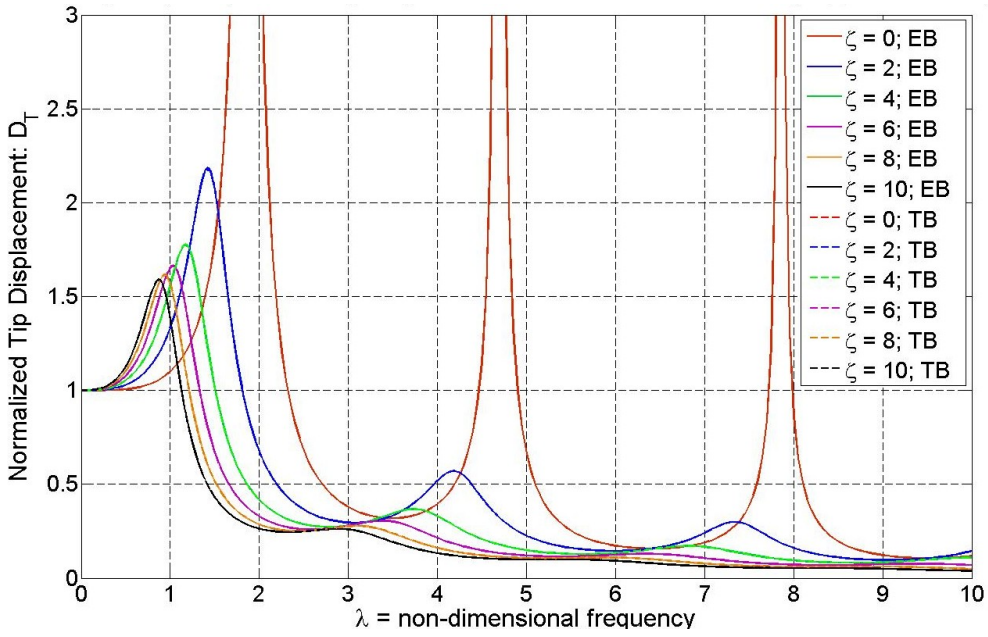

Figure 4-22: Comparison of the Frequency Response Curves of Normalized Total Tip Displacement for Harmonic Support Rotation Obtained from Euler-Bernoulli (EB) [Heinrich et al., 2010b] and Current Timoshenko Beam (TB) Model with Timoshenko Parameters: $r = s = 0$ for Various Fluid Resistance Parameters (ζ)

The values for resonant frequency, shown in Fig. 4-23, are obtained from frequency response curves analogous to those shown in Fig. 4-22. Figure 4-23a shows the resonant frequency comparison (present model vs. model of Heinrich et al. [2010a]) for the case of a harmonic tip load, while Fig. 4-23b displays the comparison for a harmonic support rotation (present model vs. that of Heinrich et al. [2010b]). The results based on the present models are for the special case of $r = s = 0$ (i.e., an Euler-Bernoulli beam). Note that when $r = s = 0$, the bending portion of the TB model, D_B, is equal to the total displacement, D_T, by virtue of no shear contribution. Consequently, eliminating the Timoshenko parameters from Eqs. (3-60) and (3-86) permits direct comparison with Euler-Bernoulli counterparts. However, it is important to note that the results for the harmonic support rotation from the EB model by Heinrich et al. [2010b] *include* the rigid-body rotation (analogous to the D_B of current TB model), whereas this research has focused on results for the bending-deformation displacement, $D_{B\text{-}D}$. Accordingly, in the following verification it is anticipated that the TB results for D_T should agree with those of D_B

when $r = s = 0$ and should match the results given by the previous EB models, whereas the TB results for $D_{B\text{-}D}$ are not expected to match the earlier EB results because of the inclusion of the rigid body motion in the results of Heinrich et al. [2010b].

The resonant frequency results as measured by the total displacement, D_T, and obtained using the current Timoshenko model with $r = s = 0$ are in excellent agreement with those provided by Heinrich et al., for both excitation methods (harmonic tip load [Heinrich et al., 2010a] and harmonic support rotation [Heinrich et al., 2010b]) as shown in Figs. 4-23a and b, respectively, thus providing the desired verification. The results of the present model for the case of harmonic support rotation, represented by D_T=D_B (where the latter corresponds to the bending displacement that *includes* the rigid rotation), are coincident with the earlier EB model results in Fig. 4-23b. (The lower curve in the figure constitutes all three of these results.) However, as expected, there is a clear difference in the resonant frequency for the case of harmonic support rotation (Fig. 4-23b) as measured by $D_{B\text{-}D}$. The difference is due to the fact that the imposed support motion (and the associated rigid body rotation of the beam) is out-of-phase with the beam response and therefore causes the resonant frequency associated with $D_T = D_B$ to be smaller than that based on $D_{B\text{-}D}$, as discussed in Sects. 4-3 and 4-4. This also accounts for the increased difference in these resonant frequencies for higher fluid resistance values. Note, however, that for values of the fluid resistance parameter commonly encountered in lateral-mode microcantilevers, $\zeta \in [0, 0.2]$, the resonant frequency values are essentially the same and are approximately linear in ζ as shown in Fig. 4-24.

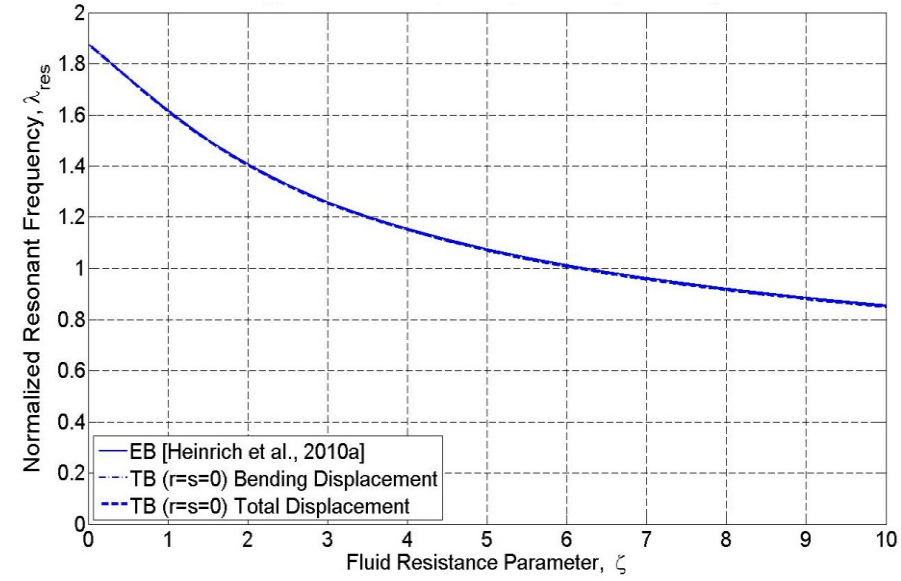

(a)

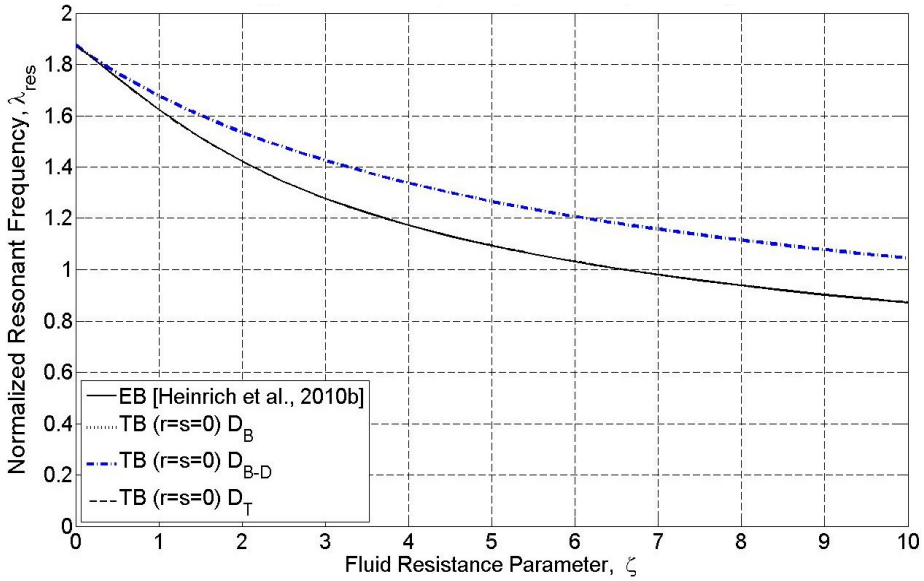

(b)

Figure 4-23: Comparison of Euler-Bernoulli (EB) [Heinrich et al., 2010a, b] and Current Timoshenko Beam (TB) Model: Resonant Frequency for $r = s = 0$ and Various Fluid Resistance Values (ζ): (a) Harmonic Tip Force, (b) Harmonic Support Motion

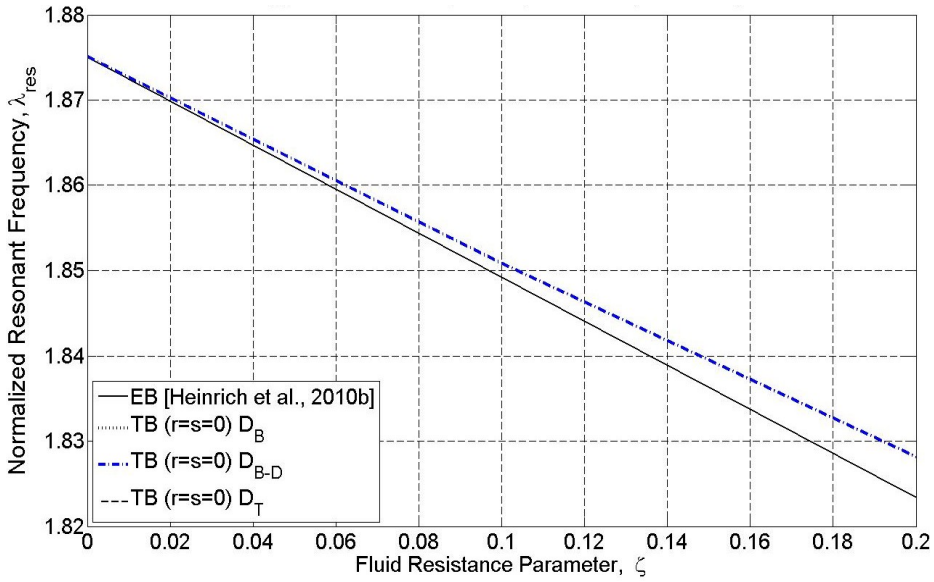

Figure 4-24: Comparison of Euler-Bernoulli (EB) [Heinrich et al., 2010b] and Current Timoshenko Beam (TB) Model: Resonant Frequency for Harmonic Support Motion, $r = s = 0$ and Various Fluid Resistance Values (ζ)

Results for the quality factor (obtained by applying the 3-dB bandwidth method to the results of the present study) are presented in Figs. 4-25a, b for the limiting case of an EB beam in fluid. Elimination of the Timoshenko parameters in the current model provides results that are in excellent agreement with the analytical formula derived by Heinrich et al. for an Euler-Bernoulli beam under harmonic tip force loading [2010a], which was later shown to be a good estimate for the case of harmonic support rotation [2010b]. For $\zeta \in [0, 0.2]$ the agreement between the present results and the previous EB results is excellent, regardless of the method of measurement (total vs. bending displacement) considered in the present model.

4.7.3 Comparison with Numerical Analysis (MATLAB)

Results for the complex vibrational shape of a lateral-mode Timoshenko beam vibrating in a viscous fluid are generated by using the MATLAB solver bvp4c to independently solve the boundary value problem for a harmonic tip force loading, i.e., the coupled, second-order ODEs

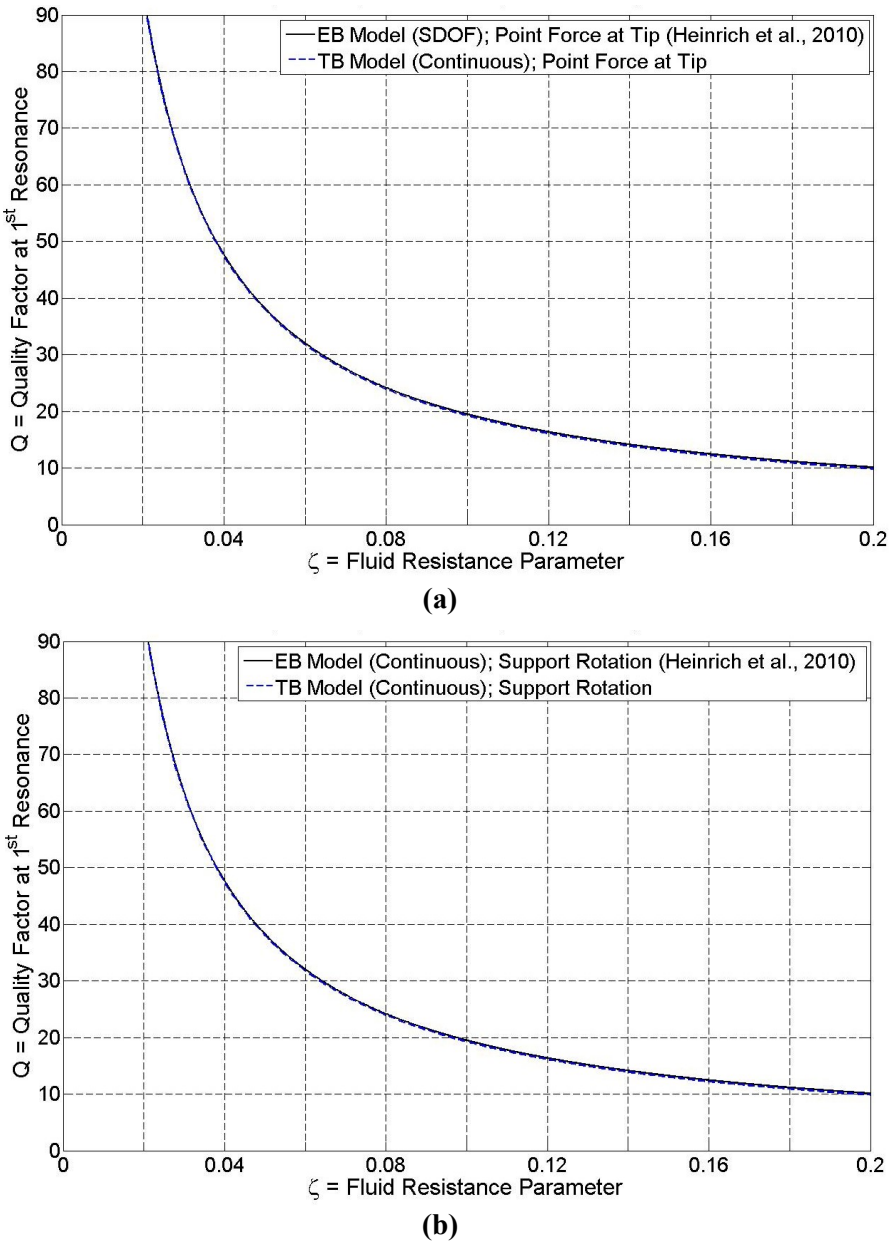

Figure 4-25: Comparison of Euler-Bernoulli (EB) Results of Heinrich et al., [2010a] and Current Timoshenko Beam (TB) Model: Quality Factor for $r = s = 0$ and Various Fluid Resistance Values (ζ): (a) Harmonic Tip Load and (b) Harmonic Support Motion

and concomitant boundary conditions given by Eqs. (3-47), (3-48), and (3-35a-d), respectively. Since the solution methodology for the different loading cases is the same, the check of the harmonic tip load provides confidence for the other load case (the only difference being in the BCs). Applying reduction of order to the two coupled second-order ODEs results in four coupled first-order ODEs with associated BCs for the case of a harmonic tip force. The reduction-of-order

methodology is included in Appendix A, as is the MATLAB program used to generate the solution for the complex vibrational shapes of the total displacement and bending slope [$\bar{V}(\xi)$ and $\Phi(\xi)$, respectively]. Since the program was used to check beam response for a range of Timoshenko and fluid resistance parameters, Figs. 4-26 through 4-29 are presented to exemplify the consistent agreement between the two methods over a range of values. Figures 4-26 and 4-27 show the real and imaginary parts of the complex bending slope amplitude while Figs. 4-28 and 4-29 provide the same results for the complex total displacement amplitude. These comparisons give a high level of confidence that the analytical solution methodology presented in this dissertation is valid and generates accurate solutions to the theoretical problem that has been formulated herein.

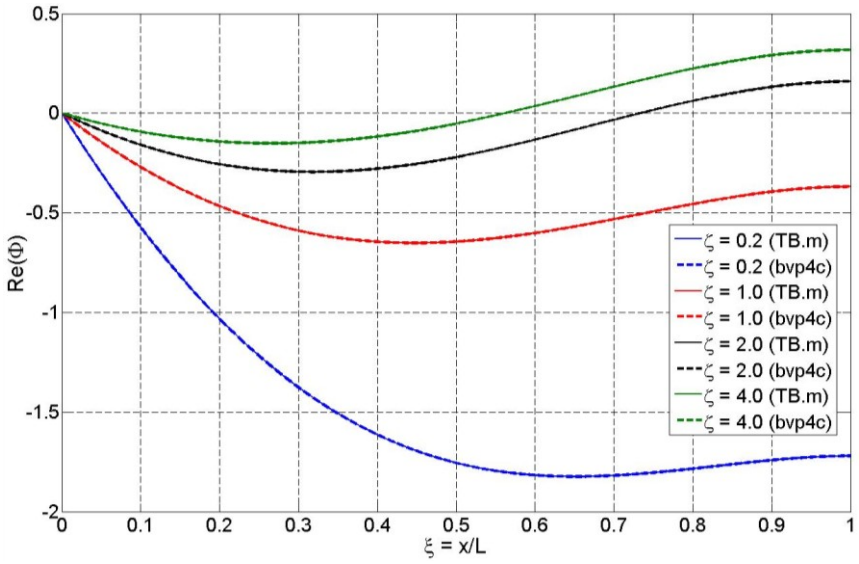

Figure 4-26: Real Part of Complex Bending Slope Amplitude due to Harmonic Tip Force for *b/L* = 0.69 (*r* = 0.2), *s* = 0.4 and λ = 1.87

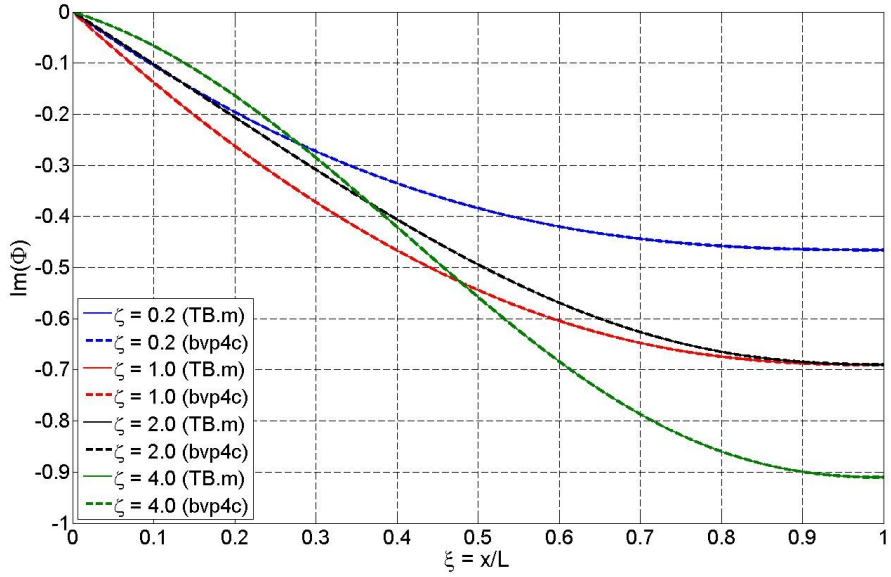

Figure 4-27: Imaginary Part of Complex Bending Slope Amplitude due to Harmonic Tip Force for *b/L* = 0.69 (*r* = 0.2), *s* = 0.4 and λ = 1.87

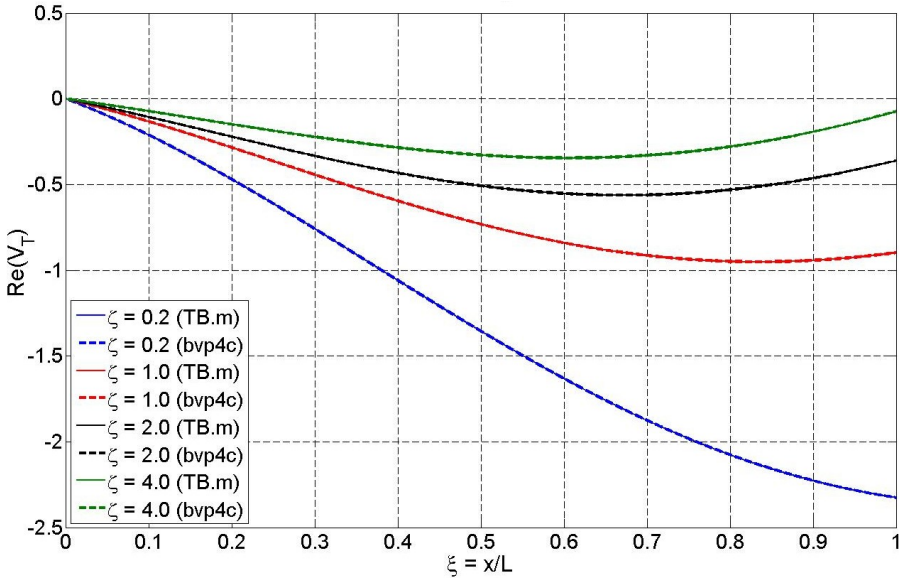

Figure 4-28: Real Part of Complex Total Displacement Amplitude due to Harmonic Tip Force for *b/L* = 0.69 (*r* = 0.2), *s* = 0.4 and λ = 1.87

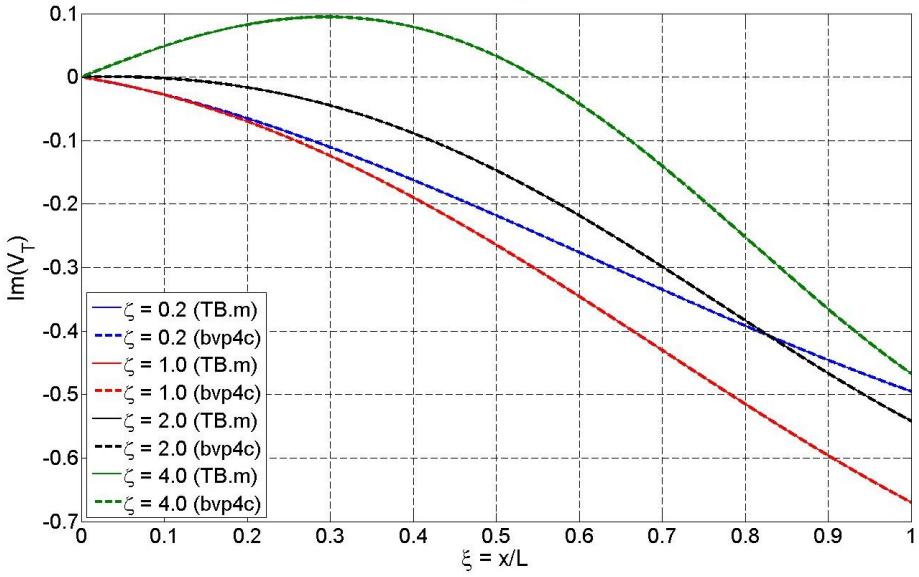

Figure 4-29: Imaginary Part of Complex Total Displacement Amplitude due to Harmonic Tip Force for b/L = 0.69 (r = 0.2), s = 0.4 and λ = 1.87

4.8 Comparison of Theoretical Model (Support Rotation Load) with Experimental Data

In Sect. 4.8 the frequency and quality factor values generated by the new, in-fluid, Timoshenko beam model will be compared to the experimental data collected by colleagues at Georgia Tech [Beardslee et al., 2010a-d; Beardslee et al., 2012] on lateral-mode microcantilevers. As noted earlier (Sects. 4.3 and 4.4), the theoretical values of resonant frequency and quality factor are essentially independent of the type of load (harmonic tip load or harmonic support rotation) when the total tip displacement is used to monitor response, but that there are some noticeable differences in results of the two detection methods for the case of support rotation loading. Because of the methods of loading (electrothermal, near the support) and detection (piezoresistive, near the support) used in the actual devices, the most appropriate of the present theoretical solutions to use for the comparison is deemed to be that based on support rotation loading with the relevant signal being the tip displacement due to bending deformation ($D_{B\text{-}D}$). (See prior discussion in Sect. 1-5.) Note that, while the current theory assumed a homogenous beam, the microcantilever is actually a composite of several different layers, namely a silicon

base layer and several passivation layers [Cox et al., 2012]. As a result of the layered composition of the beam, the material properties (notably *E* and *G*) are difficult to obtain directly. Since there will be some inherent variability in the theoretical results associated with the input values for these material parameters, the results from the current TB model are presented and compared to theoretical results from EB theory and experimental data primarily to investigate *trends* in the resonant frequency and quality factor, as opposed to being utilized in a quantitative predictive capacity.

4.8.1 Specification of Geometric and Material Parameters in Model

Section 4.8.1 discusses the material and geometric parameters that will be specified as input to the current, in-fluid, TB model to generate theoretical results for comparison with experimental data. The specimen geometries used to obtain the theoretical values are grouped by nominal Si thicknesses, h_{nom} = (5, 8, 12, 20) μm, and within each thickness set there are the following potential length and width dimensions: L = (200, 400, 600, 800, 1000) μm, and b = (45, 60, 75, 90) μm. Note that experimental results do not exist for a few combinations of these dimensions; thus, theoretical values were only calculated for those geometries that correspond to experimental data. For all of the results comparisons provided in Sec 4.8.2, estimates of the total thicknesses are used in lieu of the nominal silicon thicknesses. The total thickness for each specimen set is obtained by taking the average silicon thickness for a specimen set and adding the estimated total passivation layer thickness. The latter consists of thermal oxide, PECVD silicon nitride and PECVD silicon oxide layers [Beardslee et al., 2012]. The resulting total thickness values used in the theoretical modeling are listed in Table 4-2.

To generate theoretical results it is necessary to also specify numerical values of the following material parameters: $C1 \equiv \sqrt{E/12\rho_b}$ and $C2 \equiv \sqrt{E/kG}$. As already noted, due to the

Nominal Thickness, h_{nom} [μm]	Average Si Thickness, h_{Si} [μm]	Passivation Layer Thickness, h_p [μm]	Total Thickness, h [μm]
5	5.169	1.840	7.02
8	8.480	1.840	10.32
12	12.61	1.870	14.48
20	20.47	1.870	22.34

Table 4-2: Average Total Thickness for Each Nominal Thickness Set [Beardslee et al., 2012; also using raw data provided courtesy of O. Brand and L.A. Beardslee, Georgia Tech.]

composite nature of the fabricated cantilevers, it is difficult to specify appropriate values of the effective Young's modulus E or shear modulus G. Therefore, the input values of the parameters $C1$ and $C2$ were determined by fitting the *in-vacuum* results of the present model to *in-air* experimental data (assuming that the air resistance has negligible impact on the resonant frequency). These *same* values of $C1$ and $C2$ were then used in making the comparison between the *in-water* results of the present model and the *in-water* experimental data, which is the comparison of main interest in this study. In addition, a second method for generating theoretical results is also presented. This alternative approach utilizes the same $C1$ value as from the "fitting approach," but uses a "textbook" value for $C2$. This value corresponds to using the orthotropic material properties of a standard (100) silicon wafer with microcantilever oriented along the [110] axis, E = 169 GPa and G = 50.9 GPa [Hopcroft et al., 2010], and k = 5/6 (Cowper, 1966, for the case of zero Poisson's ratio). This second approach yields a value of $C2$=2.

The specific procedure for determining the values of $C1$ and $C2$ by curve-fitting will now be summarized. First, the in-fluid Timoshenko model is reduced to the in-vacuum case by specifying $\zeta = 0$, then used to fit the in-air experimental data for resonant frequency. This is accomplished by minimization of the total squared error, as detailed in Appendix B. This process results in the best-fit values for $C1 \equiv \sqrt{E/12\rho_b}$ and $C2 \equiv \sqrt{E/kG}$, which are listed in Table 4-3 for each specimen set. The plots of the theoretical resonant frequency for the in-vacuum Timoshenko model and the plots of the in-air experimental frequency data are in excellent agreement and are

provided in Appendix C for comparison. Note that the $C1$ values govern the initial slopes of the theoretical curves, while the $C2$ values are associated with the degree of curvature (i.e., departure from linearity) at larger values of b/L^2. Having determined these parameter values, the in-fluid, Timoshenko model may be employed to generate theoretical results for comparison with in-water experimental data for those geometries specified in this section. Such comparisons will be made in the next section.

The values of the effective modulus E listed in Table 4-3 are obtained using the best fit values for $C1 \equiv \sqrt{E/12\rho_b}$ and back-calculating E by assuming the density of the beam as that of pure silicon (i.e., $\rho_b = 2330$ kg/m^3). It is worth noting that the effective modulus of elasticity obtained from the $C1$ values follows a decreasing trend as the thickness increases. A possible explanation for this behavior may be that, as the actual stiffness of the beam increases (via increasing thickness) for constant b/L, the relative support compliance may be increasing. Consequently, although the beam stiffness is increasing, the overall system has a decreasing stiffness due to increasing support compliance. The present model does not account for support compliance, in which case the fitting process may be incorporating this effect indirectly via a reduced effective modulus value.

Nominal Thickness, h_{nom} [μm]	***C*1 [km/sec]**	***C*2**	***E* [GPa]**
5	2.324033	4.423125	151.0
8	2.190268	3.511667	134.1
12	2.191986	3.128750	134.3
20	2.144676	3.064167	128.6

Table 4-3: *C*1 and *C*2 Best-Fit Parameters and Effective Young's Modulus Based on Fitting In-Vacuum Model to In-Air Frequency Data

4.8.2 Comparison of Theory and Experimental Data

Recall from Sect. 1.2 that one of the initial impetuses for this research was the apparent drop-off in experimental resonant frequency observed at high values of b/L^2. One of the hypothesized justifications for such a divergence between the experimental resonant frequency and that predicted by the Euler-Bernoulli-based theories was that at high values of b/L^2 certain assumptions regarding Euler-Bernoulli theory (i.e., $b<<L$) cease to be valid, thus eliciting the derivation and application of the current in-fluid, Timoshenko beam model. For this reason the results of the new Timoshenko beam model will be compared with in-water experimental data in this section to ascertain if it will provide a significant improvement over Euler-Bernoulli models. In making these comparisons, the properties of water will be specified as $\rho_f = 1000$ kg/m^3 and $\eta =$ 0.001 Pa-s in the theoretical model.

Using the best-fit $C1$ and $C2$ values listed in Table 4-3 of the previous section, the current in-fluid, Timoshenko model is used to generate the in-water theoretical resonant frequencies (f_{res}) for the various specimen geometries, which are compared with the corresponding experimental data. These comparisons are shown in Figs. 4-30 through 4-33. Note that, for the largest values of b/L^2, the theoretical resonant frequencies considering TB effects are 70-97% closer to the experimental data than the approximate analytical formula of Heinrich et al. [2010a], which was based on Euler-Bernoulli theory . (These percentages are based on the relative difference of the last two columns of Table 4-4a with the EB value taken as the reference.) While this is a significant improvement in frequency modeling, Table 4-4a as well as the corresponding figures show that the current method still tends to overestimate the experimental frequency, by 6-12% for the least slender specimen for each thickness set. This is especially evident for the thicker specimens (Figs. 4-32 and 4-33), for which the validity of the Stokes fluid resistance assumption becomes more questionable. For example, the new model accurately reflects the trends of the experimental frequency data and, for the thinner specimens (nominal thicknesses of 5 μm and 8

μm), seems to provide a very good quantitative estimate of frequency (Figs. 4-30 and 4-31). At the larger nominal thicknesses (i.e., 12 μm and 20 μm) considered in Figs. 4-32 and 4-33, however, the in-fluid model overestimates the resonant frequency for the larger b/L^2 specimens. This is likely due to the fact that the Stokes fluid resistance assumption employed in the current model neglects the pressure effects on the smaller faces of the beam's lateral surface. Note that at larger thicknesses, the fluid pressure effects may need to be included for more accurate modeling.

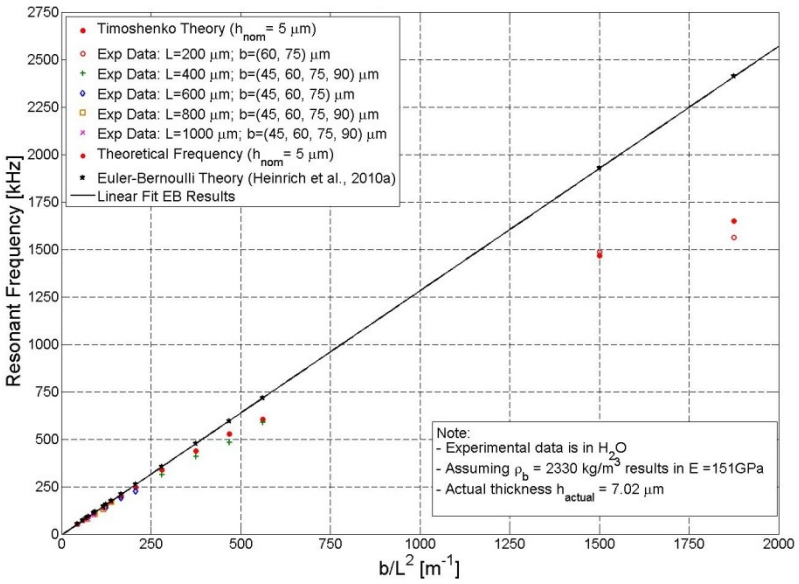

Figure 4-30: Comparison of Current In-Fluid, Timoshenko Model to Experimental [Beardslee et al., 2010d] In-Fluid Resonant Frequencies For First Lateral Flexural Mode Due to Harmonic Support Rotation; Nominal Thickness of 5 μm, $\sqrt{E/12\rho_b}$ = 2.3240 km/sec, $\sqrt{E/kG}$ = 4.4231 and E = 151 GPa

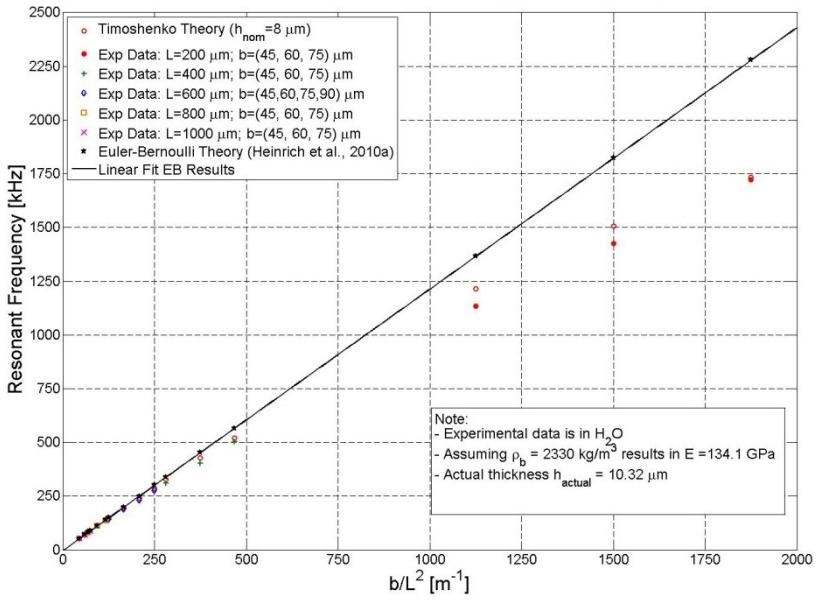

Figure 4-31: Comparison of Current In-Fluid, Timoshenko Model to Experimental [Beardslee et al., 2010d] In-Fluid Resonant Frequencies For First Lateral Flexural Mode Due to Harmonic Support Rotation; Nominal Thickness of 8 μm, $\sqrt{E/12\rho_b}$ = 2.1903 km/sec, $\sqrt{E/kG}$ = 3.5117 and E = 134.1 GPa

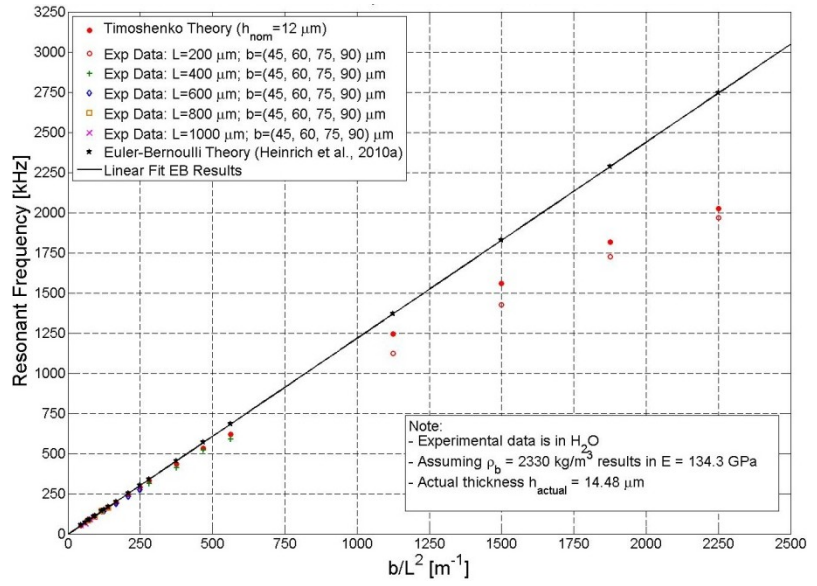

Figure 4-32: Comparison of Current In-Fluid, Timoshenko Model to Experimental [Beardslee et al., 2010d] In-Fluid Resonant Frequencies For First Lateral Flexural Mode Due to Harmonic Support Rotation; Nominal Thickness of 12 μm, $\sqrt{E/12\rho_b}$ = 2.1921 km/sec, $\sqrt{E/kG}$ = 3.1288 and E = 134.3 GPa

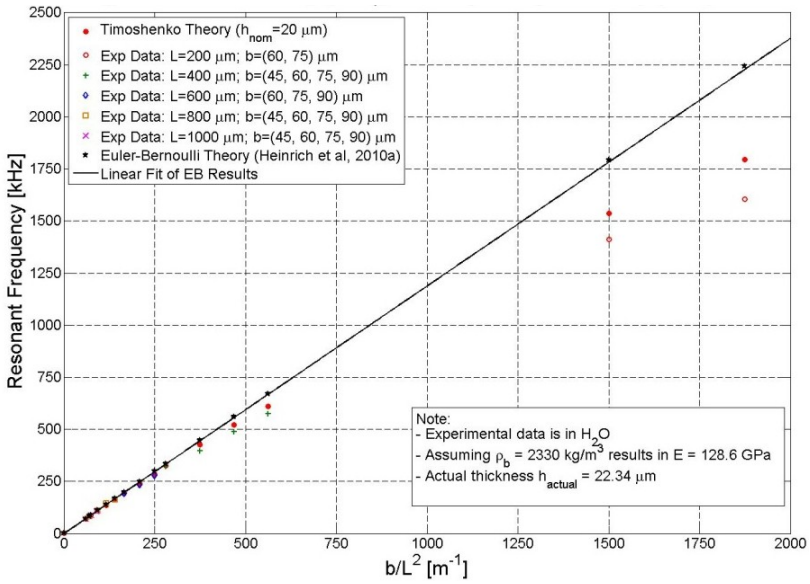

Figure 4-33: Comparison of Current In-Fluid, Timoshenko Model to Experimental [Beardslee et al., 2010d] In-Fluid Resonant Frequencies For First Lateral Flexural Mode Due to Harmonic Support Rotation; Nominal Thickness of 20 μm, $\sqrt{E/12\rho_b}$ = 2.1447 km/sec, $\sqrt{E/kG}$ = 3. 0642 and E = 128.6 GPa

Since the $C2$ values by the aforementioned fitting method seem uncharacteristically high, possibly indicating that they are indirectly accounting for other effects (e.g., support compliance), an alternative approach will be taken for making comparisons between theory and experiment. In this approach, one may simply specify $C2$=2 based on the use of published values for the moduli of pure Si and using k=5/6 as noted in the previous section. Comparisons of the new theoretical curves with the experimental data are presented in Figs. 4-34 through 4-37. It is observed that the present model captures the overall trend in the resonant frequency and that, for the largest values of b/L^2, the theoretical TB resonant frequencies are 31-52% closer to the experimental data than the Euler-Bernoulli values (for the highest b/L ratios when L = 200 μm in Figs. 4-34 through 4-37.) (Again, these figures are based on the relative difference of the last two columns of Table 4-4b with the EB value taken as the reference.) While this is a significant improvement in frequency prediction over Euler-Bernoulli theory, the current method still overestimates the experimental frequency by 18-37%. This discrepancy is likely attributable to the breakdown of the Stokes resistance assumption and the fact that support compliance effects are neglected. These

observations provide the incentive for future work to (a) utilize a more exact hydrodynamic function to model the fluid effects in order to more accurately predict the in-liquid resonant frequency, and (b) incorporate support compliance effects into the current model. (See Sect. 6.3.)

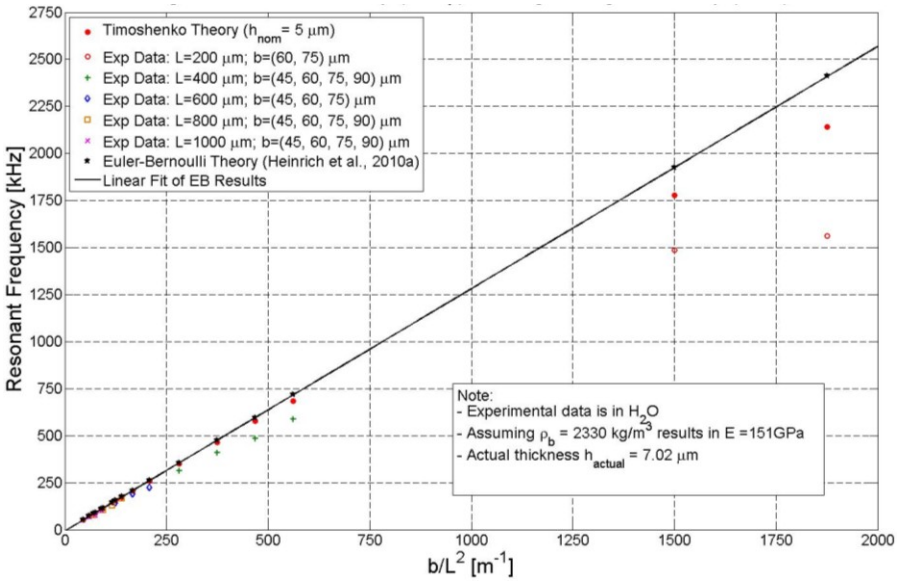

Figure 4-34: Comparison of Current In-Fluid, Timoshenko Model to Experimental [Beardslee et al., 2010d] In-Water Resonant Frequencies For First Lateral Flexural Mode Due to Harmonic Support Rotation; Nominal Thickness of 5 μm, $\sqrt{E/12\rho_b}$ = 2.3240 km/sec, $\sqrt{E/kG}$ = 2

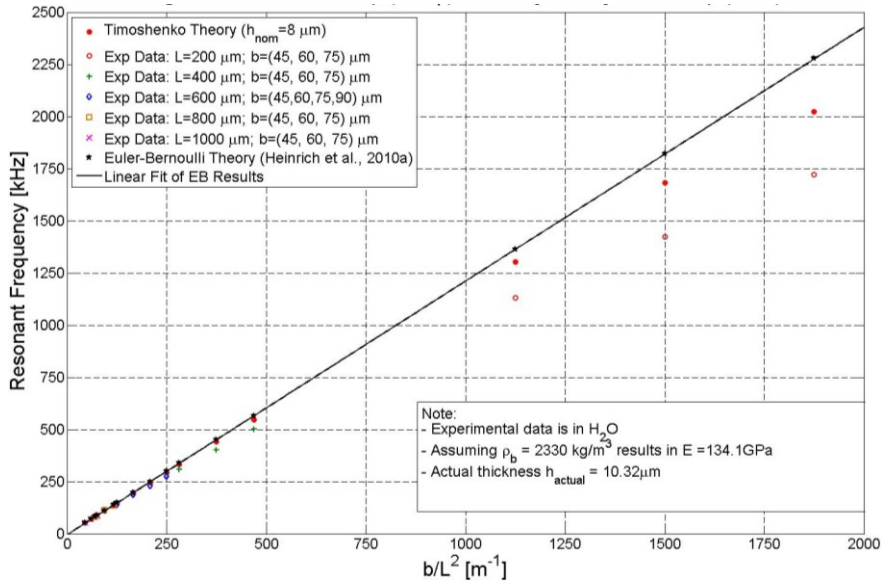

Figure 4-35: Comparison of Current In-Fluid, Timoshenko Model to Experimental [Beardslee et al., 2010d] In-Water Resonant Frequencies For First Lateral Flexural Mode Due to Harmonic Support Rotation; Nominal Thickness of 8 μm, $\sqrt{E/12\rho_b}$ = 2.1903km/sec, $\sqrt{E/kG}$ = 2

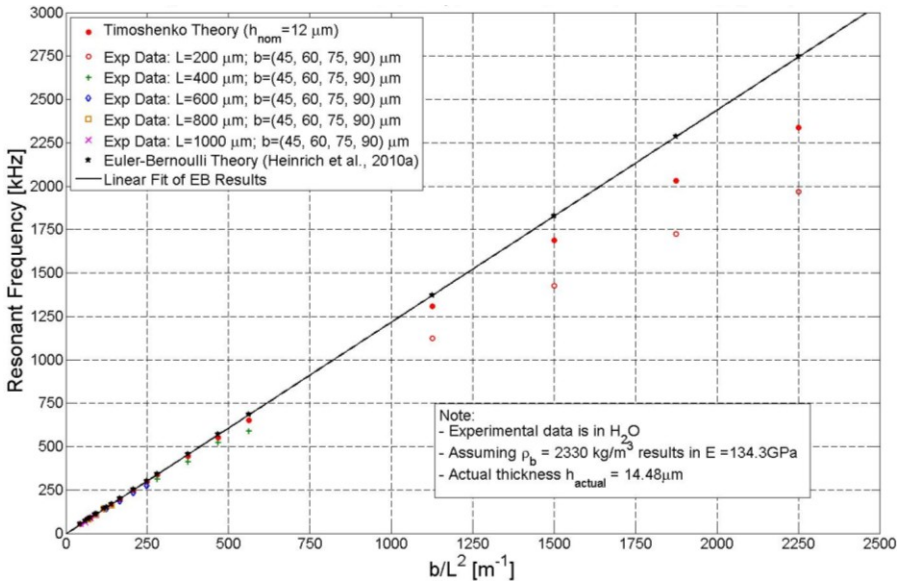

Figure 4-36: Comparison of Current In-Fluid, Timoshenko Model to Experimental [Beardslee et al., 2010d] In-Water Resonant Frequencies For First Lateral Flexural Mode Due to Harmonic Support Rotation; Nominal Thickness of 12 μm, $\sqrt{E/12\rho_b}$ = 2.1920 km/sec, $\sqrt{E/kG}$ = 2

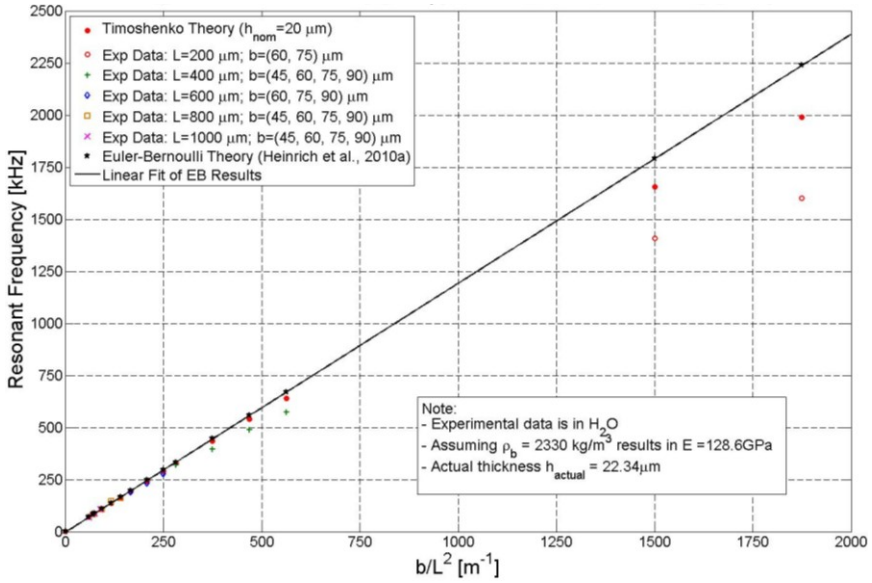

Figure 4-37: Comparison of Current In-Fluid, Timoshenko Model to Experimental [Beardslee et al., 2010d] In-Water Resonant Frequencies For First Lateral Flexural Mode Due to Harmonic Support Rotation; Nominal Thickness of 20 μm, $\sqrt{E/12\rho_b}$ = 2.1447 km/sec, $\sqrt{E/kG}$ = 2

Comparing the resonant frequency results found in Table 4-4 and in Figs. 4-30 through 4-37 for the two different methods for specifying the value of *C*2 (i.e., using "best-fit" *C*2 and "textbook" (pure Si) *C*2 = 2) indicates that, when the best-fit method is used, the TB model is 70-

97% closer to the experimental data than the EB model (as noted earlier) for the largest *b/L* ratio of each thickness data set. For the case in which *C*2=2 is used, the TB model shows less improvement (31-52%) over the EB model, but still captures the overall trend for the resonant frequency. Obviously, the case of the "best-fit" *C*2 fits the experimental data more closely than the *C*2 = 2 case because the best-fit values are from the minimization of error using the in-air data. However, the best-fit *C*2 value, as noted earlier, may be indirectly accounting for effects other than Timoshenko beam effects (e.g., support compliance), so that the *C*2 = 2 approach is deemed to be a "fairer" means of evaluating the predictive capabilities of the present theoretical model.

					% difference		
Specimen Set, h_{nom} [µm]	**b [µm] / L [µm]**	**$f_{res,EB}$ [kHz]**	**$f_{res,TB}$ [kHz]**	**$f_{res,exp}$ [kHz]**	**$f_{res,EB}$ vs $f_{res,TB}$**	**$f_{res,TB}$ vs $f_{res,exp}$**	**$f_{res,EB}$ vs $f_{res,exp}$**
5	75/200	2412	1648	1562	46%	6%	54%
8	75/200	2280	1735	1723	31%	1%	32%
12	90/200	2746	2025	1968	36%	3%	40%
20	75/200	2242	1794	1604	25%	12%	40%

(a)

					% difference		
Specimen Set, h_{nom} [µm]	**b [µm] / L [µm]**	**$f_{res,EB}$ [kHz]**	**$f_{res,TB}$ [kHz]**	**$f_{res,exp}$ [kHz]**	**$f_{res,EB}$ vs $f_{res,TB}$**	**$f_{res,TB}$ vs $f_{res,exp}$**	**$f_{res,EB}$ vs $f_{res,exp}$**
5	75/200	2412	2142	1562	13%	37%	54%
8	75/200	2280	2026	1723	13%	18%	32%
12	90/200	2746	2337	1968	18%	19%	40%
20	75/200	2242	1993	1604	13%	24%	40%

(b)

Table 4-4: Resonant Frequency Percent Difference Among: Euler-Bernoulli Theory (Heinrich et al., 2010a), Current Timoshenko Theory and Experimental Data of Beardslee et al. [2010a-d; 2012] for: (a) Best-Fit *C*1 and *C*2 and (b) Best-Fit *C*1 and *C*2 = 2 from Specified Silicon Material Properties

The theoretical quality factors corresponding to specimen geometries of various thicknesses are calculated using the 3-dB bandwidth method as described in Sect. 4.3. Again, the figures are presented first for the case of using the best-fit parameters, *C*1 and *C*2, in Figs. 4-38 through 4-41. Then the quality factor is calculated using the second approach (using the *C*2 = 2

value) in Figs. 4-42 to 4-45. The trends observed in the preceding frequency comparisons are also encountered in the comparisons of the quality factor in water: (1) while the current theoretical Q values consistently overpredict the experimental Q data, they provide a tighter upper bound than the previous Euler-Bernoulli model (i.e., than the approximate analytical formula of Heinrich et al. [2010a]) for the "stubbier" (higher b/L) specimens; (2) the theoretical Q based on the present model provides an excellent quantitative estimate for the thinner experimental specimen sets (i.e., nominal thicknesses of 5 μm and 8 μm), while for the thicker specimens the accuracy deteriorates due to the limitations of the Stokes-type fluid resistance assumption and potential support compliance effects; (3) the theoretical Q predictions of the present model capture qualitatively the experimentally observed departure from linearity in Q for higher b/L^2 specimens; and (4) as was seen in the case of resonant frequency results, the theoretical Q curves based on the artificially high, best-fit $C2$ values (Figs. 4-38 through 4-41) show better agreement with the data than those based on a more "realistic" value of $C2 = 2$ (Figs. 4-42 through 4-45). (Again, this may be due to support compliance effects that are indirectly incorporated via the best-fit $C2$ value.) However, the sensitivity of the predicted Q values on the specified value of parameter $C2$ is much smaller than it is for the frequency predictions.

To capture the efficacy of the current model in approximating the experimental Q data, the percent differences in the quality factor for the largest b/L^2 specimen at each thickness are compared for the current Timoshenko model, the Euler-Bernoulli model of Heinrich et al. [2010a], and the experimental data. The results are shown in Table 4-5a, b. The results indicate that the current Timoshenko model provides improved theoretical quality factor results compared to the Euler-Bernoulli analytical formula from the literature.

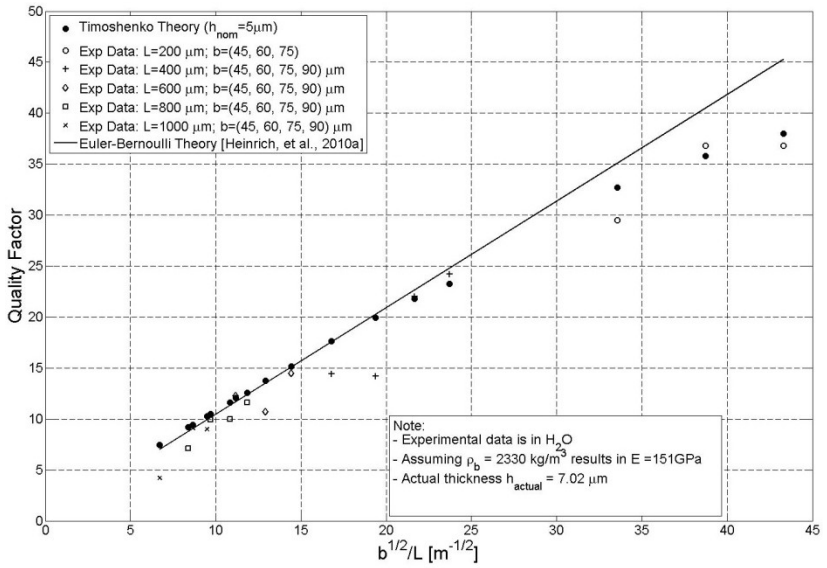

Figure 4-38: Comparison of Current In-Fluid, Timoshenko Model to Experimental [Beardslee et al., 2012] Quality Factor for First Lateral Flexural Mode, Nominal Thickness 5 μm Using $\sqrt{E/12\rho_b}$ = 2.3240 km/sec and $\sqrt{E/kG}$ = 4.4231

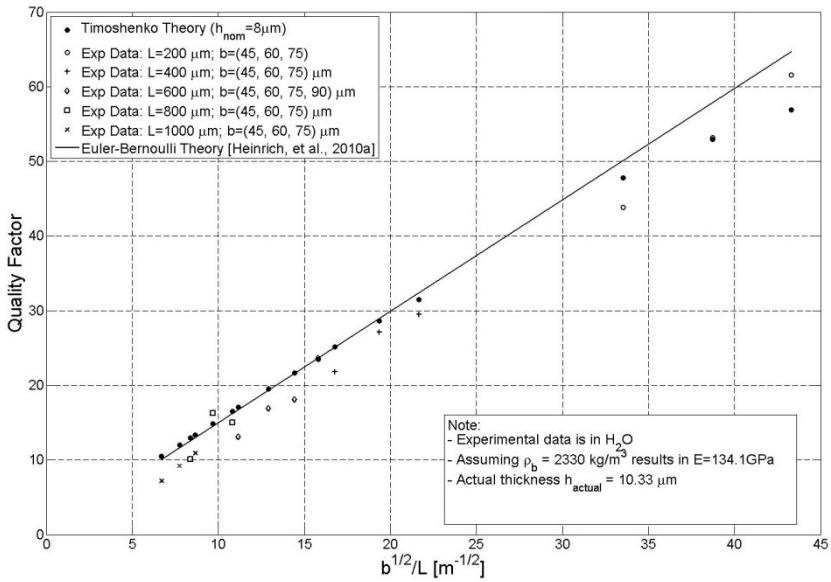

Figure 4-39: Comparison of Current In-Fluid, Timoshenko Model to Experimental [Beardslee et al., 2012] Quality Factor for First Lateral Flexural Mode, Nominal Thickness 8 μm Using $\sqrt{E/12\rho_b}$ = 2.1903 km/sec and $\sqrt{E/kG}$ = 3.511667

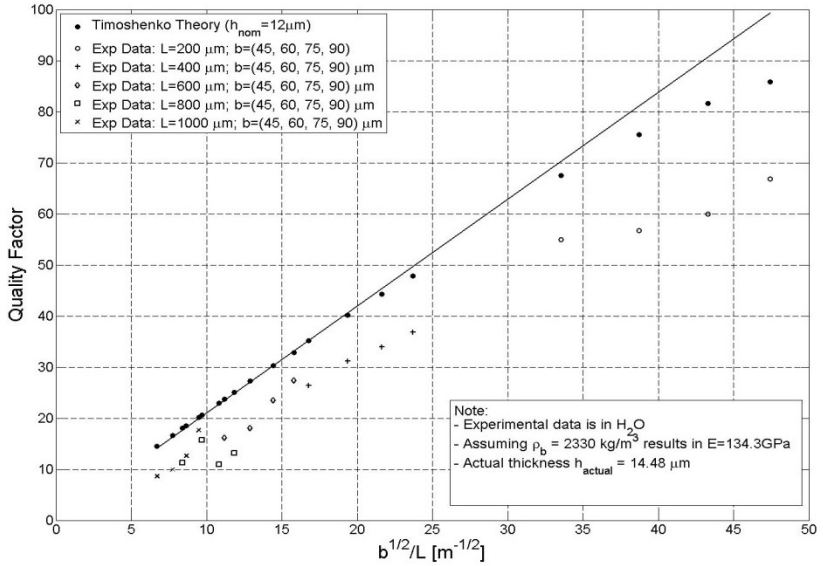

Figure 4-40: Comparison of Current In-Fluid, Timoshenko Model to Experimental [Beardslee et al., 2012] Quality Factor for First Lateral Flexural Mode, Nominal Thickness 12 μm Using $\sqrt{E/12\rho_b}$ = 2.1920 km/sec and $\sqrt{E/kG}$ = 3.1288

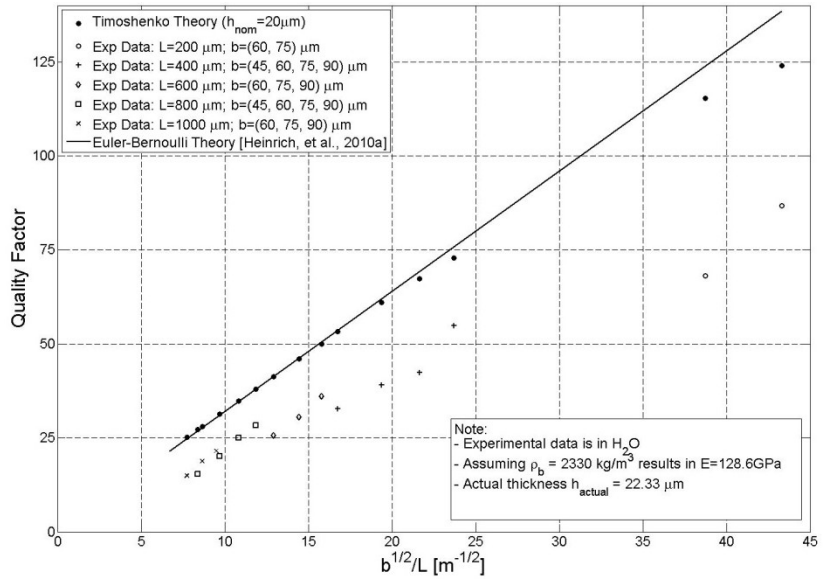

Figure 4-41: Comparison of Current In-Fluid, Timoshenko Model to Experimental [Beardslee et al., 2012] Quality Factor for First Lateral Flexural Mode, Nominal Thickness 20 μm Using $\sqrt{E/12\rho_b}$ = 2.1447 km/sec and $\sqrt{E/kG}$ = 3.0642

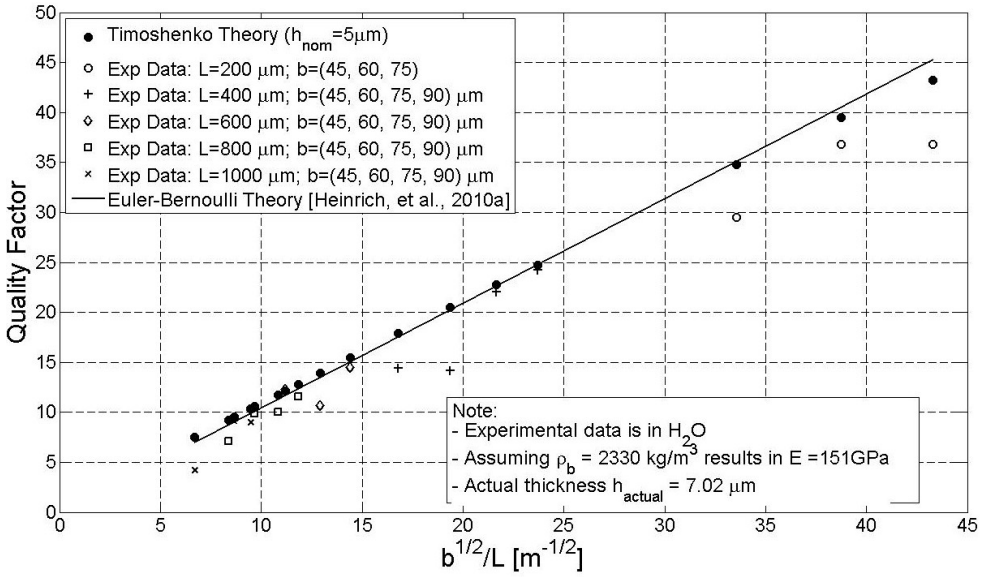

Figure 4-42: Comparison of Current In-Fluid, Timoshenko Model to Experimental [Beardslee et al., 2012] Quality Factor for First Lateral Flexural Mode, Nominal Thickness 5 μm Using $\sqrt{E/12\rho_b}$ = 2.3240 km/sec and $\sqrt{E/kG}$ = 2

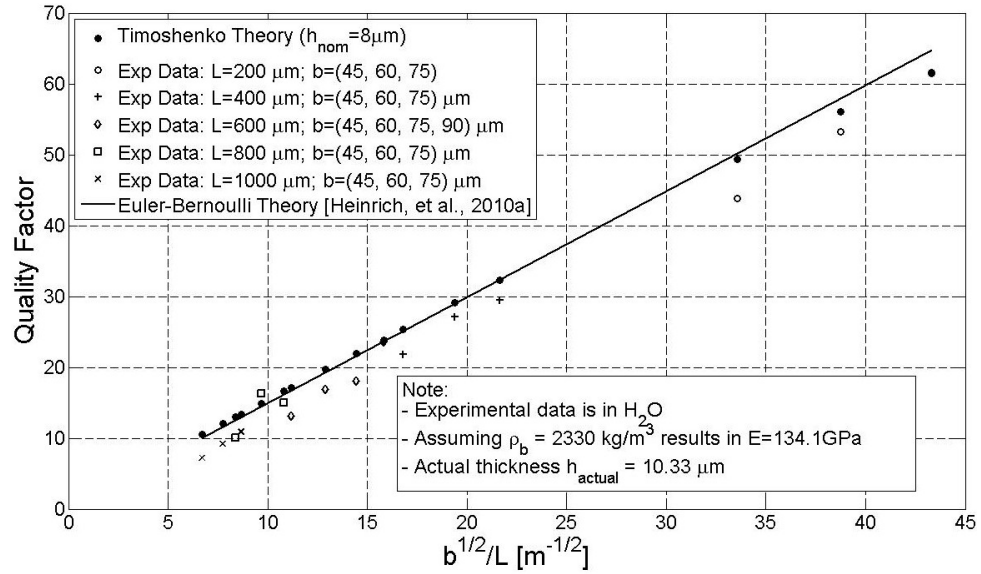

Figure 4-43: Comparison of Current In-Fluid, Timoshenko Model to Experimental [Beardslee et al., 2012] Quality Factor for First Lateral Flexural Mode, Nominal Thickness 8 μm Using $\sqrt{E/12\rho_b}$ = 2.1903 km/sec and $\sqrt{E/kG}$ = 2

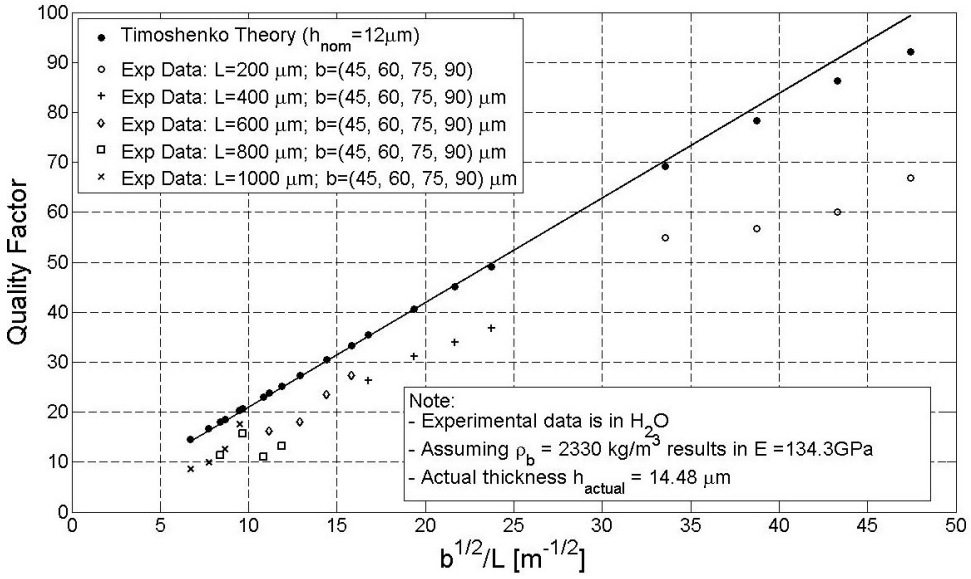

Figure 4-44: Comparison of Current In-Fluid, Timoshenko Model to Experimental [Beardslee et al., 2012] Quality Factor for First Lateral Flexural Mode, Nominal Thickness 12 μm Using $\sqrt{E/12\rho_b}$ = 2.1920 km/sec and $\sqrt{E/kG}$ = 2

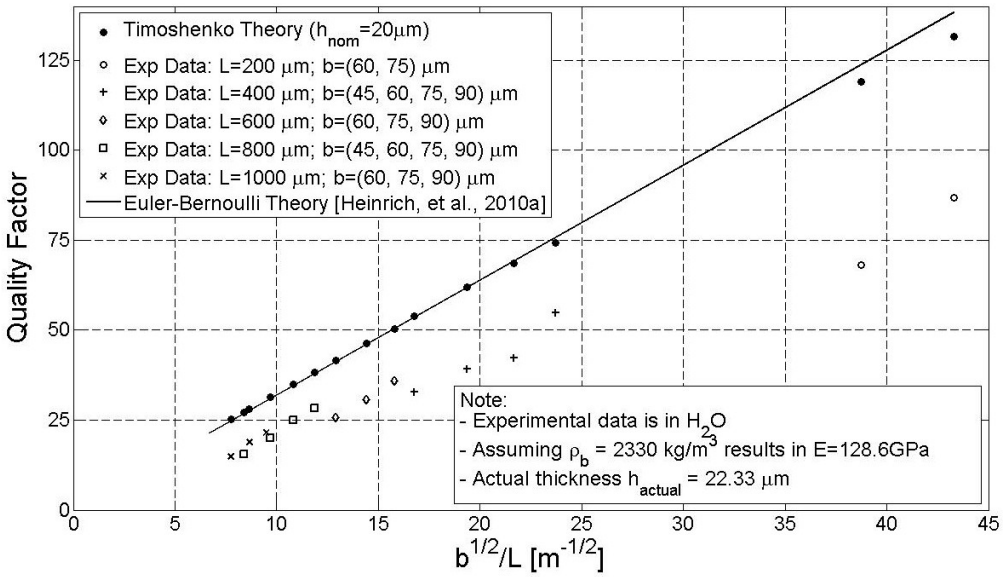

Figure 4-45: Comparison of Current In-Fluid, Timoshenko Model to Experimental [Beardslee et al., 2012] Quality Factor for First Lateral Flexural Mode, Nominal Thickness 20 μm Using $\sqrt{E/12\rho_b}$ = 2.1447 km/sec and $\sqrt{E/kG}$ = 2

					% difference		
Specimen Set, h_{nom} [μm]	**b [μm] / L [μm]**	**Q_{EB}**	**Q_{TB}**	**Q_{exp}**	**Q_{EB} vs Q_{TB}**	**Q_{TB} vs Q_{exp}**	**Q_{EB} vs Q_{exp}**
5	75/200	45.27	37.97	36.8	19%	3%	23%
8	75/200	64.67	56.93	61.6	14%	8%	5%
12	90/200	99.35	85.79	66.8	16%	28%	49%
20	75/200	138.3	124	86.8	12%	43%	59%

(a)

					% difference		
Specimen Set, h_{nom} [μm]	**b [μm] / L [μm]**	**Q_{EB}**	**Q_{TB}**	**Q_{exp}**	**Q_{EB} vs Q_{TB}**	**Q_{TB} vs Q_{exp}**	**Q_{EB} vs Q_{exp}**
5	75/200	45.27	43.21	36.8	5%	17%	23%
8	75/200	64.67	61.52	61.6	5%	0%	5%
12	90/200	99.35	92.18	66.8	8%	38%	49%
20	75/200	138.3	131.6	86.8	5%	52%	59%

(b)

Table 4-5: Quality Factor Percent Difference Among: Euler-Bernoulli Theory (Analytical Formula of Heinrich et al. [2010a]), Current Timoshenko Theory, and Experimental Data of Beardslee et al. [2010a-d; 2012] for: (a) Best-Fit $C1$ and $C2$ and (b) Best-Fit $C1$ and $C2 = 2$ from Specified Silicon Material Properties

For the case of the best-fit $C2$ value (Table 4-5a), the TB model shows an improvement of 27-87% compared to the EB model for three of the four thicknesses. (For the remaining thickness, $h_{nom} = 8$ μm, both theories are very close to the experimental data value.) This represents a greater improvement than furnished by the results based on $C2 = 2$ (Table 4-5b) for the same reasons as mentioned earlier in the frequency comparisons. (The aforementioned improvement range of 27-87% is reduced to 12-26%.) However, as noted earlier, the Q results of the present model are relatively insensitive to the input value of $C2$. (Compare the Q_{TB} columns of Table 4-5a,b.) Again, it is noted that the trend of larger discrepancies between the TB theory and the data as the thickness increases is probably attributable to the fact that, as the thickness increases, the Stokes resistance assumption of neglecting the fluid pressure effects breaks down. This neglected effect causes both the TB and EB models (each based on the assumption of

Stokes-type fluid resistance) to become less accurate in Q prediction as the thickness increases, but overall the TB accuracy tends to remain superior to that of the EB theory for all thicknesses.

CHAPTER 5: APPLICATION OF RESULTS TO MICROCANTILEVER-BASED CHEMICAL SENSORS

5.1 Introductory Remarks

The in-fluid microcantilever response investigated in Ch. 4 reflects the impact of fluid and Timoshenko parameters on the beam response for different loads (harmonic tip force and harmonic support rotation) as well as for different measurement techniques (total displacement and displacement due to bending deformation). The results for resonant frequency and quality factor are important factors in MEMS sensor applications, but determination of microcantilever-based sensor effectiveness requires consideration of additional metrics: mass and chemical sensitivities and limit of detection (LOD). These performance metrics may be related to the resonant frequency and quality factor. Due to this dependence, the improved accuracy of the current model in predicting experimental behavior in the resonant frequency and quality factor at large b/L^2 values should be reflected in better theoretical estimates of mass and chemical sensitivities and LOD. This chapter clarifies the relationships among the following: resonant frequency, quality factor, mass and chemical sensitivities and limit of detection.

In general, the mass sensitivity is the ratio of the change in resonant frequency to the change in mass of the sensor (due to sorbed analyte mass), while the chemical sensitivity is the ratio of the resonant frequency change due to sorption of analyte to the change in concentration of the analyte in the surrounding environment. The limit of detection describes the lower limit of analyte concentration that is detectable by a given sensor. Using the results for resonant frequency and quality factor from the preceding chapters, the mass sensitivity, chemical sensitivity, and limit of detection may be obtained by deriving the necessary relationships as summarized in the next two sections.

5.2 Mass Sensitivity and Chemical Sensitivity

The chemical sensitivity, S_c, can be understood in light of the mass sensitivity, S_m, where the mass sensitivity is defined as the ratio of the change in the resonant frequency to the change in the mass of the sensor due to analyte sorption [Beardslee et al., 2011]. Accordingly, the mass sensitivity is defined as [Narducci et al., 2008]

$$S_m \equiv \frac{\partial f}{\partial m}. \tag{5-1}$$

In an analogous manner, the chemical sensitivity, S_c, is defined as the ratio of the change in resonant frequency to the change in the ambient analyte concentration, C_A:

$$S_c \equiv \frac{\partial f}{\partial C_A}. \tag{5-2}$$

Rewriting Eq. (5-2) in terms of Eq. (5-1) results in

$$S_c = \frac{\partial f}{\partial m}\frac{\partial m}{\partial C_A} = S_m \frac{\partial m}{\partial C_A}. \tag{5-3}$$

The mass of the analyte that is absorbed into the sensor's chemically sensitive coating (after chemical equilibrium has been attained) may be expressed in terms of the volume of the sensitive coating, the concentration of the analyte in the surrounding environment, and the partition coefficient [Hagleitner et al., 2002; Cox, 2011; Beardslee et al., 2011]. The partition coefficient describes the tendency of absorption between a given analyte/coating pair (in a specific environment) and is defined as the ratio of the change in concentration of analyte in the coating to that in the surrounding environment (at equilibrium):

$$K = \frac{\Delta m / V_{coating}}{\Delta C_A}, \tag{5-4}$$

where

$\Delta m =$ the change in mass in the coating due to sorbed mass,

$V_{coating}$ = the volume of the chemically sensitive coating,

ΔC_A = change in ambient concentration of analyte.

Using Eq. (5-4), the change in mass per change in ambient analyte concentration is obtained as

$$\frac{\partial m}{\partial C_A} = KV_{coating} . \tag{5-5}$$

Rewriting Eq. (5-3) using (5-5) provides the chemical sensitivity as a function of mass sensitivity:

$$S_c = KV_{coating} S_m . \tag{5-6}$$

The relationship between chemical and mass sensitivity in Eq. (5-6) permits the investigation and optimization of either quantity with respect to changes in the cantilever design parameters [Cox, 2011]. However, it must be emphasized that the $V_{coating}$ factor in Eq. (5-6) is dependent on cantilever geometry (typically proportional to bL) and thus the dependence of mass sensitivity and chemical sensitivity on cantilever geometry will differ.

Recall that the mass sensitivity, S_m, is related how the system resonant frequency depends on mass. (See Eq. (5-1).) Also recall that the resonant frequency results (as presented in Sects. 4-3 and 4-4) are dependent on the Timoshenko and fluid parameters, which involve inertial effects and will thus affect the mass sensitivity. Higher mass sensitivity is obtained by the largest possible frequency shift for a given change in mass, so clearly the complicating effects of rotatory inertia and effective fluid mass may need to be incorporated if one wishes to maximize the mass sensitivity and, thus, the chemical sensitivity.

5.3 Limit of Detection

The limit of detection (LOD) is an important measure of sensor performance. For resonant-mode chemical sensors of the type considered herein, the LOD can be defined as "the analyte concentration corresponding to a frequency shift equal to three times the frequency noise, Δf_{noise}, of the system measurement" [e.g., Lochon et al., 2005]. This definition of the LOD, along with Eq. (5-2), can be used to express LOD as

$$LOD = \frac{3\Delta f_{noise}}{S_c} \quad . \tag{5-7}$$

Additionally, the noise of the resonant system (assuming, for example, that the microcantilever-based sensor is operating in an oscillator feedback loop configuration) is proportional to the ratio of the resonant frequency to the quality factor [e.g., Fadel et al., 2003; Lochon et al., 2005]:

$$\Delta f_{noise} \propto \frac{f_{res}}{Q} \, . \tag{5-8}$$

By substituting Eq. (5-8) into Eq. (5-7), the dependence of the LOD on the cantilever's resonant frequency, quality factor, and chemical sensitivity may be determined:

$$LOD \propto \frac{f_{res}}{Q S_c} \quad . \tag{5-9}$$

From the relationship in Eq. (5-9) it is apparent that maximizing the resonant frequency while minimizing the quality factor and chemical sensitivity will maximize the LOD. However, since the LOD and S_c are both important parameters in sensor design, the optimization of the sensor will rely on a balanced approach to maximization of LOD and S_c.

5.4 Trends in Sensitivity and Limit of Detection

Previous work by Cox [2011] provides a preliminary investigation of the impact of geometry on mass sensitivity, chemical sensitivity and LOD for the lateral vibration of an Euler-Bernoulli microcantilever in a viscous fluid. The purpose of this section is to use an analogous approach to demonstrate how the in-fluid, Timoshenko beam model of the present study may be used to determine mass sensitivity, chemical sensitivity, and limit of detection (LOD) and examine any trends exhibited between cantilever geometry and these performance metrics. No attempt is made here to perform an exhaustive parametric study on sensitivities and LOD, but to simply outline the approach that could be taken should such a study be performed in the future. All of the in-fluid results discussed in Sect. 5.4 are for water with the following assumed properties: $\rho_f = 1000$ kg/m^3 and $\eta = 0.001$ Pa-s.

Following the approach of Cox [2011], the effect of mass uptake can be investigated by changing the beam density to mimic the effects of analyte sorption. However, it is important to note that by changing the density there is an implicit assumption that the added mass is uniformly distributed over the entire length of the beam. Moreover, by only altering the density it is assumed that the sorption does not significantly alter the stiffness of the system. Using Eq. (3-86), the frequency response curve may be plotted for the case of a harmonic support rotation as measured by the bending-deformation displacement. As an example, Fig. 5-1 shows the response curves for a 5x75x200 μm Si specimen using material parameters $C1 = 2.324$ km/sec and $C2 = 2$ (see Sect. 4.8.1), both before and after a 1% increase in the average beam density due to analyte sorption. Increase in the beam density results in a decrease in the resonant frequency, which is consistent with the anticipated result when the system is considered via a SDOF approximation (i.e., increase of mass will decrease resonant frequency).

As shown in Fig. 5-2, the reduction in resonant frequency is nearly a linear function of sorbed analyte (i.e., change in beam mass) for the various microcantilever geometries considered.

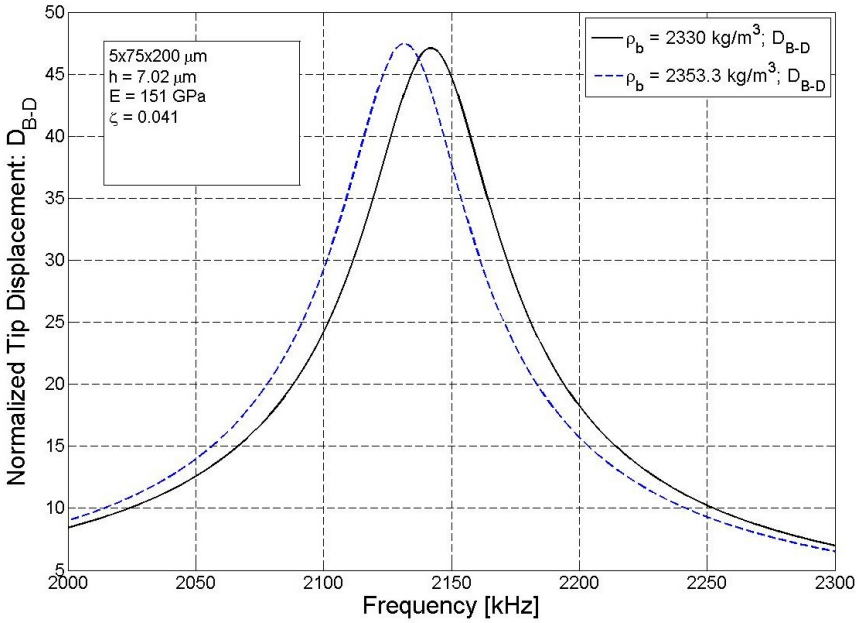

Figure 5-1: Shift in Frequency Response Curve Due to 1% Increase in Beam Density to Mirror the Effect of Analyte Sorption by a 5 x 75 x 200 μm Microcantilever-Based Sensor in Water: ρ_f = 1000 kg/m^3 and η = 0.001 Pa-s. Measured by the Bending-Deformation Displacement of the Response Due to a Harmonic Support Rotation

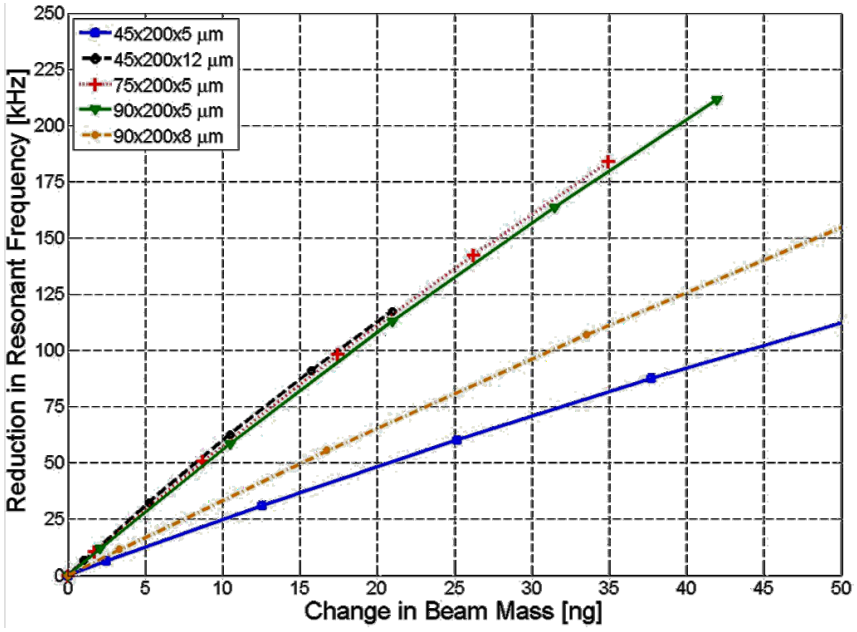

Figure 5-2: Theoretical Decrease in Resonant Frequency Due to Increase in Beam Density to Mirror the Effect of Analyte Adsorption by Microcantilever-Based Sensors of Various Geometries Sensor in Water: ρ_f = 1000 kg/m^3 and η = 0.001 Pa-s. Measured by the Bending-Deformation Displacement of the Response Due to a Harmonic Support Rotation

At larger values of sorbed mass, the change in resonant frequency can become nonlinear, but for the purpose of this work it is assumed that the added mass is sufficiently small to yield a linear system response (frequency shift). The associated $C1$ value for each geometry set is the best-fit value listed in Table 4-3, while the value of $C2 = 2$. Recalling the definition of mass sensitivity, Eq. (5-1), the S_m for each of the geometries can be obtained as the initial slope of each curve in Fig. 5-2 (assuming small mass uptake) as shown in Table 5-1.

Specimen Geometry [μm]	S_m **[Hz/pg]**
45x200x5	4.512
45x200x12	2.137
75x200x5	4.333
90x200x5	4.033
90x200x8	2.671

Table 5-1: Mass Sensitivities from Fig. 5-2

Note that the illustrative results of Fig. 5-2 suggest particular trends:

(1) There appears to be a large impact of device thickness on the mass sensitivity, i.e., the thicker (h_{nom} = 8, 12 μm) microcantilever has a lower mass sensitivity (~40-50% lower) than the corresponding specimens for h_{nom} = 5 μm. This is consistent with the results presented by Cox [2011] which indicate that decreasing the thickness can improve the mass sensitivity (although the captions to Figs. 4-16 and 4-17 of that reference appear to misstate the trend).

(2) Comparing the S_m of the specimens with h_{nom} = 5 μm for various widths (b = 45, 75, 90 μm) it is observed (from the similarity of the initial slopes of the curves) that the mass sensitivity is relatively insensitive to changes in beam width. (The results of Cox [2011] also show the same insensitivity to changes in width of an Euler-Bernoulli beam vibrating laterally in fluid.) However, if there exists a sensitive coating on one of the

larger cantilever (b x L) surfaces, then the chemical sensitivity, S_c, will have a linear dependence on the width (b) via the $V_{coating}$ factor in Eq. (5-6).

(3) Focusing on the curves of the 45x200x5 μm and the 90x200x5 μm specimens in Fig. 5-2 and the corresponding values listed in Table 5-1, it is observed that the mass sensitivity of the 90-μm-wide specimen (including the TB effects) is ~10% lower than the 45-μm-wide specimen, which possibly indicates the degree to which TB effects play a role in affecting the mass sensitivity of lateral-mode sensor geometries having large b/L ratios.

Similar calculations for mass sensitivity could be made for other specimen geometries, beam material properties, and fluid properties. While the comments above have focused on mass sensitivity, similar calculations could be performed for chemical sensitivity by implementing Eq. (5-6).

Using the results for resonant frequency and quality factor presented in earlier sections (Sects. 4-3 and 4-4) and the methodology for calculating mass sensitivity (and thus chemical sensitivity via Eq. (5-6)) in the previous paragraph, the impact of system parameters on LOD can be obtained by utilizing Eq. (5-9). As an example, a relative comparison of the LOD for the following pairs of devices will be performed: Case 1: 5 x 90 x 200 μm (Spec. 1) and 8 x 90 x 200 μm (Spec. 2), to show effect of h, and Case 2: 5 x 90 x 200 μm (Spec. 1) and 5 x 45 x 200 μm (Spec. 3), to show effect of b. For the purpose of this example it is assumed that the thickness of the chemically sensitive layer is constant for all devices. Similarly, the partition coefficient, K, is assumed to be the same among all devices because the coating material and medium (water) are assumed to be identical.

For the Case 1 comparison the ratio of LOD is obtained using Eqs. (5-6) and (5-9) as

$$\frac{LOD_1}{LOD_2} = \frac{f_{res,1}}{Q_1 S_{c1}} \frac{Q_2 S_{c2}}{f_{res,2}} = \frac{f_{res,1}}{f_{res,2}} \frac{Q_2}{Q_1} \frac{S_{m,2}}{S_{m,1}} \frac{(Kb_2 L_2 h_{coating,2})}{(Kb_1 L_1 h_{coating,1})}. \tag{5-10}$$

For the Case 1 comparison, it is noted that $b_1 = b_2$ and $L_1 = L_2$, resulting in the following ratio:

$$\frac{LOD_1}{LOD_2} = \frac{f_{res,1}}{f_{res,2}} \frac{Q_2}{Q_1} \frac{S_{m,2}}{S_{m,1}} = \left(\frac{2.4661 MHz}{2.3304 MHz} \right) \left(\frac{65.79}{46.27} \right) \left(\frac{2.671 Hz / pg}{4.033 Hz / pg} \right) = 0.997 \qquad (5\text{-}11)$$

i.e., the LOD for Specimen 1 (the thinner) device is effectively identical to that of Specimen 2 (the thicker device). (Note that the values of resonant frequency, quality factor, and mass sensitivity were obtained from Figs. 4-16 and 5-2 and Eq. 4-5). For the Case 2 comparison, note that b2 ≠ b3, L2 = L3, resulting in the ratio of LODs for Specimens 2 and 3:

$$\frac{LOD_2}{LOD_3} \propto \frac{f_{res,2}}{f_{res,3}} \frac{Q_3}{Q_2} \frac{S_{m,3}}{S_{m,2}} \frac{b_3}{b_2} = \left(\frac{2.3304 MHz}{1.3770 MHz} \right) \left(\frac{34.76}{65.79} \right) \left(\frac{4.512 Hz / pg}{2.671 Hz / pg} \right) \left(\frac{45 \mu m}{90 \mu m} \right) = 0.755 \qquad (5\text{-}12)$$

i.e., the LOD of Specimen 2 (the wider device) is ~25% lower (better) than for Specimen 3 (the narrower device). The results from the first comparison suggest that the LOD is essentially independent of the thickness of the base layer, while the second comparison indicates that the LOD decreases with an increase in width. Of course these conclusions have been made based on only two illustrative examples; to make more definitive statements a more thorough parametric study would need to be performed. Such an investigation, however, is deemed outside the scope of the present study. It is also important to note that the calculations and conclusions for both the mass sensitivity and the LOD are limited by the Stokes-type resistance assumptions (used to obtain to the resonant frequency and quality factor results) and will therefore become increasingly inaccurate at larger h/b values (i.e., as the thickness increases, the neglected pressure effects become increasingly important).

CHAPTER 6: SUMMARY CONCLUSIONS AND RECOMMENDATIONS

6.1 Summary

Motivated by discrepancies between Euler-Bernoulli beam models and experimental results, an improved analytical model has been developed for the in-fluid, lateral-mode vibration of a microcantilever-based sensor which incorporates not only the viscous fluid effects, but also the effects of shear deformation and rotatory inertia, i.e., " Timoshenko beam effects." Stokes-type fluid resistance assumptions were employed to derive the governing equations for in-fluid, Timoshenko beam vibrations and the associated BCs for the cases of a harmonic tip load and a harmonic support rotation. The resulting BVPs were non-dimensionalized and verified by reduction to existing BVPs for well-known special cases, including in-vacuum Euler-Bernoulli beams, in-fluid Euler-Bernoulli beams, and in-vacuum Timoshenko beams. The BVPs were solved analytically to obtain forced-vibration response, vibrational shapes, resonant frequencies, and quality factors, the latter associated with viscous dissipation in the surrounding fluid. Impact of the fluid resistance and Timoshenko parameters on the microcantilever response (primarily in terms of resonant frequency and quality factor) was investigated in detail for the two load types and the two methods of vibration detection of most interest in this study. More specifically, detailed results were generated and discussed for the following:

- harmonic tip loading with response monitored via total tip displacement,
- harmonic tip loading with response monitored via tip displacement due to bending,
- harmonic support rotation loading with response monitored via total tip displacement,
- harmonic support rotation loading with response monitored via tip displacement due to bending-deformation.

Although the new theoretical solutions apply to multi-modal system response for in-plane vibration, the system's first-mode lateral response was the primary focus of the study for all

loading/detection types listed above. The frequency response curves were provided for tip displacement from which the resonant frequencies were obtained. Then, the quality factor results were obtained by employing the 3-dB bandwidth method to the theoretical frequency response curves for both loading cases and for both methods of measurement. In addition to the frequency response curves, the time-dependent vibrational shapes were plotted for both types of loading as monitored by the total, shear and bending (or bending-deformation) displacements. While there is some variability in the vibrational shape over a complete cycle, the envelope for the beam shape appeared small enough to justify future consideration of a SDOF model using the in-vacuum shape of the Timoshenko beam. Additionally, the theoretical results were compared to the experimental data for resonant frequency and quality factor. Finally, while the focus of the current work was not the optimization of microcantilever-based sensor geometry to maximize sensor performance (e.g., sensitivity and limit of detection (LOD)), some sample calculations were performed to demonstrate how one may quantify the effect that changing the system parameters may have on the mass and chemical sensitivities as well as LOD, while incorporating the effects of fluid and Timoshenko beam parameters. The latter are expected to be important for those geometries that are most ideal for lateral-mode sensor operation, i.e., large b/L ratios. The derivation of the expressions for sensitivities and LOD, as well as the presentation of illustrative results, was included to show how the improved accuracy of the theoretical resonant frequency and quality factor predictions, furnished by the current in-fluid TB model, may be extended to improved estimates of sensitivities and LOD.

6.2 Conclusions

The following conclusions are based on the research presented in this work.

1. Work based on EB models [e.g., Heinrich et al., 2010a,b] has indicated that lateral-mode microcantilevers show promise in liquid-phase sensing applications, especially for those

geometries that are short and wide (large b/L). However, the advantages associated with these geometries cannot continue indefinitely as b/L increases due to the violation of the underlying Euler-Bernoulli hypotheses. For example, results from EB theory indicate that the resonant frequency is linear in b/L^2 and that the quality factor is linear in $b^{1/2}/L$ When including the Timoshenko beam effects, however, the current study shows that the linearity in these relationships eventually breaks down. It was observed that increasing the TB parameters reduces f_{res} and Q below the values predicted by EB theory. As a result, the trends in f_{res} and Q predicted by theoretical TB theory begin to "drop-off" from the EB predictions at high b/L and this type of behavior is consistent with the trends seen in experimental data.

2. Comparisons with limited experimental data show that the TB model yields in-water f_{res} predictions that are 31-52% more accurate than the predicted values of Euler-Bernoulli models for lateral-mode cantilevers having the highest b/L ratios. The more accurate frequency estimates are smaller than the EB results and thus represent the aforementioned "drop-off" trend in frequency. A similar conclusion applies to comparisons among the predicted values of quality factor Q according to the TB model and the existing BE model, and existing experimental data. For the least slender specimens the TB effects provide predictions of Q that are 12-26% more accurate than the theoretical values from EB models. (These improvements in accuracy over the EB model were based on using a "textbook" value of $\sqrt{E/kG} = 2$ which corresponds to pure Si.)

3. Over the parameter ranges r = [0, 0.2], $\sqrt{E/kG}$ = [0, 3] and ζ =[0, 0.2], the impact of the Timoshenko effects on f_{res} is that they may cause a reduction of up to 23% in the resonant frequency. This value occurs at the largest values of r and $\sqrt{E/kG}$ in the specified ranges and is relatively insensitive to the value of fluid resistance parameter. Similarly, the influence of the Timoshenko effects over the specified ranges of Timoshenko parameters

is to cause a reduction of up to 23% in the quality factor, with the maximum reduction occuring at the largest values of r and $\sqrt{E/kG}$. The percent reduction in Q is relatively insensitive to ζ over the range ζ =[0.05, 0.2].

4. While the TB model tends to provide more accurate theoretical values for f_{res} and Q than the EB theory, for $b/L \leq 0.15$ the EB theory provides f_{res} and Q results within 2% of the TB model. (This conclusion is based on Figs. 4-16 and 4-19 and the assumption that $\sqrt{E/kG} \leq 3$, which is satisfied by all isotropic materials and by many anisotropic materials, inclusing silicon. Also, this accuracy level is relatively insensitive to the value of the fluid resistance parameter.) Thus, Timoshenko beam effects may be considered negligible if $b/L \leq 0.15$, i.e., if the length-to-width ratio is roughly 7 or higher.
5. For small values of the fluid resistance parameter ($\zeta < 0.2$), f_{res} and Q are independent of load type (tip force or support rotation) and measurement method (monitoring the total tip deflection or that associated with bending deformation only). However, despite the fact that f_{res} and Q are load-independent, the shape and the peak amplitude of the frequency response curves *are* influenced by the type of loading and the measurement method.
6. For larger values of the fluid resistance parameter, i.e., $\zeta > 0.2$, f_{res} and Q exhibit a dependence on the detection scheme. For example, for the case of a harmonic support rotation and ζ =2, numerical results from the present study indicate that f_{res} as measured by the bending-deformation tip displacement ($D_{B\text{-}D}$) may be up to 10% larger than its total tip deflection counterpart (D_T), while Q measured by $D_{B\text{-}D}$ may be up to 25% smaller than its D_T counterpart. These differences appear to be due to the fact that the rigid motion from the harmonic support rotation and the beam response are out-of-phase, becoming increasingly so at higher fluid resistance values. Also, preliminary results indicate that

there may exist a similar dependence of resonant frequency and quality factor on the type of load at large values of the fluid resistance parameter.

7. For both load types considered, it was observed that a change between D_T and $D_{B\text{-}D}$ response curves occurs when transitioning from the fundamental mode to mode 2. In particular, for mode 2 the amplitude of the beam's $D_{B\text{-}D}$ resonant response is larger than that obtained for the D_T response for both loading cases. This differs from the mode-1 response in which the D_T amplitude exceeds that of the $D_{B\text{-}D}$ response, thus suggesting potential advantages to mode-2 operation for sensor designs that employ a motion-detection method based on monitoring the bending strain. This may be especially true for systems with higher values of fluid resistance and Timoshenko parameters.
8. A new approximate analytical equation for quality factor Q has been established in terms of the fundamental system parameters (beam dimensions; Young's modulus, shear modulus, and density of the beam material; and density and viscosity of the fluid). This equation is within 2.6% of the "exact" TB theoretical results obtained herein for a Timoshenko beam vibating laterally with Stokes fluid resistance. This accuracy level was determined over the following practical ranges of normalized system parameters: $\zeta = (0, 0.05)$, $r = (0, 0.2)$ and $\sqrt{E/kG} = (0, 3)$. Accuracy of the formula is expected to be good for even higher ζ values that may be encountered.
9. Based on limited illustrative examples for estimating lateral-mode chemical sensor performance, the following dependence of sensor performance on cantilever dimensions has been observed:
    a. Mass sensitivity (S_m) decreases with an increase in device thickness and this dependence appears to be approximately $S_m \sim 1/h$. The dependence of S_m on beam width is minimal. For example, the mass sensitivity of a 90-μm-wide specimen (including the TB effects) was only ~10% lower than that of the 45-

μm-wide specimen, which possibly indicates the degree to which the higher-order TB effects may influence the mass sensitivity of lateral-mode microcantilever-based sensors.

b. If there exists a sensitive coating on one of the larger cantilever (b x L) surfaces, then the chemical sensitivity, S_c, will have an approximately linear dependence on the width (b) and coating thickness h_c via the coating volume factor, and will be approximately inversely related to cantilever thickness h. (This follows from the dependence of S_m on beam dimensions as noted above.)

c. For the case of a lateral-mode sensor operating within an oscillator feedback loop configuration, the limit of detection (LOD) is approximately independent of thickness of the cantilever thickness (without coating). However, the dependence of LOD on width b appears to be important and indicates that wider devices yield improved LODs. For example, when the device width was doubled from 45 μm to 90 μm, the LOD decreased (improved) by 25%.

Note that, for all thickness sets, the TB theory provides improved accuracy compared to the EB model; however, both theories become less effective as the thickness increases, a likely consequence of the limitations of the Stokes-type fluid resistance assumption. As the thickness increases, the pressure effects on the narrower sides of the beam may become increasingly important and no longer negligible. The importance of this effect has been pointed out recently by other researchers [Brumley et al., 2010; Cox et al., 2012]. Therefore, one should keep in mind that the above conclusions should be viewed within the context of the Stokes fluid resistance assumption that has been employed in the present study.

6.3 Recommendations for Future Work

The results of the present research suggest several logical extensions that may constitute important future studies. These might include the following:

1. In comparison with experimental data, the present model tends to overpredict resonant frequencies and in-fluid quality factors, especially (a) at higher *b/L* ratios and (b) for thicker specimens. Item (a) may most likely be addressed by incorporating the support compliance (which is assumed to be more significant as the sensor geometry becomes shorter and wider, paralleling the Timoshenko trends). Adding this effect will result in lower calculated resonant frequencies for the less slender beams, due to the reduced overall stiffness of the system caused by support flexibility, and a corresponding change in Q. To address item (b), the recent results of Brumley et al. [2010] and Cox et al. [2012] could be incorporated into the present model to account for the dependence of fluid effects on the aspect ratio of the cross section by introducing a more accurate hydrodynamic function than that used in the present study.
2. The inclusion of the structural effects of a sensitive coating (e.g., density, elasticity, viscoelasticity) would also provide a more complete model. While the viscoelastic effects are typically negligible for in-liquid applications (due to the large dissipation in the liquid), the viscoelastic effects of the coating may be significant for the in-gas case [e.g., Lochon et al., 2005]. To the author's knowledge there has been no effort to apply Timoshenko beam theory to coated beams and account for the viscoelasticity of the coating for either static-mode or dynamic-mode applications. Such a solution may be applicable to, for example, large-aspect ratio, laminated structural glass fins.
3. An analytical formula for Q has been established in the present study for a lateral-mode Timoshenko beam vibrating in a viscous fluid. Future work may include an

analogous effort to derive a corresponding analytical formula for the resonant frequency. Such an end may be achievable by introducing a SDOF model based on the results of the present study, thereby leading to a relatively simple formula to give accurate estimates of resonant frequency without the complications of the partial differential equation approach utilized in the present study.

4. Finally, the change in the nature of the frequency response curves from mode-1 to mode-2, as indicated by the relative sizes of the amplitudes of the total and bending (or bending-deformation) displacements, is interesting and a potential topic for future investigation. Such studies may yield results that could prove beneficial in sensing applications.

REFERENCES

Abbasion,S., Rafsanjani,A., Avazmohammadi, R., and Farshidianfar, A., "Free vibration of microscaled Timoshenko beams," Applied Physics Letters, Vol. 95, 2009, pp.143122 – 143122-3.

Abramovich, H., and Elishakoff, I., "Influence of shear deformation and rotatory inertia on vibration frequencies via Love's equations," *Journal of Sound and Vibration*, 1990, Vol. 137, 3, pp. 516-522.

Barnes, J., Stephenson, R., Welland, M., Gerber, C., and Gimzewski, J., "Photothermal spectroscopy with femtojoule sensitivity using a micromechanical device, *Nature,* Vol. 372, No. 6501, 1994, pp. 79-81.

Basak, S., Raman, A., and Garimella, S., "Hydrodynamic loading of microcantilevers vibrating in viscous fluids," *Journal of Applied Physics*, Vol. 99, 2006, pp. 114906 – 114906-10.

Beardslee, L.A., Josse, F., Heinrich, S.M., Dufour, I., and Brand, O., "Geometrical Considerations for the Design of Liquid-Phase BioChemical Sensors Using a Cantilever's Fundamental In-Plane Mode," *Sensors and Actuators B*, 2012, pp. 7-14.

Beardslee, L.A., Truax, S., Su, J.-J., Heinrich, S.M., Josse, F., Brand, O., "On the Relative Sensitivity of Mass-Sensitive Chemical Microsensors," *Proc., Transducers '11, 16th International Conference on Solid-State Sensors, Actuators and Microsystems*, Beijing, China, June 5-9, 2011, 5 pp.

Beardslee, L.A., Addous, A.M., Demirci, K.S., Heinrich, S.M., Josse, F., and Brand, O., "Geometrical Optimization of Resonant Cantilevers Vibrating in In-Plane Bending Mode," *Proceedings, IEEE Sensors 2010 Conference*, Waikoloa, Hawaii, November 1-4, 2010a, pp. 1996-1999.

Beardslee, L., Addous, A., Heinrich, S., Josse, F., Dufour, I., and Brand, O., "Thermal Excitation and Piezoresistive Detection of Cantilever In-Plane Resonance Modes for Sensing Applications," *Journal of Microelectromechanical Systems*, Vol. 19, No. 4, 2010b, pp. 1015-1017.

Beardslee, L.A., Demirci, K.S., Luzinova, Y., Mizaikoff, B., Heinrich, S.M., Josse, F., and Brand, O., "Liquid-Phase Chemical Sensing Using Lateral Mode Resonant Cantilevers," *Analytical Chemistry***,** Vol. 82, 2010c, pp. 7542-7549.

Beardslee, L.A., Demirci, K.S., Luzinova, Y., Su, J.J., Mizaikoff, B., Heinrich, S., Josse, F., and Brand, O., "In-Plane Mode Resonant Cantilevers as Liquid-Phase Chemical Sensors with PPB Range Limits of Detection," *Proc., Hilton Head Workshop 2010: A Solid-State Sensors, Actuators and Microsystems Workshop*, Hilton Head, SC, June 6-10, 2010d, 4 pages.

Boisen, A., Dohn, S., Keller, S. Schmid, S. and Tenje M., "Cantilever-like micromechanical sensors," *Reports on Progress in Physics*, Vol. 74, February 2011, 30 pages.

Brumley, D., Willcox, M., and Sader, J., "Oscillation of cylinders of rectangular cross section immersed in fluid," *Physics of Fluids*, Vol. 22, 2010, pp. 052001-052001-15.

Chen G., Warmack, R., Thundat, T., Allison, D., and Hunag, A., "Resonance response of scanning force microscopy cantilevers," *Applied Physics Letters*, Vol. 65, No. 8, 1994, pp. 2532 - 2537.

Cowper, G., "The Shear Coefficient in Timoshenko's Beam Theory," *ASME Journal of Applied Mechanics*, Vol. 33, 1966, pp. 335-340.

Cox, R., Josse, F., Heinrich, S., Brand, O., and Dufour, I., "Characteristics of Laterally Vibrating Resonant Microcantilevers in Viscous Liquid Media," *Journal of Applied Physics*, Vol. 111, January, 2012 pp. 014907 - 014907-14.

Cox, R., "*Theoretical Analysis of Laterally Vibrating Microcantilever Sensors in a Viscous Liquid Medium*," Doctoral Dissertation, May 2011, Marquette University, Wisconsin, USA.

Cox, R., Josse, F., Wenzel, M., Heinrich, S.M., and Dufour, I., "A Generalized Model of Resonant Polymer-Coated Microcantilevers in Viscous Liquid Media," *Analytical Chemistry*, Vol. 80, 2008, pp. 5760-5767.

Cox, R., Wenzel, M., Josse, F., Heinrich, S.M., and Dufour, I., "Generalized Characteristics of Resonant Polymer-Coated Microcantilevers in Viscous Liquid Media," *Proceedings, IEEE International Frequency Control Symposium (FCS) 2007*, Geneva, Switzerland, May 29-June 1 2007, 6 pages.

Dong, S., Apldogan, C., and Taciroglu, E., "Much ado about shear correction factors in Timoshenko beam theory," *International Journal of Solids and Structures*, Vol. 47, 2010, pp. 1651-1665

Dufour, I., Josse, F., Heinrich, S., Lucat, C., Ayela, C., Menil, F., and Brand, O., "Unconventional uses of microcantilevers as chemical sensors in gas and liquid media," *Sensors and Actuators B*, Vol. 170, July 2010, pp. 115-121.

Dufour, I., Josse, F., and Heinrich, S., "Theoretical Analysis of Strong-Axis Bending Mode Vibrations for Resonant Microcantilever (Bio)Chemical Sensors in Gas or Liquid Phase" *Journal of Micromechanical Systems*, Vol. 16, No. 1, 2007a, 44-49.

Dufour, I., Lochon, F., Heinrich, S.M., Josse, F., and Rebière, D., "Effect of Coating Viscoelasticity on Quality Factor and Limit of Detection of Microcantilever Chemical Sensors," *IEEE Sensors Journal*, Vol. 7, No. 2, February, 2007b, pp. 230-236.

Dufour, I., Heinrich, S.M., and Josse, F., "Strong-Axis Bending Mode Vibrations for Resonant Microcantilever (Bio)Chemical Sensors in Gas or Liquid Phase," *Proceedings, 2004 IEEE International Ultrasonics, Ferroelectrics, and Frequency Control 50th Anniversary Joint Conference*, 6 pp., Montreal, Canada, August 24-27, 2004.

Ekinci, K., Yakhot, V., Rajauri, S., Colosqui, C., and Karabacak, D., "High-frequency nanofluidics: a universal formulation of the fluid dynamics of MEMS and NEMS," *Lab on a Chip*, Vol. 10, July 2010, pp. 3013-3025.

Fadel, L., Dufour, I., Lochon, F., and Francis, O., "Signal-to-noise ratio of resonant microcantilever type chemical sensors as a function of resonant frequency and quality factor," *Sensors and Actuators B*, Vol. 121, January 2004, pp. 73-77.

Feynman, R., "There's Plenty of Room at the Bottom," *Engineering and Science,* 1960, 36 pp.

Finot, E., Passian, A., and Thundat, T., "Measurement of Mechanical Properties of Cantilever Shaped Materials," *Sensors*, Vol. 8, 2008, pp. 3497-3541.

Ghatkesar, M.K., Braun T., Barwich, V., Ramseyer, J., Gerber, C., Hegner, M., and Lang, H., "Resonating modes of vibrating microcantilevers in liquid" *Applied Physics Letters*, Vol. 92, 2008, pp. 92-94.

Ghugal, Y., and Sharma, R., "A refined shear deformation theory fro flexure of thick beams," *Latin American Journal of Solids and Structures*, Vol. 8, 2010, pp. 183-195.

Ghugal, Y., and Sharma, R., "A Hyperbolic Shear Deformation Theory for Flexure and Vibration of Thick Isotropic Beams," *International Journal of Computational Methods*, Vol. 6, 2009, pp. 585-604.

Green, C., and Sader, J., "Small amplitude oscillations of a thin beam immersed in a viscous fluid near a solid surface," *Physics of Fluids,* Vol. 17, 2005, 12 pages.

Hagleitner, C., Lange, D., Hierlemann, A., Brand, O., and Baltes, H., "CMOS Single-Chip Gas Detection System Comprising Capacitive, Calorimtetric and Mass-Sensitvie Microsensors," *IEEE Journal of Solid State Circuits,* Vol. 37, 12, 2002, pp. 1867-1878.

Heinrich, S.M., Maharjan, R., Beardslee, L., Brand, O., Dufour, I., and Josse, F., "An Analytical Model for In-Plane Flexural Vibrations of Thin Cantilever-Based Sensors in Viscous Fluids: Applications to Chemical Sensing in Liquids," *Proceedings, International Workshop on Nanomechanical Cantilever Sensors*, Banff, Canada, May 26-28, 2010a, 2 pp.

Heinrich, S.M., Maharjan, R., Dufour, I., Josse, F., Beardslee, L.A., and Brand, O., "An Analytical Model of a Thermally Excited Microcantilever Vibrating Laterally in a

Viscous Fluid," *Proceedings and Poster Session, IEEE Sensors 2010 Conference*, Waikoloa, Hawaii, November 1-4, 2010, pp. 1399-1404. 2010b.

Hopcroft, M., Nix, W., and Kenny, T., "What is the Young's Modulus of Silicon?" *Journal of Microelectromechanical Systems*, Vol. 19, 2010, pp. 229-238.

Horng, T., "A Modal Superposition Method for Vibration Responses of Atomic Force Microscope Cantilevers Using the Timoshenko Beam Model," *Proceedings*, *International Conference on Consumer Electronics, Communications and Networks (CECNet),* XianNing, Taiwan, April 16-18 2011, pp. 3831-3835.

Horng, T., "Analyses of vibration responses on nanoscale processing in a liquid using tapping-mode atomic force microscopy," *Applied Surface Science,* Vol. 256, 2009, pp. 311-317.

Hsu, J., Lee, H. and Chang, W., "Flexural vibration frequency of atomic force microscope cantilevers using the Timoshenko beam model," *Nanotechnology*, Vol. 18, 2007.

Huang, T., and Kung, C., "New Tables of Eigenfunctions Representing Normal Modes of Vibration of Timoshenko Beams," *Developments in Theoretical and Applied Mechanics*, Vol. 1, 1963, pp. 59-71.

Huang, T., "The Effect of Rotatory Inertia and of Shear Deformation on the Frequency and Normal Mode Equations of Uniform Beams with Simple End Conditions," *Journal of Applied Mechanics,* 1961, 579-584.

Hutchinson, J., "Shear Coefficients for Timoshenko Beam Theory," *Journal of Applied Mechanics*, Vol. 68, January 2001, pp. 87-92.

Kruszewski, E., "Effect of Transverse Shear and Rotatory Inertia on the Natural Frequency of a Uniform Beam," *National Advisory Committee for Aeronautics Technical Note 1909*, Langley Aeronautical Laboratory, Langley Va., 1949.

Lavrik, N., Sepaniak, M., and Datskos, G., "Cantilever Transducers as a Platform for Chemical and Biological Sensors," *Review of Scientific Instruments*, Vol. 75, 2004, pp. 1ff.

Lee, H and Chang, W., "Effects of Damping on the Vibration Frequency of Atomic Force Microscope Cantilevers Using the Timoshenko Beam Model," *Japanese Journal of Applied Physics,* Vol 48, 2009.

Li, X. and Lee, D., "Integrated microcantilevers for high-resolution sensing and probing," *Measurement Science and Technology*, Vol. 23, December 2011, 40 pages.

Lin, S., "Effective dampings and frequency shifts of several mdoes of an inclined cantilever vibrating in viscous fluid," *Precision Engineering,* Vol. 34, 2010, pp. 320-326.

Lochon, F., Dufour, I., Rebière, D., Sampath, U., Heinrich, S.M., and Josse, F., "Effect of Viscoelasticity on Quality Factor of Microcantilever Chemical Sensors: Optimal Coating Thickness for Minimum Limit of Detection" *Proceedings of IEEE Sensors 2005*, pp. 265-268, 2005

Mahdavi, M., Farshidianfar, A., Tahani, M., Mahdavi, S., and Dalir, H., "A more comprehensive modeling of atomic force microscope cantilever," *Ultramicroscopy*, Vol. 109, 2008 pp. 54-60.

MATLAB version 7.10.0. Natick, Massachusetts: The MathWorks Inc., 2010.

Narducci, M., Figueras, E., Lopez, M., Gracia, I., Fonseca, L., Santander, J., and Cane, C., "A High Sensitivity Silicon Microcantilever Based Mass Sensor," *IEEE Conference 2008*, 2008, pp. 1127-1130.

Naeli, K., and Brand, O., "Dimensional considerations in achieving large quality factors for resonant silicon cantilevers in air," *Journal of Applied Physics,* Vol. 105, 2009, 10 pp.

Rensburg, N., and Merwe, A., "Natural frequencies and modes of a Timoshenko beam," *Wave Motion*, Vol. 40, 2006, pp. 58-69.

Renton, J., "Generalized beam theory applied to shear stiffness," *International Journal of Solid Structures*, Vol. 27, No. 15, 1991, pp. 1955-1967.

Sader, J., "Frequency response of cantilever beams immersed in viscous fluids with applications to the atomic force microscope," *Journal of Applied Physics*, Vol 84, No 1, 1998, pp. 64-76.

Sampath, U., Heinrich, S.M., Josse, F., Lochon, F., Dufour, I., and Rebière, D., "Study of Viscoelastic Effect on the Frequency Shift of Microcantilever Chemical Sensors," *IEEE Transactions on Ultrasonics, Ferroelectrics, and Frequency Control*, Vol. 53, No. 11, 2006, pp. 2166-2173.

Schaffer, T., Cleveland, J., Ohnsorge, F., Wlaters, D, and Hansma, P., "Studies of vibrating atomic force microscope cantilevers in liquid," *Journal of Applied Physics,* Vol. 80, 7, 1996, pp. 3622-3627.

Stephen, N., "The second spectrum of Timoshenko beam theory – Further assessment," Journal of Sound and Vibration, Vol. 292, 2006, pp. 372-389.

Stokes, G., "On the Effects of the Internal Friction of Fluids on the Motion of Pendulums" *Transactions of the Cambridge Philosophical Society*, vol. 9, pp 8-106, 1851.

Thundat, T., Wachter, E., Sharp, S., and Warmack, R., "Detection of mercury vapor using resonating microcantilevers," *Applied Physics Letters*, Vol. 66, No. 13, 1995, pp. 1695-1697.

Thundat, T., Warmack, R., Chen G., and Allison, D., "Thermal and ambient-induced deflections of scanning force microscope cantilevers," *Applied Physics Letters*, Vol. 64, No. 21, 1994, pp. 2894-2896.

Timoshenko, S., "On the transverse vibrations of bars of uniform cross sections," *The London, Edinburgh and Dublin Philosophical Magazine and Journal of Science*. Vol 43, 1922, pp. 125-131.

Timoshenko, S., "On the correction for shear of the differential equation for transverse vibrations of prismatic bars," *The London, Edinburgh and Dublin Philosophical Magazine and Journal of Science*. Vol 41, 1921, pp. 744-746.

Trimmer, W., Micromechanics and MEMS: Classic and Seminal Papers to 1990,Institute of Electrical and Electronics Engineers Inc. Press, New York, 1997.

Van Eysden, C and Sader, J., "Frequency response of cantilever beams immersed in viscous fluids with applications to the atomic force microscope: Arbitrary mode order," *Journal of Applied Physics,* Vol. 101, 2007.

Van Eysden, C and Sader, J., "Small amplitude oscillations of a flexible thing lade in a viscous fluid: Exact analytical solution," *Physics of Fluids,* Vol. 18, 2006.

Vancura, C., Dufour, I., Heinrich, S., Josse, F., and Hierlemann, A., "Analysis of Resonating Microcantilevers Operating in a Viscous Liquid Environment," *Sensors and Actuators A*, Vol. 141, No. 1, January 2008, pp. 43-51.

White, F., Viscous Fluid Flow, 3rd ed., ch. 3, McGraw-Hill, 2006.

Weaver, W., Timoshenko, S., and Young, D., Vibration Problems in Engineering 5th ed, John Wiley and Sons, New York, 1990.

Wenzel, M.J., Josse, F., Heinrich, S.M., Yaz, E., and Datskos, P.G., "Sorption-Induced Static Bending of Microcantilevers Coated with Viscoelastic Material," *Journal of Applied Physics*, Vol. 103, Paper No. 064913, 2008, 11 pages.

Zhu, Q., "Microcantilever Sensors in Biological and Chemical Detections: A Review," *Sensors and Transducers Journal*, Vol. 125, No. 2, February 2011, pp. 1-12.

APPENDIX A: MATLAB VERIFICATION OF IN-FLUID TIMOSHENKO BVP USING MATLAB SOLVER BVP4C

Reduction of Order and Application of MATLAB solver bvp4c

The following derivation is for the application of bvp4c solver for numerical verification to the in-fluid Timoshenko BVP. Since the MATLAB bvp4c function requires the input of first order ODEs, reduction of order is applied to the coupled, second order ODEs. In the following derivation the harmonic tip load is taken as the illustrative case and the harmonic support rotation is obtained similarly with the necessary changes to the BCs.

Recall the coupled, second order ODE's from Eqs. (3-45) and (3-46):

$$s^2\Phi'' + \bar{V}' - \left\{1 - r^2 k_3\right\}\Phi = 0\,, \tag{A-1}$$

$$\bar{V}'' + k_3\bar{V} - \Phi = 0\,. \tag{A-2}$$

The associated BCs for a harmonic tip load from Eq. (3-35):

$$\bar{V}(0) = 0\,, \tag{A-3a}$$

$$\Phi(0) = 0\,, \tag{A-3b}$$

$$\Phi'(1) = 0\,, \tag{A-3c}$$

$$\frac{\bar{V}'(1) - \Phi(1)}{s^2} = \bar{F}_0\ . \tag{A-3d}$$

Now applying a redefinition of terms for reduction of order:

$$z_1 = \bar{V} \tag{A-4}$$

$$z_2 = z_1' = \bar{V}' \tag{A-5}$$

$$z_3 = \Phi \tag{A-6}$$

$$z_4 = z_3' = \Phi' \tag{A-7}$$

Applying Eqs. (A1-4) through (A1-7) to Eqs. (A1-1) and (A1-2) results in the coupled, first order ODE's (i.e., the reduced equations) as follows:

$$s^2 z_4' + z_2 - \left(1 - r^2 k_3\right) z_3 = 0 \rightarrow z_4' = -\frac{1}{s^2} z_2 + \frac{\left(1 - r^2 k_3\right)}{s^2} z_3 \tag{A-8}$$

$$z_2' + k_3 z_1 - z_4 = 0 \rightarrow z_2' = -k_3 z_1 + z_4 \tag{A-9}$$

The associated BCs in terms of the newly defined variables become:

$$\mathrm{z}_1(0) = 0 \tag{A-10}$$

$$\mathrm{z}_3(0) = 0 \tag{A-11}$$

$$z_4(1) = 0 \tag{A-12}$$

$$\frac{\mathrm{z}_2(1) - z_3(1)}{s^2} = \bar{F}_0 \tag{A-13}$$

Finally, (A1-10) through (A1-13) are rewritten using the nomenclature employed in the following MATLAB bvp4c solver:

$$va(1) \equiv \mathrm{z}_1(0) = 0 \tag{A-14}$$

$$va(3) \equiv \mathrm{z}_3(0) = 0 \tag{A-15}$$

$$vb(4) \equiv z_4(1) = 0 \tag{A-16}$$

$$vb(2) - vb(3) - 1 = 0 \tag{A-17}$$

Note that the result Sxint(1,:) will report the values associated with z_1, (i.e., $\bar{V}$), and Sxint(3,:) will report the values associated with z_3, (i.e., Φ). The following general overview of reduction of order for the bvp4c solver will serve as clarification for notation regarding the BCs. Take the case of 1st order ODEs of the form:

$$v' = f(x, v).$$

They can be interpreted as (if, say there are two 1st order equations in two unknowns *v*(1) and *v*(2)):

$$\hat{v}' = \hat{f}(x, v);$$

or, more explicitly as:

$$\begin{Bmatrix} \dfrac{dv(1)}{dx} \\ \dfrac{dv(2)}{dx} \end{Bmatrix} = \begin{Bmatrix} f_1[x, v(1), v(2)] \\ f_2[x, v(1), v(2)] \end{Bmatrix}.$$

The BC's for the above situation are:

$$bc[v(a), v(b)] = 0.$$

Again, the BCs can be interpreted as (again, for two 1st order equations in two unknowns y(1) and y(2)):

$$\hat{bc}[\hat{v}(a), \hat{v}(b)] = \hat{0},$$

or

$$\hat{bc}[y(1) \text{ at a}, y(2) \text{ at a}, y(1) \text{ at b}, y(2) \text{ at b}] = \hat{0},$$

or

$$\begin{Bmatrix} bc1[v(1) \text{ at a}, v(2) \text{ at a}, v(1) \text{ at b}, v(2) \text{ at b}] \\ bc2[v(1) \text{ at a}, v(2) \text{ at a}, v(1) \text{ at b}, v(2) \text{ at b}] \end{Bmatrix} = \begin{Bmatrix} 0 \\ 0 \end{Bmatrix}.$$

Note that the function handle that computes the residual is in the boundary conditions. For two-point boundary value conditions of the form *bc*(*v*(a),*v*(b)), bcfun can have either form:

res = bcfun(*v*a,*v*b)

or

res = bcfun(*v*a,*v*b,parameters)

where:

*v*a and *v*b are column vectors corresponding to *v*(a) and *v*(b) parameters is a vector of unknown parameters and the output *res* is a column vector.

MATLAB Code Using bvp4c Solver:

```
% This program uses the bvp4c ODE solver to provide a numerical soln to the
% in-fluid Timoshenko beam theory
% Date Modified: 01/30/2012
% Modified by: Joshua Schultz
%
function bvp4TB
xlow=0; xhigh=1;

% Qty of values in [] must equal number of equations
solinit = bvpinit(linspace(xlow,xhigh,300000),[0 0 0 1]);

% Solution using bvp4c
% bvp4c requires (ODE definition, BC definition and mesh, guess for soln
sol = bvp4c(@bvp4ode,@bvp4bc,solinit);
xint = linspace(xlow, xhigh);
Sxint = deval(sol,xint);
hold on;
grid on;
plot(xint,Sxint(1,:)/max(Sxint(1,:)),'r')
%-------------------------------------
% ODE definition routine
function dydx = bvp4ode(x,y)
% Input Values
R = 0.1;
S = 0.2;
LAMBDA = 1.5;
ZETA = 0.2;

% Calculation of k values, the k values are coefficients on the TB ODE's
% k1 = LAMBDA^3*(R^2+S^2)*((LAMBDA+ZETA)-1i*ZETA);
% k2 = -LAMBDA^3*(LAMBDA+(1-1i)*ZETA)*(1-R^2*S^2*LAMBDA^3*(LAMBDA+(1-
1i)*ZETA));
k3 = (S^2*LAMBDA^2*((LAMBDA*(LAMBDA+ZETA)-1i*ZETA*LAMBDA)));

dydx = [y(2) -k3*y(1)+y(4) y(4) ((1-R^2*k3)/(S^2))*y(3)-(1/S^2)*y(2)];
%-------------------------------------
% Boundary value definition routine
function res = bvp4bc(ya,yb)
res = [ya(1) ya(3) yb(4) yb(2)-yb(3)-1];
```

Verification of current in-fluid, Timoshenko results for $V_{B\text{-}D}$ by Using bvp4c Routine:

Having established the merit of using $\bar{V}_{B-D}$ as an output that is proportional to the measured strain of the experimental devices employed by colleagues at Georgia Tech [Beardslee et al., 2010a, b], the existing programs based on the in-fluid TB BVP have been edited to provide output in terms of $\bar{V}_{B-D}$. However, these results need to be verified by an independent check. As a result, the preceding program, "bvp4cTB.m" is used to determine the results for displacement terms V and Φ, based on $\bar{V}_{B-D}$.

Using the results for $\bar{V}$ and Φ generated by MATLAB solver bvp4c, the following derivation shows the process to obtain the results based solely on the deformation due to bending displacement ($\bar{V}_{B-D}$).

Recall that the preceding bvp4c solver determines: $\bar{V}(\xi)$ and $\Phi(\xi) = \bar{V}_B'(\xi)$.

Recalling the derivation for the magnitude of $\bar{V}_{B-D}$ in Ch 3, it is anticipated that the integral of Φ will be needed. This is obtained explicitly in the in-fluid, Timoshenko MATLAB programs by the analytical integration of the equations. However, the results can also be checked numerically with the bvp4c and trapz functions.

Thus, $\bar{V}_B(\xi)$ is obtained by taking the numerical (trapezoidal rule) integration:

$$\bar{V}_B(1) = \int_0^1 \Phi(\xi) d\xi .$$

Recall, the results for the displacement due to total bending can be obtained as

$$\frac{\bar{v}_B(1,\tau)}{\theta_0} = \frac{\bar{V}_B(1)}{\theta_0} e^{i\tau} ,$$

and the result for rigid displacement (recalling basic geometry) is

$$\frac{\bar{v}_R(1,\tau)}{\theta_0} = e^{i\tau} .$$

Then the solution for the displacement due solely to bending is:

$$\frac{\bar{v}_{B-D}(1,\tau)}{\theta_0}=\frac{\bar{v}_B(1,\tau)}{\theta_0}-\frac{\bar{v}_R(1,\tau)}{\theta_0}=\frac{\bar{V}_B(1)}{\theta_0}e^{i\tau}-e^{i\tau}=\left(\frac{\bar{V}_B(1)}{\theta_0}-1\right)e^{i\tau}.$$

Where the magnitude of the spatial dependence $\left|\frac{\bar{V}_B(1)}{\theta_0}-1\right|$ can be compared to Eq. (3-88).

MATLAB Results and Comparison:

The preceding derivation was used to update the bvp4c program and provide a point check of previous results from TB EOM MATLAB files. The following is a typical check based on specified parameters.

%% Inputs: (bvp4TBYbendingdeflection.m for comparison to

%% TBTrigSolnForcedVibComparisonBVP4C.m)

R = 0.2;

S = 0.4;

LAMBDA = 1.87;

ZETA = 4;

The bvp4c program effectively checks the derivation of "*Derivation of Deflection due Solely to Bending Deformation, $Y_{B\text{-}D}(x)$*" and the integration of the equation for Φ to obtain:

$$\bar{V}_B(\xi)=\frac{C_1'}{n_1}e^{n_1(\lambda)\xi}-\frac{C_2'}{n_1}e^{-n_1(\lambda)\xi}+\frac{C_3'}{n_3}e^{n_3(\lambda)\xi}-\frac{C_4'}{n_3}e^{-n_3(\lambda)\xi}-\left(\frac{C_1'}{n_1}-\frac{C_2'}{n_1}+\frac{C_3'}{n_3}-\frac{C_4'}{n_3}\right)$$

as derived in Ch.3. However, instead of employing the analytical integration of the equation, the bvp4c program uses a numerical integration (trapezoidal integration) function of form:

$$V_B = \text{trapz}(X,V);$$

where,

X = the length from 0 to 1 (ξ) along the beam (of form xint = linspace(xlow, xhigh, 10001) in MATLAB file),

and

V = the numerical data for Φ (of form Sxint(3,:)in the MATLAB file)as obtained by the bvp4c ODE solver.

The results of the bvp4c program match those of the in-fluid Timoshenko MATLAB program for the magnitude of the complex tip displacement due to $V_{B\text{-}D}$.

Output: (at $\xi = 1$, i.e. tip)

TBFluidMaster.m:

Ybarmag(:,:,1,1,1,10001)

ans = 1.1018

bvp4cTBbendingdeflection.m:

Ybarmag = 1.1018

Since the results match for a variety of input values, the agreement between the two methods provides a check on the integration and programming of the TB BVP files.

APPENDIX B: DERIVATION OF THE FITTING PARAMETERS, C1 AND C2, BY MINIMIZATION OF ERROR BETWEEN THEORETICAL TIMOSHENKO MODEL AND EXPERIMENTAL DATA

2 Parameter Fit of TB Theory Frequencies to Experimental Frequencies:

The following procedure is the derivation of "best-fit" values for C1and C2 for fit of experimental data using in-vacuum Timoshenko Beam theory. Recall that the dimensionless frequency parameter *b* is dependent only on *r* and *s*. Where r and s are the parameters associated with rotatory inertia and shear, respectively. The best fit parameters C1 and C2 will be based on minimization of error between the Timoshenko theory frequencies and the experimental frequencies in air.

The following definitions are used:

$b = \sqrt{\frac{1}{EI}\frac{\gamma A}{g}} L^2 \omega$, the frequency parameter (B-1)

$r^2 = \frac{I}{AL^2}$, the parameter associated with rotatory inertia effects (B-2)

$s^2 = \frac{EI}{kAGL^2} = r^2 \frac{E}{kG}$, the parameter associated with shear effects and related to r^2 (B-3)

where:

$\gamma = \rho g$, weight per unit volume (B-4)

$A = Bh$, beam cross sectional area (B-5)

$B \equiv \text{in} - \text{plane dimension parallel to in} - \text{plane vibration}$

$h \equiv \text{in} - \text{plane dimension perpendicular to in} - \text{plane vibration}$

$I = \frac{hB^3}{12}$, second moment of area of cross section about neutral axis parallel to B dimension. (B-6)

Substituting (B-4) through (B-6) into (B-1) through (B-3) and rearranging results in:

$$\omega = b \frac{B}{L^2} \sqrt{\frac{E}{12\rho}}. \quad \text{(B-7)}$$

Converting circular frequency (radians) to natural frequency (Hz):

$$f = \frac{\omega}{2\pi} = b\frac{B}{L^2}\sqrt{\frac{E}{12\rho}}\frac{1}{2\pi} \tag{B-8}$$

$$r = \frac{B}{L\sqrt{12}} \tag{B-9}$$

$$s = \frac{B}{L\sqrt{12}}\sqrt{\frac{E}{kG}} = r\sqrt{\frac{E}{kG}} \tag{B-10}$$

From the previous derivation of the frequency equation it can be seen that the dimensionless frequency *b* from (B-1) is dependent only on the quantities r and s [i.e., b is a function g() of *r* and *s*]:

$$b = g(r, s) \tag{B-11}$$

Alternatively, the dimensionless frequency can be thought of using (B-9) and (B-10) as:

$$b = G\left(\frac{B}{L}, \sqrt{\frac{E}{kG}}\right) \tag{B-12}$$

Substituting (B-12) into (B-8):

$$f = \left(\frac{B}{L^2}\sqrt{\frac{E}{12\rho}}\frac{1}{2\pi}\right)\left[G\left(\frac{B}{L}, \sqrt{\frac{E}{kG}}\right)\right] \tag{B-13}$$

letting:

$$C1 = \sqrt{\frac{E}{12\rho}} \tag{B-14}$$

$$C2 = \sqrt{\frac{E}{kG}} \tag{B-15}$$

Rewriting the theoretical frequency (B-13) results in:

$$f^{th} = \frac{B}{L^2}C1\frac{1}{2\pi}\left[G\left(\frac{B}{L}, C2\right)\right] \tag{B-16}$$

f^{th} = theoretical frequency

The C1 and C2 in (B-16) are the fit parameters whose values will be determined to give the best-fit of the experimental frequency data by minimization of the sum of the squared errors, *e*:

$$e = \sum_{i=1}^{N}\left(f_i^{exp} - f_i^{th}\right)^2 \tag{B-17}$$

where:

N = number of data points

f^{exp} = experimental frequency

Substituting (B-16) into (B-17) provides:

$$e = \sum_{i=1}^{N} \left\{ f_i^{exp} - \frac{B_i}{{L_i}^2} C1 \frac{1}{2\pi} \left[G\left(\frac{B_i}{L_i}, C2\right) \right] \right\}^2 \tag{B-18}$$

Minimize the error (B-18) with respect to C1 and C2 results in:

$$\frac{\partial e}{\partial C1} = 0 \; ; \frac{\partial e}{\partial C2} = 0$$

$$\frac{\partial e}{\partial C1} = \sum 2 \left\{ f_i^{exp} - \frac{B_i}{{L_i}^2} C1 \frac{1}{2\pi} \left[G\left(\frac{B_i}{L_i}, C2\right) \right] \right\} \cdot \left\{ - \frac{B_i}{{L_i}^2} \frac{1}{2\pi} \left[G\left(\frac{B_i}{L_i}, C2\right) \right] \right\} = 0 \tag{B-19}$$

$$\sum \left\{ f_i^{exp} - \frac{B_i}{{L_i}^2} C1 \frac{1}{2\pi} [G_i(C2)] \right\} \cdot \left\{ \frac{B_i}{{L_i}^2} \frac{1}{2\pi} [G_i(C2)] \right\} = 0$$

where:

$$G_i(C2) \equiv \; G\left(\frac{B_i}{L_i}, C2\right)$$

Simplifying:

$$\sum \left\{ \frac{B_i}{{L_i}^2} \frac{1}{2\pi} [G_i(C2)] {f_i}^{exp} \right\} - \sum \left\{ \frac{B_i}{{L_i}^2} \frac{1}{2\pi} C2 [G_i(C2)] \frac{B_i}{{L_i}^2} \frac{1}{2\pi} [G_i(C2)] \right\} = 0$$

$$\sum \left\{ \frac{B_i}{{L_i}^2} \frac{1}{2\pi} [G_i(C2)] {f_i}^{exp} \right\} - C1 \sum \left\{ \frac{{B_i}^2}{{L_i}^4} \frac{1}{4\pi^2} [G_i(C2)]^2 \right\} = 0$$

$$C1 = \frac{\sum \left\{ \frac{B_i}{{L_i}^2} \frac{1}{2\pi} [G_i(C2)] {f_i}^{exp} \right\}}{\sum \left\{ \frac{{B_i}^2}{{L_i}^4} \frac{1}{4\pi^2} [G_i(C2)]^2 \right\}} = \frac{\frac{1}{2\pi} \sum \left\{ \frac{B_i}{{L_i}^2} [G_i(C2)] {f_i}^{exp} \right\}}{\frac{1}{4\pi^2} \sum \left\{ \frac{{B_i}^2}{{L_i}^4} [G_i(C2)]^2 \right\}} = 2\pi \frac{\sum \left\{ \frac{B_i}{{L_i}^2} [G_i(C2)] {f_i}^{exp} \right\}}{\sum \left\{ \frac{{B_i}^2}{{L_i}^4} [G_i(C2)]^2 \right\}} \tag{B-20}$$

$$\frac{\partial e}{\partial c_2} = \sum 2 \left\{ f_i^{exp} - \frac{B_i}{{L_i}^2} C1 \frac{1}{2\pi} [G_i(C2)] \right\} \cdot \left\{ - \frac{B_i}{{L_i}^2} \frac{1}{2\pi} [G_i'(C2)] C1 \right\} = 0$$

$$\sum \left\{ f_i^{exp} - \frac{B_i}{{L_i}^2} C1 \frac{1}{2\pi} [G_i(C2)] \right\} \cdot \left\{ \frac{B_i}{{L_i}^2} \frac{1}{2\pi} [G_i'(C2)] C1 \right\} = 0$$

$$\sum \left\{ \frac{B_i}{{L_i}^2} \frac{1}{2\pi} [G_i'(C2)] C1 {f_i}^{exp} \right\} - \sum \left\{ \frac{{B_i}^2}{{L_i}^4} \frac{1}{4\pi^2} {c_1}^2 [G_i(C2)][G_i'(C2)] \right\} = 0$$

$$\sum \left\{ \frac{B_i}{{L_i}^2} \frac{1}{2\pi} [G_i'(C2)] {f_i}^{exp} \right\} - C1 \sum \left\{ \frac{{B_i}^2}{{L_i}^4} \frac{1}{4\pi^2} [G_i(C2)][G_i'(C2)] \right\} = 0$$

$$C1 = \frac{\sum \left\{ \frac{B_i}{{L_i}^2} \frac{1}{2\pi} [G_i'(C2)] {f_i}^{exp} \right\}}{\sum \left\{ \frac{{B_i}^2}{{L_i}^4} \frac{1}{4\pi^2} [G_i(C2)][G_i'(C2)] \right\}} = 2\pi \frac{\sum \left\{ \frac{B_i}{{L_i}^2} [G_i'(C2)] {f_i}^{exp} \right\}}{\sum \left\{ \frac{{B_i}^2}{{L_i}^4} [G_i(C2)][G_i'(C2)] \right\}} \tag{B-21}$$

Setting (B-20) = (B-21) yields

$$g(C2) \equiv 2\pi \frac{\Sigma\left\{\frac{B_i}{L_i^2}[G_i{}'(C2)]f_i{}^{exp}\right\}}{\Sigma\left\{\frac{B_i{}^2}{L_i{}^4}[G_i(c_2)][G_i{}'(C2)]\right\}} - 2\pi \frac{\Sigma\left\{\frac{B_i}{L_i^2}[G_i(C2)]f_i{}^{exp}\right\}}{\Sigma\left\{\frac{B_i{}^2}{L_i{}^4}[G_i(C2)]^2\right\}} = 0 \qquad \text{(B-22)}$$

$$g(C2) \equiv \frac{\Sigma\left\{\frac{B_i}{L_i^2}[G_i{}'(C2)]f_i{}^{exp}\right\}}{\Sigma\left\{\frac{B_i{}^2}{L_i{}^4}[G_i(c_2)][G_i{}'(C2)]\right\}} - \frac{\Sigma\left\{\frac{B_i}{L_i^2}[G_i(C2)]f_i{}^{exp}\right\}}{\Sigma\left\{\frac{B_i{}^2}{L_i{}^4}[G_i(C2)]^2\right\}} = 0 \qquad \text{(B-23)}$$

The function g(C2) given in [23] is in terms of known geometric quantities (*B, L*), known experimental frequencies and the theoretical frequencies as a function of C2. Recall:

$$C2 = \sqrt{\frac{E}{kG}}$$

Therefore, (B-21) can be plotted against values of C2 to find the root of the equation (i.e. the point at which the function is zero or closest to zero according to the minimization of the square of the errors). Once the best value of C2 is known, either (B-20) or (B-21) can be used to calculate the best value of C1. Recall:

$$C1 = \sqrt{\frac{E}{12\rho}}$$

APPENDIX C:IN-VACUUM THEORETICAL FREQUENCY PLOTS: BEST FIT OF IN-AIR EXPERIMENTAL DATA USING TIMOSHENKO AND EULER-BERNOULLI THEORIES

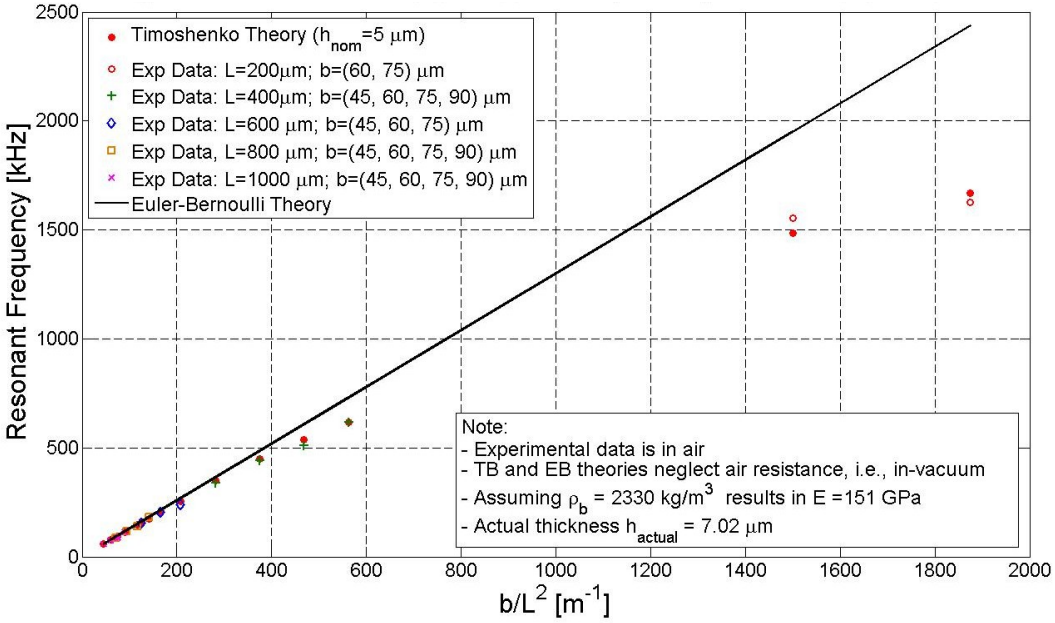

Figure C-1: Comparison of Current In-Vacuum (i.e., $\zeta = 0$), Timoshenko Model to Experimental [Beardslee et al., 2010a] In-Air Resonant Frequencies For First Lateral Flexural Mode Due to Harmonic Support Rotation; Nominal Thickness of 5 μm, $\sqrt{E/12\rho_b}$ = 2.3240 km/sec, $\sqrt{E/kG}$ = 4.4231 and E = 151 GPa

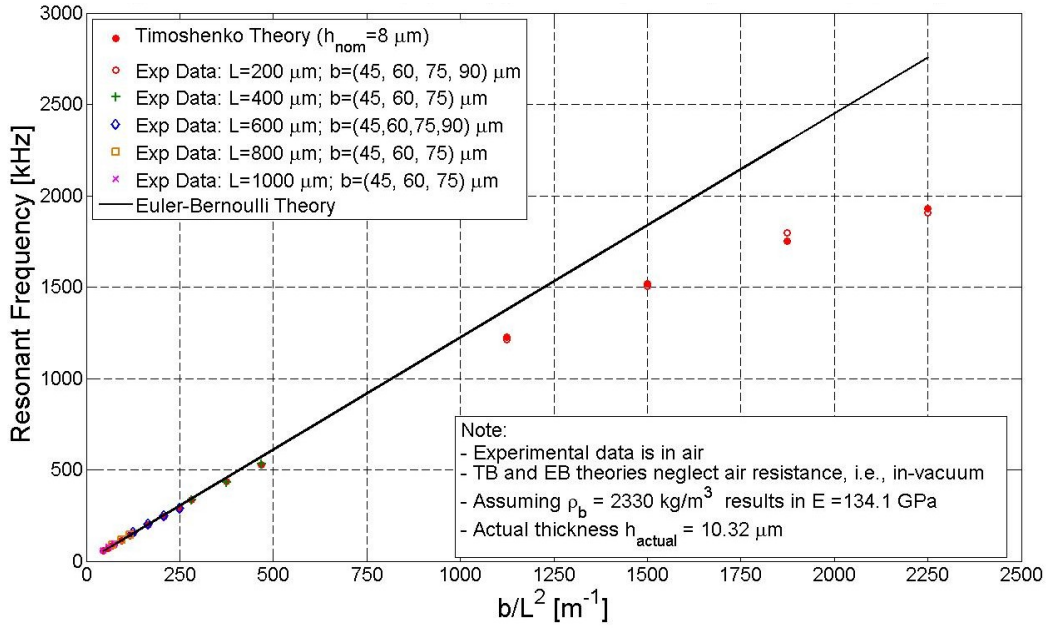

Figure C-2: Comparison of Current In-Vacuum (i.e., $\zeta = 0$), Timoshenko Model to Experimental [Beardslee et al., 2010a] In-Air Resonant Frequencies For First Lateral Flexural Mode Due to Harmonic Support Rotation; Nominal Thickness of 8 μm, $\sqrt{E/12\rho_b}$ = 2.1903 km/sec, $\sqrt{E/kG}$ = 3.5117 and E = 134.1 GPa

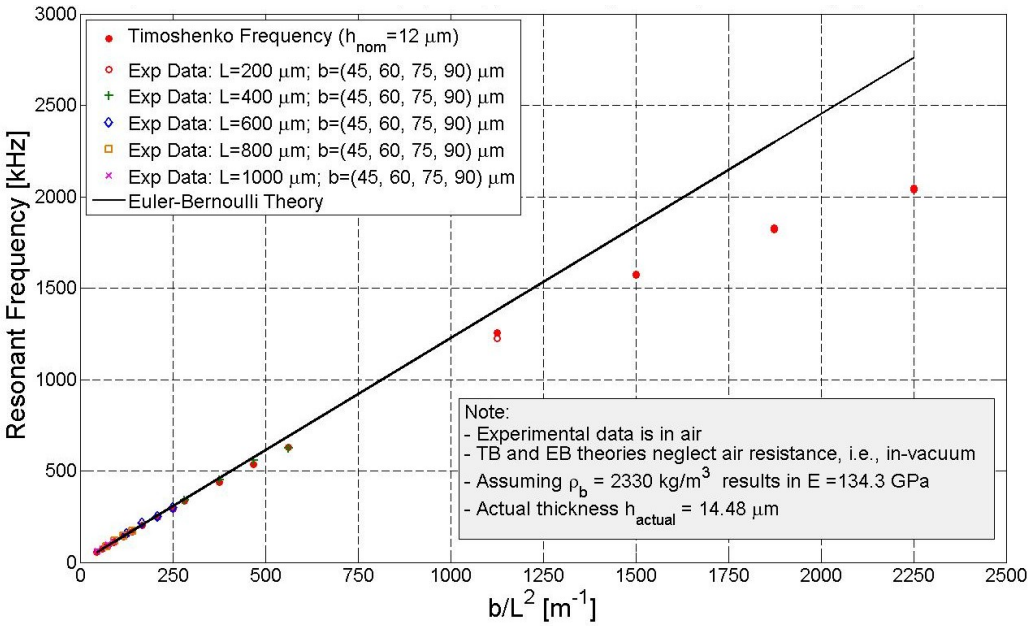

Figure C-3: Comparison of Current In-Vacuum (i.e., $\zeta = 0$), Timoshenko Model to Experimental [Beardslee et al., 2010a] In-Air Resonant Frequencies For First Lateral Flexural Mode Due to Harmonic Support Rotation; Nominal Thickness of 12 μm, $\sqrt{E/12\rho_b}$ = 2.1920 km/sec, $\sqrt{E/kG}$ = 3.1288 and E = 134.3 GPa

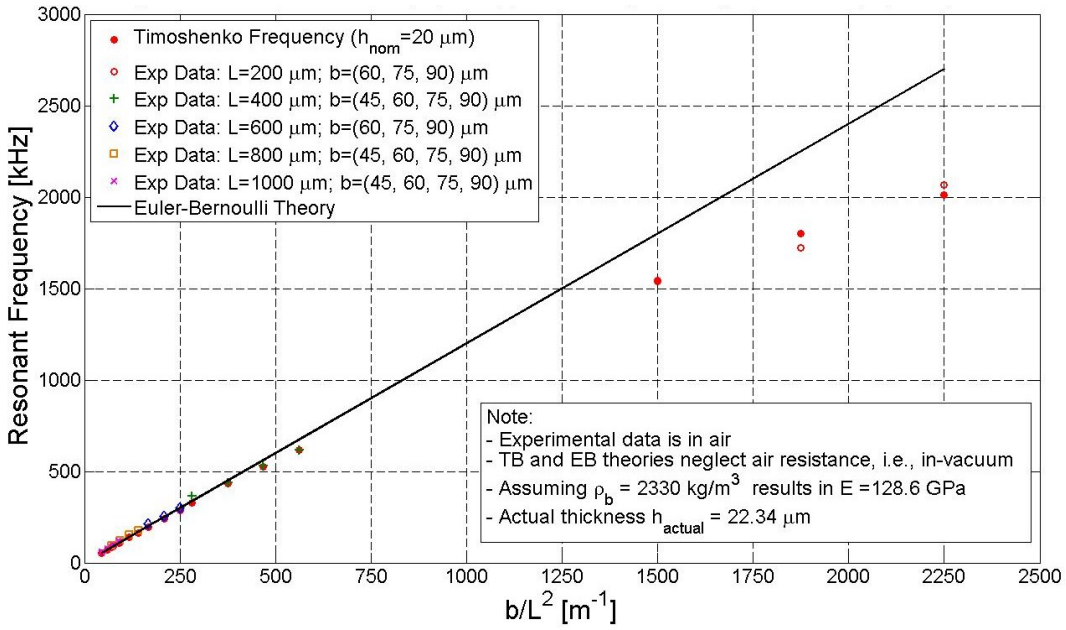

Figure C-4: Comparison of Current In-Vacuum (i.e., $\zeta = 0$), Timoshenko Model to Experimental [Beardslee et al., 2010a] In-Air Resonant Frequencies For First Lateral Flexural Mode Due to Harmonic Support Rotation; Nominal Thickness of 20 μm, $\sqrt{E/12\rho_b}$ = 2.1446 km/sec, $\sqrt{E/kG}$ = 3.0642 and E = 128.6 GPa